

**DETERMINATION OF MILLIMETRIC SIGNAL ATTENUATION
DUE TO RAIN USING RAIN RATE AND RAINDROP SIZE
DISTRIBUTION MODELS FOR SOUTHERN AFRICA**

by

Senzo Jerome Malinga

A THESIS

submitted in fulfillment of the requirements for the degree

PhD (ELECTRONIC ENGINEERING)

School of Engineering

College of Agriculture, Engineering, and Science



**UNIVERSITY OF
KWAZULU-NATAL**

**INYUVESI
YAKWAZULU-NATALI**

UNIVERSITY OF KWAZULU-NATAL

Durban, South Africa

March 2014

Supervisor: **Professor Thomas Joachim Odhiambo Afullo**

Approved by:

Supervisor: **Professor Thomas Joachim Odhiambo Afullo**

As the candidate's Supervisor I agree to the submission of this thesis.

Signed.....Date.....

COLLEGE OF AGRICULTURE, ENGINEERING AND SCIENCE

Declaration 1 - Plagiarism

I **Senzo Jerome Malinga** declare that

1. The research reported in this thesis, except where otherwise indicated, is my original research.
2. This thesis has not been submitted for any degree or examination at any other university.
3. This thesis does not contain other persons' data, pictures, graphs or other information, unless specifically acknowledged as being sourced from other persons.
4. This thesis does not contain other persons' writing, unless specifically acknowledged as being sourced from other researchers. Where other written sources have been quoted, then:
 - a. Their words have been re-written but the general information attributed to them has been referenced
 - b. Where their exact words have been used, then their writing has been placed in italics and inside quotation marks, and referenced.
5. This thesis does not contain text, graphics or tables copied and pasted from the Internet, unless specifically acknowledged, and the source being detailed in the thesis and in the References sections.

Signed.....Date.....

Declarations 2 - Publications

DETAILS OF CONTRIBUTION TO PUBLICATIONS that form part and/or include research presented in this thesis (include publications in preparation, submitted, *in press* and published and give details of the contributions of each author to the experimental work and writing of each publication).

Journal Publications

1. Senzo J. Malinga and Pius A. Owolawi, "Obtaining Raindrop Size Model Using the Method of Moments and Its Applications for South African Radio Systems," *PIER B Journal*, Vol. 46, pp. 119-138, 2013.

In this paper, the Raindrop Size Distribution (DSD) modeling and analysis are presented. Drop sizes are classified into different rain types, namely: drizzle, widespread, shower and thunderstorm. The gamma and Lognormal distribution models are employed using the method of moments estimator, considering the third, fourth and sixth order moments. The results are compared with the existing raindrop size distribution models such as the three parameter lognormal distribution proposed by Ajayi and his colleagues and Singapore's modified gamma and Lognormal models. This is then followed by the implementation of the proposed raindrop size distribution models on the computation of the specific rain attenuation. Finally, the paper suggests a suitable DSD model for the region with its expressions. The proposed models are very useful for the determination of rain attenuation for terrestrial and satellite systems.

2. Senzo J. Malinga, P.A. Owolawi and T.J.O. Afullo, "Determination of Specific Rain Attenuation using Different Total Cross Section Models for Southern Africa," – *Africa Research Journal* Vol. 104, No. 3, 2013 (accepted).

Electromagnetic waves whose frequency is beyond 10 GHz are severely attenuated by rain. This is true in both satellite and terrestrial links. The rain attenuation is mainly manifested in the form of scattering and absorption. In the paper presented here, various total cross section models are used to calculate the

specific attenuation due to rain for the frequencies between 1 to 100 GHz. The DSD modelling is done using the Method of Moments, from which the specific attenuation due to rain is computed. Comparisons are then drawn between the models proposed, well known models in existence, and theoretical results for three different polarizations at 19.5 GHz frequency.

Conference Publications

1. P.A. Owolawi, S.J. Malinga and T.J.O. Afullo, "Estimation of Terrestrial Rain Attenuation at Microwave and Millimeter Wave Signals in South Africa Using the ITU-R Model," *PIERS Proceedings*, Kuala Lumpur, Malaysia, March 27-30, 2012, pp. 952-962.

In this paper, experimental rain rate measurements are presented together with rain attenuation results computed via the application of the International Telecommunication Union's Recommendations (ITU-R) model for attenuation due to rain in terrestrial links in South Africa. A total of nineteen case study locations, at least every province in South Africa represented by one, are used for this presentation. The paper specifically presents results of the total path and specific attenuation for terrestrial links for three different types of polarizations in the frequencies ranging from 1 to 400 GHz. The implications of rain attenuation to the system designers are evaluated by finding link distance chart, and design link-budget at the chosen frequency range. The results of this work can be used in planning links for both microwave and millimeter broadband wireless networks in South Africa such as Local-Multipoint-Distributed-Services (LMDs).

2. Mulangu, C.T.; Malinga, S.J.; Afullo, T.J.O., "Impact of rain on microwave radars," 2012 International Conference on Electromagnetics in Advanced Applications (ICEAA), vol., no., pp.1088,1091, 2-7 Sept. 2012, Cape Town

The most important source of disturbance in microwave links is caused by precipitation attenuation due to mainly snow and rain via scattering and absorption. In this paper, two year experimental rain rate data is used to perform the reflectivity profile of radar at various rain rates using the lognormal DSD model for Durban.

3. S.J. Malinga, P.A. Owolawi, and T.J.O. Afullo, "Estimation of Rain Attenuation at C, Ka, Ku, and V Bands for Satellite Links in South Africa," *PIERS Proceedings*, Taipei, Taiwan, March 25-28, 2013, pp. 948-958.

The fast growth in telecommunications, increased demand for bandwidth, congestion in lower frequency bands and miniaturization of communication equipment have forced the designers to employ higher frequency bands such as the C (4 to 8 GHz), Ka (26.5 to 40GHz), Ku (12-18 GHz) and V (40-75 GHz) bands. Rain is the most deleterious to signal propagation in these bands. The contribution of rain attenuation to the quality of signal in these bands, especially in the tropical and subtropical bands in which South Africa is located, need to be studied. The aims of this paper are to estimate the magnitude of rain attenuation using the ITU-R model, carry out link performance analysis, and then propose reasonable, adequate fade margins that need to be applied for all provinces in South Africa.

4. S.J. Malinga, P.A. Owolawi, and T.J.O. Afullo, “Computation of Rain Attenuation through Scattering at Microwave and Millimeter Bands in South Africa,” *PIERS Proceedings*, Taipei, Taiwan, March 25-28, 2013, pp. 959-971.

In this presentation, both measured and calculated rain attenuation are obtained using two methods. These methods are the Pruppacher-Pitter technique (non-spherical method) and the Mie Scattering technique (spherical method). Incorporation of available DSD data and measured rain rate with the derived scattering amplitude coefficients is then done to estimate the total and specific attenuation due to rain for the South Africa region. Comparison between the results obtained with the few known rain attenuation models and one-year attenuation measurement data in South Africa (Durban) are then drawn. Further, the results obtained are tested for both satellite and terrestrial radio links at particular rain rates and specific frequencies.

5. P.A. Owolawi, S.J. Malinga, T.J.O. Afullo “Computation of rain scattering properties at SHF and EHF for radio wave propagation in South Africa”, URSI Commission F Triennial, April 30 – May 3, 2013, Ottawa, Canada.

In this paper computation of scattering parameters at 1 – 100 GHz frequencies under the influence of a rainy medium are presented. The characteristics of scattering parameters at these frequencies are integrated and computed with lognormal raindrop size distribution for four rain types, and the results are used to compute the specific attenuation due to rain as well as the associated specific phase shift. The calculated specific attenuation due to rain and its phase shift results are compared with tropical and temperate regions’ counterparts. In addition, analytical coefficients of the fundamental specific rain attenuation and specific phase shift are derived in the same frequency range of different rain types in Southern Africa.

6. Chrispin T. Mulangu, Senzo J. Malinga, Thomas J. Afullo, “Prediction of Radar Reflectivity along Radio Links”, PIERS Proceedings, pp. 264 – 267, Taipei, March 25 – 28, 2013

Radiowaves propagating through a rain zone will be scattered, depolarized, absorbed and delayed in time. All these effects of rain on the wave propagation are related to the frequency at which the signal is transmitted and polarization of the wave as well as to the rain rate, which influences the form and size distribution of the raindrop. The average power received by the bistatic radar is proportional to the product of reflectivity and attenuation. These can be measured in practice but sometimes there is a need to determine them separately. In order to determine radar reflectivity, the backscattering coefficient needs to be estimated. This study makes predictions about the backscattering coefficient caused by hydrometeors along terrestrial radio links, operated at wide bandwidth of 10 – 140 GHz frequencies. The scattering properties of the spherical raindrops are calculated for different sizes of raindrops. From the scattering properties, the back cross-sections for the spherical raindrops are determined for different frequencies. These are integrated over different established raindrop-size distribution models to formulate radar reflectivity and fitted to generate power-law models.

Signed:.....Date.....

Acknowledgements

First and foremost, I wish to thank the Almighty God for giving me energy, good health, and the right state of mind and wisdom that has enabled me to pursue this dream to the end.

This journey has been long and would not have been possible without the unrelenting supervision accorded by my supervisor, Prof. Thomas Joachim Odhiambo Afullo. I am very grateful for the many times we shared, discussing tirelessly the progress made on this study, and the constructive criticism and inputs rendered at different stages of this work. Without his guidance and unrelenting support, this work would not have come to a successful completion.

Additionally, I wish to convey my sincere gratitude to my wife, Lucia Babongile Malinga, for her understanding and support during the most grueling periods of the dream. Her care and love have for sure been a source of strength and inspiration in all that I undertake to do.

Also, I would wish to thank all those who assisted in one way or the other during the compilation and editing of this work. Most notably, I wish to acknowledge, Dr. P.A. Owolawi, Mr. Chrispin Mulangu and Mr. Abraham Nyete for their editing assistance and critic of the write up.

There are many other people, who assisted in many other ways, but all their names cannot fit here, nonetheless, to all of you, may God continue to bless you so that you may also touch other people's lives.

Abstract

The advantages offered by Super High Frequency (SHF) and Extremely High Frequency (EHF) bands such as large bandwidth, small antenna size, and easy installation or deployment have motivated the interest of researchers to study those factors that prevent optimum utilization of these bands. Under precipitation conditions, factors such as clouds, hail, fog, snow, ice crystals and rain degrade link performance. Rain fade, however, remains the dominant factor in the signal loss or signal fading over satellite and terrestrial links especially in the tropical and sub-tropical regions within which South Africa falls. At millimetre-wave frequencies the signal wavelength approaches the size of the raindrops, adversely impacting on radio links through signal scattering and absorption. In this work factors that may hinder the effective use of the super high frequency and extremely high frequency bands in the Southern African region are investigated. Rainfall constitutes the most serious impairment to short wavelength signal propagation in the region under study. In order to quantify the degree of impairment that may arise as a result of signal propagation through rain, the raindrops scattering amplitude functions were calculated by assuming the falling raindrops to be oblate spheroidal in shape. A comparison is made between the performance of the models that assume raindrops to be oblate spheroidal and those that assume them to be spherical.

Raindrops sizes are measured using the Joss-Waldvogel RD-80 Distrometer. The study then proposes various expressions for models of raindrops size distributions for four types of rainfall in the Southern Africa region. Rainfall rates in the provinces in South Africa are measured and the result of the cumulative distribution of the rainfall rates is presented. Using the information obtained from the above, an extensive calculation of specific attenuation and phase shift in the region of Southern Africa is carried out. The results obtained are compared with the ITU-R and those obtained from earlier campaigns in the West African sub region. Finally, this work also attempts to determine and characterize the scattering process and micro-physical properties of raindrops for sub-tropical regions like South Africa. Data collected through a raindrop size measurement campaign in Durban is used to compare and validate the developed models.

Table of Contents

Declaration 1 - Plagiarism.....	iii
Declaration 2-Publications.....	iv
Acknowledgements.....	viii
Abstract	ix
Table of Contents.....	x
List of Figures.....	xiv
List of Tables	xvi
Chapter 1.....	1
Introduction.....	1
1.1 Research Question.....	1
1.2 Aims and Objectives.....	2
1.3 Methodological Approach.....	2
1.4 Significance of the Study.....	2
1.5 Contributions.....	3
1.6 Organization of the Thesis.....	3
Chapter 2.....	5
Background Literature Review	5
2.0 Introduction	5
2.1 Tropospheric Propagation Effects	6
2.1.1 Clear-air Effects	6
2.1.2 Diffraction fading.....	6
2.1.3 Multipath propagation (fading).....	7
2.1.4 Absorption by Atmospheric Gases.....	9
2.1.5 Scintillation	10
2.1.5.1 Karasawa, Yamada and Allnut Model.....	10
2.1.5.2 The ITU-R Scintillation Model.....	12
2.1.6 Hydrometeor Effects	12
2.2 Modeling of Different Propagation Impairments	12
2.2.1 Rain Attenuation	12

2.2.2	Cloud Attenuation.....	14
2.2.2.1	Liebe Model.....	14
2.2.2.2	Altshuler Model.....	15
2.2.2.3	Gunn and East Model.....	15
2.2.2.4	Staelin Model.....	16
2.2.2.5	Slobin Model.....	16
2.2.3	Melting Layer Attenuation.....	16
2.3	The Current South African Situation.....	17
2.4	Chapter Summary and Conclusion.....	20
Chapter 3.....		21
Characterization of Rain Attenuation in Terrestrial and Satellite Links in Southern Africa.....		
3.0	Introduction.....	21
3.1	Terrestrial Rain Attenuation at Microwave and Millimetre Frequencies in South Africa.....	21
3.1.1	Introductory Concepts in Rain Attenuation.....	21
3.1.2	Cumulative Distribution of Rain Rate.....	23
3.1.3	Specific Rain Attenuation Distribution for All Provinces in South Africa.....	25
3.1.4	Estimation of Total Path Attenuation for South African Provinces.....	27
3.2	Rain Attenuation at C, Ka, Ku and V Bands for Satellite Links in South Africa.....	31
3.2.1	Introduction to earth-space links in South Africa.....	32
3.2.2	Rain Height.....	33
3.2.3	Slant Path Rain Attenuation Models.....	34
3.2.3.1	ITU-R Rain Attenuation Model.....	34
3.2.4	Earth-Space Rain Attenuation.....	43
3.3	Chapter Summary and Conclusion.....	49
Chapter 4.....		51
Raindrop Size Modelling Using Method of Moments and its Applications for South Africa Radio		
Systems.....		
4.0	Introduction.....	51
4.1	Raindrop Size Distribution Modelling.....	51
4.2	Experimental Setup and Data Sorting.....	53
4.3	DSD Models with the Method of Moments (MoM).....	55
4.4	Gamma Distribution Model and MoM.....	56

4.5 Lognormal Distribution Model and MoM.....	59
4.6 Comparison and Validation of Results.....	62
4.7 Specific Rain Attenuation.....	64
4.8 Chapter Summary and Conclusion.....	68
 Chapter 5.....	 70
Specific Rain Attenuation Computation Using Different Total Cross Section Models.....	70
5.0 Introduction.....	70
5.1 Rain Drop Size Modelling.....	70
5.2 Data Collection and Modelling.....	72
5.3 Application of Rainfall Regimes.....	74
5.4 Comparison of DSD Models in South Africa and West African Countries.....	75
5.5 Scattering Properties of Distorted Raindrops.....	75
5.6 Scattering Coefficients.....	75
5.7 Total Scattering Cross Section.....	77
5.8 Specific and Total Rain Attenuation.....	81
5.9 The Olsen Model for Specific Rain Attenuation.....	88
5.10 Chapter Summary and Conclusion.....	91
 Chapter 6.....	 92
Specific Attenuation and Phase Shift due to Rain.....	92
6.0 Introduction.....	92
6.1 The physics of the rain structure.....	93
6.2 Method of Moments and the three-parameter Lognormal Distribution.....	95
6.3 Specific Rain Attenuation and Phase Shift: Pruppacher-Pitter Theory.....	95
6.4 Comparative studies of specific attenuation and phase shift with existing models.....	102
6.5 Power Law regression for specific attenuation and phase shift.....	104
6.6 Chapter Summary and Conclusion.....	108
 Chapter 7.....	 109
Conclusions and Recommendations for Future Work.....	109
7.0 Conclusions.....	109
7.1 Recommendations for Future Work.....	111

References..... 112

List of Figures

Figure 2.1: Specific Attenuation due to Atmospheric Gases.....	11
Figure 2.2 Specific attenuation caused by rain [7].....	14
Figure 3.1 Map of South Africa [7].....	22
Figure 3.2: Average cumulative time distribution of the rain rate in all provinces in South Africa.....	23
Figure 3.3: Specific Rain Attenuation (Horizontal polarization) for the Provinces in South Africa	26
Figure 3.4: Specific Rain Attenuation (Vertical polarization) for the Provinces in South Africa	26
Figure 3.5a: Total Path Attenuation for vertically polarized signals at various frequencies	28
Figure 3.5b: Total Path Attenuation for horizontally polarized signals at various frequencies.....	28
Figure 3.6a: Predicted Rain Attenuation (VP) against Availability.....	30
Figure 3.6b: Predicted Rain Attenuation (CP) against Availability.....	31
Figure 3.6c: Predicted Rain Attenuation (HP) against Availability.....	31
Figure 3.7: Slant path through rain [17].....	34
Figure 3.8a: Rain Attenuation at 0.01% exceedence for all regions for Circular Polarization	40
Figure 3.8b: Rain Attenuation at 0.01% exceedence for all regions for Horizontal Polarization.....	40
Figure 3.8c: Rain Attenuation at 0.01% exceedence for all regions for Vertical Polarization	41
Figure 3.9a: Effective path length for all regions for Circular Polarization	41
Figure 3.9b: Effective path length for all regions for Horizontal Polarization	42
Figure 3.9c: Effective path length for all regions for Vertical Polarization.....	42
Figure 3.10a: Rain Attenuation at C-band for Horizontal Polarization for all locations at 4 GHz.....	44
Figure 3.10b: Rain Attenuation at C-band for Horizontal Polarization for all locations at 8 GHz.....	45
Figure 3.11a: Rain Attenuation at Ku-band for Vertical Polarization for all locations at 12 GHz.....	45
Figure 3.11b: Rain Attenuation at Ku-band for Vertical Polarization for all locations at 18 GHz.....	46
Figure 3.12a: Rain Attenuation at Ka-band for Circular Polarization for all provinces at 26.5 GHz.....	46
Figure 3.12b: Rain Attenuation at Ka-band for Circular Polarization for all provinces at 40 GHz.....	47
Figure 3.13a: Rain Attenuation at V-band at 75 GHZ for all Provinces for Horizontal Polarization	47
Figure 3.13b: Rain Attenuation at V-band at 75 GHZ for all Provinces for Vertical Polarization	48
Figure 3.13c: Rain Attenuation at V-band at 75 GHZ for all Provinces for Circular Polarization.....	48
Figure 4.1: Block diagram of the JWD-RD 80 Distrometer [115].....	53
Figure 4.2: Distrometer enclosure on Durban site.....	54
Figure 4.3: Scatter plots for shower: Gamma parameters against rain rate.....	58
Figure 4.4: Scatter plots for widespread: Lognormal parameters against rain rate.....	61
Figure 4.5: Comparative studies of the proposed model with existing ones at different rain rate.....	63

Figure 4.6a: Specific rain attenuation for different rain types and general model.....	67
Figure 4.6b: Specific rain attenuation for different rain types and general model.....	67
Figure 4.6c: Specific rain attenuation for different rain types and general model.....	68
Figure 4.6d: Specific rain attenuation for different rain types and general model.....	68
Figure 5.1: Scattergrams of estimated Lognormal parameters (a) N_T (b) μ and (c) σ^2 , versus the rain rate for the thunderstorm rain type.....	73
Figure 5.2: Comparison of extinction cross-sections of MC, P-P, and Mie models at horizontal and vertical polarization versus mean drop radius at (a) 7.8 GHz (b) 13.6 GHz (c) 19.5 GHz (d) 34.8 GHz (e) 140 GHz (f) 245.5 GHz	80
Figure 5.3: Specific attenuation due to rain versus frequency for different rain types: (a) Drizzle, (b) Widespread, (c) Shower and (d) Thunderstorm.....	84
Figure 5.4: Specific rain attenuation against rain-rate for (a) 7.8 GHz (b) 19.5 GHz (c) 34.8 GHz and (d) 140 GHz	87
Figure 5.5: Coefficient k against frequency (Note: the Spheroidal model is the M-C model)	88
Figure 5.6: Coefficient α against frequency (Note: the Spheroidal model is the M-C model)	89
Figure 6.1: Characteristics for the complex refractive index of water at 3 different temperatures	94
Figure 6.2: Lognormal DSD for: (a) Drizzle (b) widespread (c) Shower, and (d) Thunderstorm.....	97
Figure 6.3: Specific Attenuation for: a) Drizzle (b) Widespread (c) Shower (d) Thunderstorm.....	99
Figure 6.4: Specific Phase Shift: (a) Drizzle (b) Widespread (c) Shower (d) Thunderstorm.....	101
Figure 6.5: Percentage difference in specific attenuation due to rain for different rain rates in different regions with respect to the ITU-R model.....	102
Figure 6.6: Percentage difference in phase shift for different rain rates in different regions with respect to the ITU-R model.....	103

List of Tables

Table 2.1: Monthly rain attenuation models for a 6.3 km link in Durban, South Africa, for 2004.	19
Table 2.2: Analysis of the logarithmic and power regression estimates for the measured minimum, average and maximum attenuation values.....	19
Table 3.1: Rain rate at 0.01% for all the Provinces in South Africa.....	24
Table 3.2: The specific attenuation parameters given by ITU-R [20]	25
Table 3.3: Average rain rate at 0.01% for all provinces in South Africa.....	33
Table 3.4: Characteristics for Locations in South Africa at 0.01% time of exceedance.....	39
Table 4.1: Summary of gamma Parameter Model for Raindrop Size Distribution in Durban.....	59
Table 4.2: Summary of Lognormal Parameter Model for Raindrop size Distribution in Durban.....	62
Table 4.3: RMSE for different raindrop size distribution models in Percentage.....	64
Table 4.4: specific rain attenuation power law coefficients for different rain types.....	66
Table 5.1: Coefficients of Lognormal DSD parameters in Equation (5.6, 5.7) for Southern Africa (SA) and West Africa (WA).....	74
Table 5.2: Error analysis (RMSE in %) of the proposed Lognormal model and West Africa model.....	74
Table 5.3: Comparison of rain attenuation for P-P and MC model against the Mie model at different rain rates at 100 GHz.....	81
Table 5.4: Comparison of the P-P and M-C models to the Mie model at different frequencies.....	85
Table 5.5: Power law model parameters for the three drop-size models	90
Table 5.6: Modelled coefficient k.....	90
Table 5.7: Modelled coefficient α	90
Table 6.1: The values of a and b given for the frequency range 1-100 GHz for the Southern African Region.....	105
Table 6.2: The values of α and β for frequencies range 1-1000 GHz for South Africa region.....	107

Chapter 1

Introduction

1.1 Research Question

Propagation impairments arising from signal attenuation and phase shift due to rain and cloud effects, absorption by atmospheric gases, and tropospheric refractive effects adversely compromise the quality of millimetric band signals thereby resulting in appreciable digital transmission errors. While rain fade, essentially a non-clear-air tropospheric effect that is characterized by variations in signal amplitude and phase, is the dominant impairment at frequencies above 10 GHz, clear-air tropospheric effects like gaseous absorption and tropospheric scintillation are also appreciable impairments at these frequency ranges. These impairments result in the degradation on the Quality of Service (QoS) in terrestrial and satellite communications links. Modeling of these effects is essential for communications service providers in accurately predicting propagation impairments as a necessary basis for mitigation planning through approaches like adaptively selecting appropriate power levels, coding and modulation schemes.

The study is focused on the effects of rain on millimetric waves at frequencies of 10 – 100 GHz where the presence of rain degrades the performance of communication systems. Congestion at lower frequency bands and the increased use of digital techniques and orthogonally polarized frequency channels have made it imperative for communications service providers to migrate to higher frequency bands. However, at these frequency bands the wavelength of the transmitted signal approaches the size of the raindrops, which results in the degradation of the communication link when these signals interact with the raindrops. This degradation is in the form of signal amplitude attenuation and phase change caused by signal absorption and scattering due to displacement currents in the rain drops and the raindrops' high dielectric constants at high frequencies [1]. To determine the magnitude of signal degradation, the detailed scattering process and microphysical properties of raindrops must be known.

Most of the work that has been done in this subject has been in temperate regions and to some extent in tropical regions of West Africa and South America, which has made it necessary for similar work to be done for sub-tropical regions like South Africa. A raindrop size distribution measurement campaign for Southern Africa has been accomplished through the work led by Afullo [2] from which was suggested the use of the log-normal distribution for raindrop sizes for South Africa due to the over-estimation of the small diameter raindrops emanating from the use of the Laws and Parsons [3] exponential distribution models. Moupfouma and Tiffon [4] also suggested a modified form of the

Marshall and Palmer distribution for the equatorial regions due to the similar limitations of the Laws and Parsons model.

This study presents calculated rain attenuation obtained using two raindrop shape models. These models are the Pruppacher-Pitter technique [5] (non-spherical method) and the Mie Scattering technique (spherical method) [6]. The two methods are chosen by virtue of the frequency band of interest in this work (10 – 100 GHz). The Mie technique has been chosen over the Rayleigh technique since the latter is best suited for frequencies between 1 and 3 GHz while the Mie scattering technique is best suited for higher frequencies, see for example [7] for more elaborate details on the consideration of each of these techniques. The available DSD data and measured rain rates are combined with the derived scattering amplitude coefficients to estimate the total and specific attenuation due to rain for the South Africa region. The results obtained are compared with existing rain attenuation models and the one-year attenuation measurement campaign in Durban, South Africa.

This study further looks at the scattering amplitude of rain, signal attenuation, and phase shift due to rain. The approach of Pruppacher and Pitter, that assumes that the shape of raindrops is oblate spheroidal, is used for signal wavelengths in the millimeter range that approach the dimensions of the raindrop sizes. Results of the computation of the scattering amplitudes for varying angles of incidence for application in terrestrial links and for the vertical and horizontal polarizations for application in satellite links are presented. Results are also presented for the specific attenuation and phase shift.

1.2 Aims and Objectives

This research work focuses on the modeling of rain attenuation and depolarization effects over terrestrial and satellite communication links.

1.3 Methodological Approach

- (i) Data collection: Daily rainfall data for the period 2001 to 2010 was collected from the South African Weather Services' archives.
- (ii) Data sorting, processing, interpretation and statistical analysis.
- (iii) Development of rain attenuation models for spherical and non-spherical raindrops.
- (iv) Application of models and optimization.

1.4 Significance of the Study

Rain attenuation is the main drawback in the design of wireless networks that are highly reliable and optimal in performance. This is so because rain causes attenuation of the signal with varying degrees

of severity depending on the intensity, raindrop size, rain rate as well as the frequency of transmission. High rain rates at frequencies of operation beyond 10 GHz pose a serious challenge to the optimal performance of radio links and often cause complete signal outages (total unavailability of service). Thus there is a need to determine accurately the amount of attenuation caused by varying raindrop sizes and rain rates in both satellite and terrestrial links. Although some work has been done in this area in Southern Africa, it is hardly enough and is not conclusive in any way. Thus, there is the need for continued campaigns to determine accurate models of rain attenuation, raindrop size distributions, rain rates and the phase shift and depolarization effects caused by raindrops along the radio links. Much of the previous work was concentrated mainly on spherical raindrops and rain rate conversions. This work is focused on both spherical and non-spherical rain drops, as well as the depolarization effects and phase shift caused by non-spherical raindrops with emphasis on the oblate spheroidal raindrops. Similar rainfall attenuation studies have been done in Brazil [8, 9], Malaysia [10, 11], Singapore [12, 13] and Nigeria [14-16], among other regions albeit on a smaller scale.

1.5 Contributions

The following are the contributions in this work:

1. Both Gamma and Lognormal models for the rain drop size distributions have been developed using the method of moments.
2. Determination of measured and computed rain attenuation models for spherical and oblate spheroidal rain drops using the Mie scattering approach and the Pruppacher and Pitter rain drops shape technique for both terrestrial and satellite links for Southern Africa.
3. Characterization of depolarization effects and phase shift due to hydrometeors in radio links in South Africa.

1.6 Organization of the Thesis

The rest of this thesis is organized as follows:

In Chapter Two, a review of tropospheric precipitation and clear-air effects is presented. The different models that describe each of the different effects are presented. A short preview of the current situation on the work done so far by various authors in the area of rain fading in terrestrial and satellite links is also presented here.

In Chapter Three, rain attenuation in terrestrial and satellite links is presented. Rain rate experimental measurements are applied to compute the rain attenuation in terrestrial and satellite links. A total of nineteen sites are used for this case study, which employs the ITU-R models. In both the satellite and

terrestrial links, both the specific and total rain attenuation along the path is determined. This is done for vertical, circular and horizontal polarization at different frequencies.

In Chapter Four, rain drop size distribution models for the drizzle, widespread, shower and thunderstorm rain types are determined. These include the Lognormal and Gamma models which are developed using the method of moments. The models are validated by comparing them with others existing models in West Africa and Singapore using the root mean square error criterion. The models obtained are then applied in the determination of specific rain attenuation.

In Chapter Five, different total cross section models are employed in the computation of the specific attenuation. The method of moments is used in the raindrop size distribution modeling, while various extinction coefficients are used to calculate the specific rain attenuation. The total scattering cross section models of Morrison and Cross, Pruppacher and Pitter as well as the Mie technique are used. The results obtained are compared using the percentage difference between them.

In Chapter Six, oblate spherical raindrop models are applied to determine the scattering amplitude, scattering cross section and total cross section. The specific attenuation and phase shift due to rain at varying frequencies are then modeled and calculated using scattering amplitude and integrated over all the lognormal raindrop size distribution models using different rain types.

Chapter 2

Background Literature Review

2.0 Introduction

Today, there are a variety of roles played by satellites, among them are for forecasting of weather, Global Positioning Systems, In data gathering, earth observation, and, the most important ones being for communication purposes, navigation systems, and surveillance systems, and so on. Communication via satellite is applied in three main areas: fixed satellite, mobile satellite and broadcast satellite services. Current advancements in satellite technology have led to the emergence of new applications for satellite that include IP-based communications which support digital video services [17].

In the past, satellite communications took place in frequency bands like L (1/2 GHz), S (2/4 GHz) and C (4/6 GHz). As mentioned above, more and more advanced satellite applications have led to the congestion of the lower frequency bands, and utilization of higher frequency bands has become a necessity so as to support advanced services like video streaming, data communications and voice services, which form the bulk of today's communication needs. The current efforts are targeted towards the exploitation of the Ku band (12/14 GHz), the Ka band (20/30 GHz) and the V band (40/50 GHz) for better satellite service delivery. Thus, a full knowledge of the merits offered by these higher bands is necessary for service providers to fully tap into them. The higher bands offer the following benefits; larger bandwidth, frequency reuse, and better spectrum availability.

On a general scale, at these frequency bands, signal degradation as a result of atmospheric effects is a major issue mainly at frequency bands above 7 GHz in tropical and sub-tropical regions, and above 10 GHz in temperate regions. This in turn causes the level of system performance to drop. The atmospheric effects that are responsible for the signal degradation in satellite links occur in the troposphere as well as the ionosphere. Given that the effects that are originating from the ionosphere are only dominant at frequencies below 3 GHz, this frequency band forms part of the already congested lower frequency band. However, the effects that originate from the troposphere are the main concern of this work since they are dominant at frequencies greater than 3 GHz. The main sources of signal degradation at frequencies greater than 10 GHz include absorption by gases, attenuation due to clouds and fog, melting layer attenuation, attenuation due to rain, intersystem interference, sky noise effect, depolarization by rain and ice, scintillation effects, multipath fading and diffraction effects. Among these sources of signal degradation, attenuation due to rain, occurring mainly through scattering and absorption processes is the most predominant on both earth-space and terrestrial links [7, 18 – 32].

2.1 Tropospheric Propagation effects

The troposphere is the lowest layer of the atmosphere, situated between the earth and the stratosphere, in which there is a relatively large change in temperature with height. This is the region where convection is active and where clouds form. This region contains about 80% of the total air mass of the atmosphere and has a thickness that varies seasonally from 10 km in the polar regions to about 18 km in the tropical regions. This is the region where much of terrestrial propagation takes place. Some of the tropospheric effects in both clear air and precipitation conditions are discussed below.

2.1.1 Clear-air Effects

Tropospheric propagation clear-air effects are broadly categorized into atmospheric gaseous absorptive effects and refractive effects. Absorptive effects refer to molecular absorption of signal energy, leading to signal fading, by water vapour and oxygen in the troposphere. Refractive effects refer to the effects caused by the variation of the tropospheric refractive index with height, temperature, atmospheric pressure, relative humidity as well as atmospheric turbulence. These effects manifest themselves in terms of diffraction fading, multipath propagation, gaseous absorption and scintillation.

2.1.2 Diffraction fading

Diffraction fading (k-factor fading) takes place when the signal travelling from the transmitting antenna to the receiving antenna is intercepted by any obstacle. This kind of fading is a direct consequence of the refraction of radio wave as they traverse the lower atmosphere. As such, the radio path should be clear of any obstacles or a minimum path clearance criterion should be adhered to during terrestrial line of sight link planning as outlined in ITU-R Recommendation P.530-14 [33]. The degree of wave bending will determine whether or not electromagnetic waves are likely to be intercepted by obstacles along the radio link path. The degree of bending is usually modeled through the effective earth radius factor (k-factor). However, other quantities like the atmospheric radio refractivity, the atmospheric refractive index or the vertical refractivity gradient can also be used to characterize the refractive properties of the atmosphere. The refractive index, n , is the primary parameter used to describe refraction in the atmosphere. It is defined as the ratio of the velocity of an electromagnetic wave travelling in air to that in a vacuum (free space). It is given by [34]:

$$n = \frac{c}{v} = \sqrt{\mu\epsilon} \quad (2.1)$$

where c is the velocity of an electromagnetic wave in a vacuum (free space), v is the speed of a radio wave in air, μ is the relative permeability of air, ϵ is the relative permittivity of air.

Since the refractive index is very close to unity in the troposphere, $n = 1.000312$, the atmospheric radio refractivity, N , which defines the refractive index in parts per million is usually used to define the refraction and is given by [35, 36]:

$$N = (n - 1)10^6 = \frac{77.6}{T}P + 3.3 \times 10^5 \frac{e}{T^2} \quad (2.2)$$

where P is the atmospheric pressure (hPa), e is the water vapour pressure (hPa), and T is the absolute temperature (K).

From the foregoing equations, the point k-factor, k , is obtained from the following expression [37]:

$$k = \left[1 + \frac{\frac{dN}{dh}}{157} \right]^{-1} \quad (2.3)$$

where $\frac{dN}{dh}$ is the vertical refractivity gradient.

Atmospheric pressure, temperature, and water vapour content decrease with height above the earth's surface in the troposphere, but temperature will also increase with height in layers with temperature inversion in the troposphere. The decrease in dry air pressure and water vapour pressure is usually approximated as an exponential function of height. The variation of the tropospheric refractivity can also, as a result of these approximations, be approximated by an exponential function of height, as follows [38]:

$$N = N_s e^{-h/H} \quad (2.4)$$

where h is the height above the ground level, N_s is the surface level refractivity and H is the applicable scale height.

2.1.3 Multipath propagation (fading)

Multipath propagation occurs when a signal travelling from the transmitter to the receiver takes different paths. The main signal, that is the straight path signal, is then received together with other multiple copies that are delayed and attenuated. The delays and attenuations suffered will vary from one copy of the signal to the other depending on the route taken to the receiver, which at times could involve multiple reflections arising from the signal encountering obstacles along the path that are

much greater than its wavelength. Depending on the way the signals superimpose at the receiver, the net effect could be destructive (multipath fading) or constructive (multipath enhancement).

In [33], the ITU-R proposes three methods for the determination of multipath fading and enhancement in terrestrial line of sight links. They include:

1. Method for small percentages of time.
2. Method for all percentages of time.
3. Method for predicting enhancement.

For the small percentages method, both gross and detailed planning cases are considered. For the gross planning case, the percentage of time, ρ_w , a fade depth, A , that is exceeded in the average worst month is given by [33]:

$$\rho_w = Kd^{3.1}(1 + |\varepsilon_p|)^{-1.29} f^{0.8} \times 10^{-0.00089h_L - A/10} \% \quad (2.5)$$

where ε_p is the path inclination factor in radians, f is the frequency in GHz, h_L is the altitude of the smaller of the transmitting antenna and the receiving antenna and K is the geoclimatic factor, and is obtained using the following equation [33]:

$$K = 10^{-(4.6+0.0027dN_1)} \quad (2.6)$$

where dN_1 is the refractivity gradient in the lowest 65 m of the atmosphere not exceeded for 0.01% of the time of an average year.

For detailed link design, the percentage of time, ρ_w , a fade depth, A , is exceeded in the average worst month is given by [33]:

$$\rho_w = Kd^{3.4}(1 + |\varepsilon_p|)^{-1.03} f^{0.8} \times 10^{-0.00076h_L - A/10} \% \quad (2.7)$$

where all parameters are as defined in Equation (2.5), except K , the geoclimatic factor, which is obtained using the following equation [22]:

$$K = 10^{-(4.4+0.0027dN_1)}(10 + S_a)^{-0.46} \quad (2.8)$$

where dN_1 is as defined in Equation (2.6) and S_a is the terrain roughness factor.

Large signal enhancements are usually experienced under ducting conditions and for cases where the value is above 10 dB, the following equation is used [33]:

$$\rho_w = 100 - 10^{(-1.7-0.2A_{0.01}-E)/3.5} \% \quad (2.9)$$

where E is the enhancement in dB, ρ_w is as defined in (2.5) and $A_{0.01}$ is the attenuation exceeded for 0.01% of the time.

Thus, we can conclude that multipath fading is affected by the following [33, 39]:

- a) Point atmospheric refractivity gradient
- b) Frequency of operation
- c) Percentage of time a particular fade depth is exceeded.
- d) The height of the antennas
- e) The terrain roughness factor
- f) Inclination of the path

2.1.4 Absorption by Atmospheric Gases

Below 10 GHz electromagnetic wave signal absorption caused by atmospheric gases is negligible. There are three absorption peaks for the frequencies that are of interest to this study: an absorption peak at about 22 GHz due to water vapour, and two peaks due to absorption by oxygen that occur at about 60 GHz and at around 118 GHz.

The specific gaseous attenuation, γ , is given by [30]:

$$\gamma = \gamma_o + \gamma_w = 0.1820fN''(f) \quad \text{dB/km} \quad (2.10)$$

where γ_o is the specific attenuation due to dry air, γ_w is the specific attenuation due to water vapour, f is the frequency in GHz, and $N''(f)$ is the complex frequency-dependent refractivity imaginary part, and is given by [30]:

$$N''(f) = \sum_i S_i F_i + N_D''(f) \quad (2.11)$$

S_i is the strength of the i -th line, F_i is the shape factor of the line, and the sum extends over all the lines (for frequencies, f , above 118.75 GHz, only the oxygen lines above 60 GHz should be included in the summation), and $N_D''(f)$ is the dry continuum due to pressure-induced nitrogen absorption and the Debye spectrum.

The strength of the line is given by [30]:

$$S_i = a_1 \times 10^{-7} p \theta^3 \exp[a_2(1 - \theta)] \quad \text{for oxygen} \quad (2.12a)$$

$$S_i = b_1 \times 10^{-1} e \theta^{3.5} \exp[b_2(1 - \theta)] \quad \text{for water vapour} \quad (2.12b)$$

where p is the pressure of dry air (hPa), e is the partial pressure of the water vapour (hPa) and a_1, b_1, a_2, b_2 are coefficients.

2.1.5 Scintillation

This is another propagation effect associated with variations in the tropospheric refractive index, which results from changes in the refractive index with atmospheric turbulence. Atmospheric turbulence develops from wind shear due to a transfer of energy from larger to smaller eddies in the atmosphere. Associated with the turbulent eddies is a corresponding time-variable structure of temperature, water vapour density, and refractive index. The turbulent structure of the troposphere is largely responsible for the scattering of electromagnetic waves (the so-called troposcatter). For satellite communications our interest is in scintillation, phase fluctuations, and angle-of-arrival variations, which are effects of propagation through turbulent regions of the troposphere [40, 41, 42].

Some of the different models of scintillation are discussed below:

2.1.5.1 Karasawa, Yamada and Allnutt Model

This scintillation model is based on measurements that were carried out in Yamaguchi, Japan in the year 1983 at an elevation angle of 6.5° using an antenna of diameter 7.6m at the frequency range 11.5 to 14.23 GHz. The following model was developed [41]:

$$\sigma_{pre} = 0.0228(0.15 + 5.2 \times 10^{-3} N_{wet}) \times f^{0.45} \sqrt{G(D_c) / \sin^{1.3} \varepsilon} \quad dB \quad (2.13)$$

where σ_{pre} is the predicted scintillation intensity, N_{wet} is the wet part of the radio refractivity, f is the frequency in GHz, $G(D_c)$ is the antenna averaging function, D_c is the antenna effective diameter and ε is the angle of elevation.

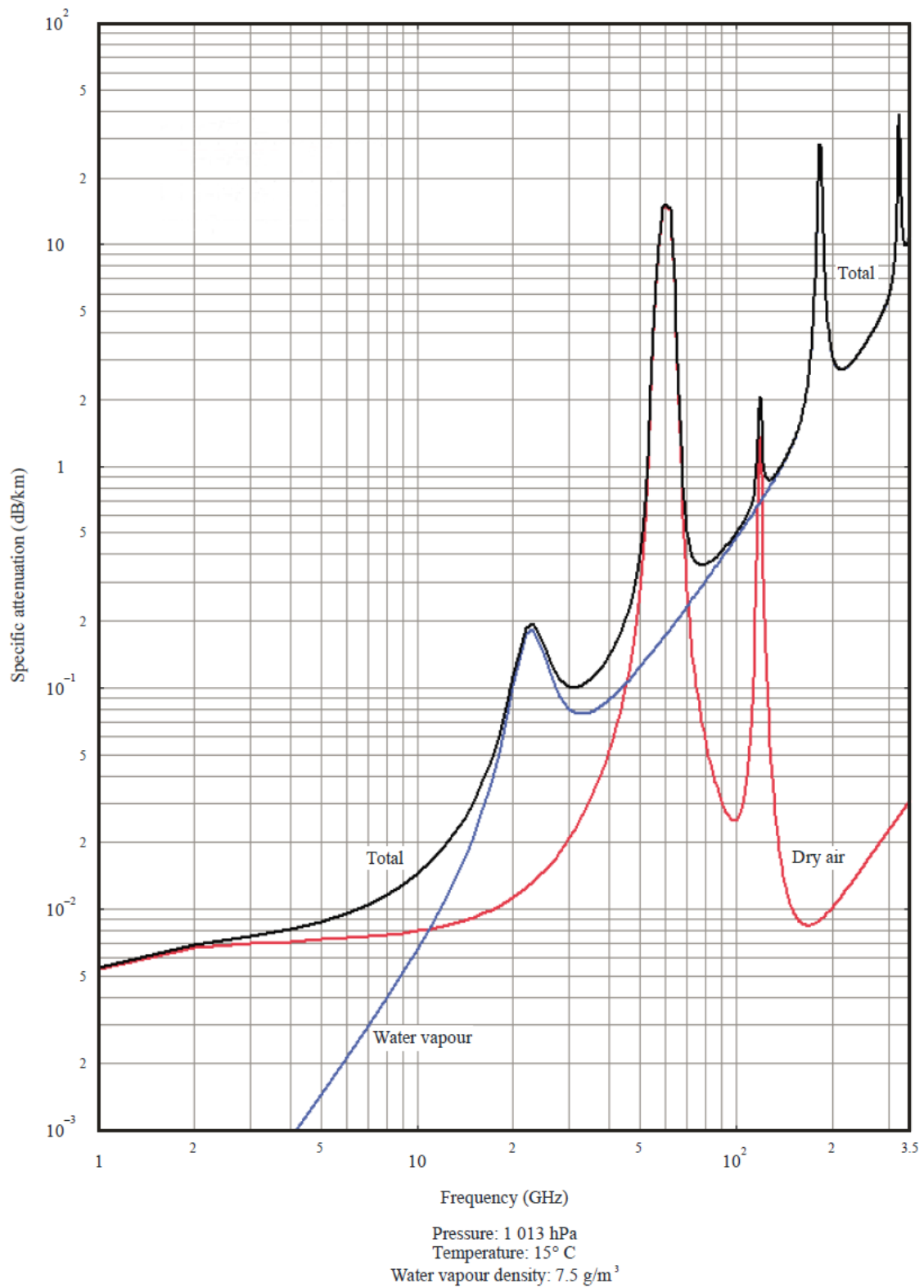


Figure 2.1: Specific Attenuation due to atmospheric gases [19]

2.1.5.2 The ITU-R Scintillation Model

This model is proposed for the frequency range 7 – 14 GHz and the averaging antenna aperture effects and the theoretical frequency dependence are used to estimate the average intensity of the scintillation, σ_{pre} , over a minimum period of one month. The model is summarized by the following equation [40]:

$$\sigma_{pre}^2 = \left[(3.6 \times 10^{-3} + 1.03 \times 10^{-4} N_{wet})^{2G_{HV}(D_e)} \right] \times f^{\frac{7}{6}} \sin^{2.4} \varepsilon \quad (dB^2) \quad (2.14)$$

where σ_{pre}^2 is the scintillation variance, $G_{HV}(D_e)$ is the Haddon and Vilar antenna averaging function. All other parameters are as defined in (2.13) above.

2.1.6 Hydrometeor Effects

The atmosphere, due to the many different gases, water and particles contained therein, which are collectively referred to as hydrometeors, absorbs and transmits many different wavelengths of electromagnetic radiation. Hydrometeors appear to radiowaves as lossy capacitors suspended in the atmosphere, causing both signal scattering and absorption that ultimately results in the reduction of channel capacity. The wavelengths that are able to penetrate the atmosphere without undergoing any absorption comprise what is known as the "atmospheric windows." Rain attenuation constitutes the main atmospheric effect here. At frequencies lower than 10 GHz, fading due to rain is not that pronounced, but, at higher frequencies, it is the main cause of poor link performance, especially in regions where rainfall is heavy. Additionally, apart from attenuation of signals, rain and other hydrometeors tend to cause depolarization [7, 43, 44].

2.2 Modeling of Different Propagation Impairments

The most important tropospheric effects that affect satellite communications at Ku- and Ka-band frequencies, together with their modelling based on ITU-R recommendations, are detailed below.

2.2.1 Rain Attenuation

Most communication systems at microwave and millimeter bands may experience a loss due to rain attenuation which temporarily makes the link unavailable for use at a given time. Rain attenuation depends on rain rate characteristics, rain shape, rain drop size, and volume density. In instances where the rain attenuation measurements are not available, the rain rate becomes an important parameter for estimating the level of fade due to the rain. An empirical relationship between the rain rate R (mm/hr) and the specific attenuation γ (dB/km) is given as [7, 31, 45]:

$$\gamma = aR^b \quad (dB/km) \quad (2.15)$$

where a and b are regression coefficients which depend on the drop shape of the falling raindrops, the raindrop density, the polarization and the frequency. The regression coefficients in equation (2.17) are computed by using ITU-R P.838-3 [31]:

$$a = [a_H + a_V + (a_H - a_V)\cos^2\theta \cos 2\tau]/2 \quad (2.16)$$

$$b = [a_H b_H + a_V b_V + (a_H b_H - a_V b_V)\cos^2\theta \cos 2\tau]/2a \quad (2.17)$$

where τ is the polarization tilt angle relative to the horizontal, θ is the path elevation angle, a_H is the constant for the coefficient for horizontal polarization, a_V is the constant for the coefficient for vertical polarization. In the case of linear vertical or horizontal polarization used for radio link transmission, the polarization tilt angle $\tau = 90^\circ$ for vertical polarization and $\tau = 0^\circ$ for horizontal polarization and $\tau = 45^\circ$ for circular polarization. The path elevation angle $\theta = 0^\circ$ as it is assumed that the angles of arrival and launch make an angle of 0° with the ground [33].

The total path attenuation is given as the product of specific attenuation γ (dB/km) and effective path length L_{eff} (km) between the transmitter and the receiver [7, 47]:

$$Att_{(0.01)} = aR^b \cdot L_{eff} \text{ (dB)} \quad (2.18)$$

where,

$$L_{eff} = \frac{d}{1+d/d_0} \text{ (km)} \text{ and } d_0 = 35e^{-0.015R_{0.01}} \quad (2.19)$$

where d is the path length and $R_{0.01}$ is the rain rate exceeded in 0.01% of the time. The fade depth is given at any desired availability for latitudes greater than 30 degrees, North or South as [7, 47]:

$$\frac{A_p}{A_{0.01}} = C_1 p^{-(C_2 + C_3 + \log_{10} p)} \quad (2.20)$$

where:

$$C_1 = (0.07^{C_0})[0.12^{(1-C_0)}] \quad (2.21a)$$

$$C_2 = 0.855C_0 + 0.546(1 - C_0) \quad (2.21b)$$

$$C_3 = 0.139C_0 + 0.043(1 - C_0) \quad (2.21c)$$

$$C_0 = \begin{cases} 0.12 + 0.4[\log_{10}(f/10)^{0.8}] & f \geq 10 \text{ GHz} \\ 0.12 & f < 10 \text{ GHz} \end{cases} \quad (2.21d)$$

where p is the desired probability (100% availability) often expressed as a percentage.

Figure 2.2 shows the variation of specific rain attenuation with frequency at three different rain rates computed for spherical raindrops at a water temperature of 0°C using *Laws and Parsons* [3] dropsize distribution.

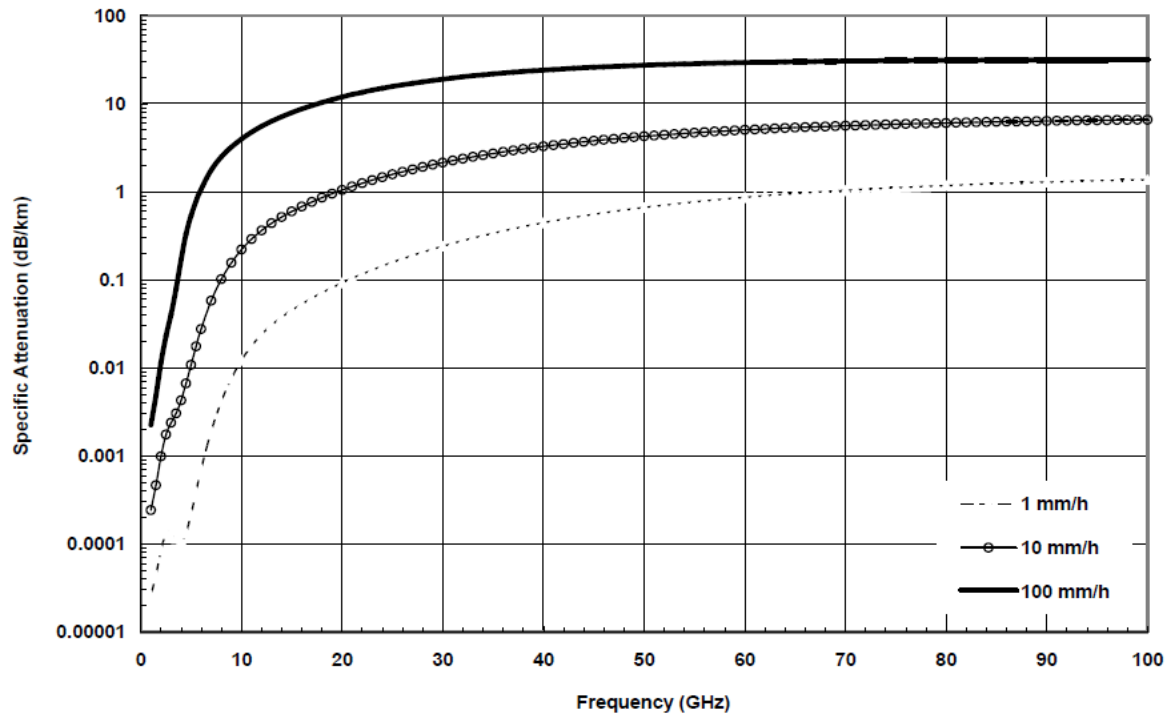


Figure 2.2: Specific attenuation caused by rain [7].

2.2.2 Cloud Attenuation

The cloud attenuation models that have been considered in this work are the Gunn and East model, the Liebe model, the Staelin model, the Slobin model, and the Altshuler model and they are all outlined below.

2.2.2.1 Liebe Model

Liebe, Manabe, and Hufford [48] used a double-Debye relaxation model of the complex permittivity of liquid water to derive an attenuation model for clouds, haze, and fog. This permittivity is then converted into refractivity values for conditions involving suspended water particles and the resulting specific attenuation, in dB/km, is given by [48, 49]:

$$\alpha = 0.182 \cdot f \cdot N''(f) \quad (2.22)$$

where f is the frequency (GHz) and $N''(f)$ is the loss spectrum (in parts per million), a function of frequency.

2.2.2.2 Altshuler Model

Altshuler [49, 50], realising the difficulty of measuring vertical liquid water and vapour profiles, correlated data of absolute surface humidity with measurements of zenith cloud attenuation and derived the following empirical equation [49, 50]:

$$\alpha = \left[-0.0242 + 0.00075\lambda + \frac{0.403}{\lambda^{1.15}} \right] (1.13 + \rho_1) \quad (2.23)$$

where λ is the wavelength (mm), ρ_1 is the surface absolute humidity (g/m^3), and α is the zenith attenuation (dB).

The total attenuation is obtained by multiplying this empirical equation by the distance $D(\theta)$ through the clouds, as defined below [49]:

$$D(\theta) = \text{cosec}\theta \quad \text{for } \theta > 8^\circ \quad (2.24a)$$

$$D(\theta) = [(a_e + h_e)^2 - a_e^2 \cos^2 \theta]^{1/2} - a_e \sin \theta \quad \text{for } \theta \leq 8^\circ: \quad (2.24b)$$

where θ is the elevation angle, a_e is the effective earth radius (8 497 km), $h_e = 6.35 - 0.302\rho$ is the effective cloud height (km) and ρ is the surface absolute humidity (g/m^3).

2.2.2.3 Gunn & East Model

This model is based on Mie's theory for spherical particles in a non-absorbing medium where Rayleigh approximation was used to calculate the total absorption cross-section of a spherical particle of water that is small compared to the wavelength of incident signal. In this model, cloud attenuation in dB/km, is given by [49, 51]:

$$\alpha = 0.4343 \left(\frac{6\pi}{\lambda \rho_d} \right) \text{Im} \left[-\frac{\varepsilon - 1}{\varepsilon + 2} \right] \rho_1 \quad (2.25)$$

where ε is the complex relative dielectric constant of water, λ is the wavelength (cm), ρ_d is the density of water (g/cm^3); ρ_1 is the liquid water content of the cloud (g/m^3), and Im denotes the imaginary part

2.2.2.4 Staelin Model

The Staelin model was developed from the classical theoretical work of Rayleigh and explicitly established that cloud attenuation is dependent on temperature. This is valid for frequencies between 10 GHz and 40 GHz and is given, in dB/km [49]:

$$\alpha = \frac{4.343\rho_1 10^{0.0122(291-T)^{-1}} \times 1.16}{\lambda^2} \quad (2.26)$$

where ρ_1 is the cloud liquid water density (g/m^3), T is the temperature (K); and λ is the wavelength (cm).

2.2.2.5 Slobin Model

The Slobin model makes use of the Staelin model where it divides clouds into twelve density categories, from clear air to heavy clouds, such as lighter cloud, light cloud, medium cloud, heavy cloud, heavier cloud, etc. [49].

2.2.3 Melting Layer Attenuation

A one-dimensional and stationary model was proposed by Salonen *et al* [52] in which the melting layer is assumed to be composed of spherical melting snow particles that are a mixture of ice, air and water. At the 0° C isotherm (at the top of the layer) the particles are a mixture of ice and air, and below the bottom all the melting particles have turned to raindrops. A one-to-one relationship between the melting particle and the corresponding raindrop is assumed where the particle mass is assumed to be invariant during the melting process. Size distribution and the average dielectric constant are used to characterize the melting particle.

The specific attenuation and zenith attenuation are then found by either using the Mie scattering theory or an approximation [52]:

$$\alpha = \lambda \int \Im(S)N(D)dD \quad (2.27)$$

where λ is the wavelength (mm), $\Im(S)$ is the imaginary part of the scattering amplitude in the forward direction and $N(D) = N_o D^\mu \exp(-\lambda D)$, is the modified Gamma distribution for raindrops.

2.3 The Current South African Situation

In South Africa the initial contributions by Owolawi [19] focused on the modeling of the characteristics of rain for both satellite and terrestrial links. His study focused on the rainfall rate integration time conversions, cumulative distributions, rain rate modelling as well as the raindrop size modelling. The author developed a factor for converting rainfall data from five-minute to one-minute integration time. Using the combined characteristics of three rain rate integration time techniques, viz., the empirical method, the physical method and the analytical method, he was able to develop a hybrid method for converting the rainfall rate data of long integration time to short integration time for South Africa and its surrounding Islands.

By letting N be the number of models generating different one-minute rain rate cumulative distributions, and P be the probabilities of rain rate exceedences; then the conversion factors (CF), for $P = 0.001, 0.003$ and 1 are given by [19]:

$$CF_{N=1,2,3\dots n} = \left(\frac{R_{1,1}(P_{0.001})}{R_{T,1}(P_{0.001})} \right) + \left(\frac{R_{1,2}(P_{0.001})}{R_{T,2}(P_{0.001})} \right) + \dots + \left(\frac{R_{1,n}(P_{0.001})}{R_{T,n}(P_{0.001})} \right) \quad (2.28)$$

$$CF_{N=1,2,3\dots n} = \left(\frac{R_{1,1}(P_{0.003})}{R_{T,1}(P_{0.003})} \right) + \left(\frac{R_{1,2}(P_{0.003})}{R_{T,2}(P_{0.003})} \right) + \dots + \left(\frac{R_{1,n}(P_{0.003})}{R_{T,n}(P_{0.003})} \right) \quad (2.29)$$

⋮

$$CF_{N=1,2,3\dots n} = \left(\frac{R_{1,1}(P_1)}{R_{T,1}(P_1)} \right) + \left(\frac{R_{1,2}(P_1)}{R_{T,2}(P_1)} \right) + \dots + \left(\frac{R_{1,n}(P_1)}{R_{T,n}(P_1)} \right) \quad (2.30)$$

With the assumption that the hybrid conversion factor $L_{i=0.001,0.003,\dots,1} = \frac{1}{N} \sum CF_{N=1,2,3\dots n,0.001}$, and the hybrid conversion factors for each exceedence percentage are $L_{i=0.001}$, $L_{i=0.003}$, $\dots, L_{i=1}$ respectively, then a general expression for the hybrid conversion factor is given by [19]:

$$L_{i=0.001,0.003,\dots,1} = \frac{1}{N} \sum CF_{N=1,2,3\dots n,0.001} \quad (2.31)$$

where $\sum CF_{N=1,2,3\dots n,0.001}$ is the rain rates ratio sum exceeded for a given percentage of time for rainfall with integration times T minutes and one minute for each number of distributions N .

Using the developed hybrid method, the author was able to demonstrate the superiority of his method in converting rain rate data from five-minute to one-minute integration time locally in Durban, South Africa. Additionally, the author was able to suggest a new classification of rain zones for South Africa

and the surrounding Islands using both Crane and ITU-R designations. Further, the author came up with simple models of the raindrop size distribution by employing the maximum likelihood estimation technique.

Odedina [7] dealt extensively with semi-empirical modelling of rain attenuation using rain rate, raindrop size distribution and signal level measurements on a 19.5 GHz link in Durban, South Africa. The choice of the semi-empirical technique was informed by the scattering nature of raindrops on electromagnetic waves. Various scattering raindrop amplitudes were determined at varying frequencies, by employing the Mie scattering approach on raindrops which are spherically shaped. From the said scattering amplitudes, different extinction cross-sections for the raindrops were computed.

For the real part of the computed extinction cross-sections, power-law regression was applied to determine the power-law coefficients at the different frequencies considered. The power-law model developed was then integrated over the raindrop size distribution models for the sake of developing theoretical models of rain attenuation. The empirical models, shown in Table 2.1, are the rain attenuation models obtained for the rainy months in Durban in the year 2004 using measurements on a 6.3 km long radio link.

Table 2.1: Monthly rain attenuation models for a 6.3 km link in Durban, South Africa, for 2004.

Calendar months	Empirical models
February	$A=0.0004R^3-0.012R^2+0.1642R+2.6184$
March	$A=0.0027R^3-0.0661R^2+0.8102R+0.1009$
April	$A=-0.0019R^3+0.0536R^2-0.0704R+0.9264$
October	$A=0.0002R^3-0.0149R^2+0.6024R-0.9477$
November	$A=0.1201R^2-0.1764R+1.3416$
December	$A=0.484R^{1.0992}$

The author was also able to develop empirically the annual power and logarithmic estimates for the measured minimum, average and maximum attenuation values. These equations are shown in Table 2.2 below.

Table 2.2: Analysis of the logarithmic and power regression estimates for the measured minimum, average and maximum attenuation values

Measured attenuation	Logarithmic equation	Regression coefficient	Power equation	Regression coefficient
Minimum	$A = 2.503\text{Ln}(R)-1.157$	0.922	$A = 0.578R^{0.789}$	0.886
Average	$A = 4.947\text{Ln}(R)-1.966$	0.917	$A = 1.892R^{0.618}$	0.948
Maximum	$A = 8.399\text{Ln}(R)-3.226$	0.887	$A = 3.112R^{0.6275}$	0.891

Rain attenuation results obtained from the measurements on a 19.5 GHz link that is horizontally polarized in Durban, South Africa were then compared with those obtained using other existing models for validation purposes. The author was also able to classify rain types in South Africa into four classes: thunderstorm, shower, widespread and drizzle.

B.T Maharaj [53], in his paper dwelt on the application of fade countermeasures to alleviate rain fade attenuation on earth-space links.

While the work in [7, 9, 53] is focused on rain rate conversions, raindrop size distributions, rain attenuation modelling for spherical raindrops and application of fade countermeasures to alleviate rain fade attenuation on earth-space links, determination of rain drop size distributions for Southern Africa for oblate spheroidal raindrops, and its use in the determination of signal attenuation through scattering and depolarization needs to be covered for Southern Africa. This is the main contribution in the current study.

2.4 Chapter Summary and Conclusion

In this chapter, a review of clear-air effects, scintillation effects, gaseous absorption, cloud attenuation and rain attenuation are been presented. Under clear-air effects, multipath and diffraction fading have been discussed. Two scintillation models have also been reviewed as well as five different cloud attenuation models. Gaseous attenuation has also been treated to a reasonable extent. Rain attenuation models have also been discussed with special mention of the specific and total attenuation. Finally, a summary of the current situation in South Africa has also been done with special mention of the main contributions in the PhD studies of Owolawi [19] and Odedina [7] in the same area. Overall, we conclude that rain attenuation presents the biggest threat to the design of reliable terrestrial and satellite links of high availability in South Africa.

Chapter 3

Characterization of Rain Attenuation in Terrestrial and Satellite Links in Southern Africa

3.0 Introduction

The first section of this chapter presents the application of results found in a rain rate characterizations study in South Africa and their application to terrestrial links. It further provides an analysis on rain fade in the light of the link distance chart and how it relates to the link budget. The outcomes are incorporated into the link budget to determine the maximum link distance and other performance parameters.

In the second section, an estimation is presented of the magnitude of attenuation due to rain at various frequencies for earth-space links based on the ITU-R model using the database of rainfall of over ten years for all provinces in South Africa. A link performance analysis using Intelsat IS 17 data is carried out for all provinces in South Africa from which are proposed reasonable, but adequate fade margins for all provinces in South Africa. Specific attention in terms of application is given to Ku and Ka bands which are of interest to communication systems designers in South Africa.

3.1 Terrestrial Rain Attenuation at Microwave and Millimetre-wave Frequencies in South Africa

This section presents the rain rate experimental measurements with the application of the International Telecommunication Union's Recommendations (ITU-R) on rain attenuation model in South Africa. Nineteen sites were chosen for this study, with at least one site from each province in South Africa. Figure 3.1 shows the map of South Africa. The parameters presented in this section are specific attenuation and total path attenuation for signals of horizontal, circular, and vertical polarizations and frequency in the range from 1 to 400 GHz through rain. The impact of rain attenuation on the system is evaluated by finding the link distance chart, and designing the link-budget at the chosen frequency range. The results of this work are useful in the planning of both microwave and millimeter-wave broadband wireless networks in South Africa such as Local-Multipoint-Distributed-Services (LMDS).

3.1.1 Introductory Concepts in Rain Attenuation

The interest of many telecommunication companies to provide high speed wireless internet access, broadcast multimedia information, multimedia file transfer, remote access to a local network, interactive video conference and Voice-Over-IP has forced migration from lower frequency bands

which are already congested to higher frequency bands such as microwave and millimeter-wave bands.



Figure 3.1: Map of South Africa [7]

The choice of these bands has become the key solution to today's needs because of large bandwidth availability, small device size and wide range of spectrum availability. Whilst there are a number of advantages that result from operating at these bands, rain, however, compromises optimum performance and usage of these bands. Rain attenuation results in outages that compromise the quality of signal and link availability rendering it as a prime factor to be considered in designing both terrestrial and satellite links. This means that the design of any communication device in this spectrum range requires knowledge of rain fade in order to provide optimum link availability and robust and reliable link to any telecommunication systems that offer the aforementioned benefits [28].

The performance metric considered mostly in link analysis is the system availability. That is, the time percentage the link is providing service either at or below the specified given bit error rate. It has been confirmed that at frequencies just above 5 GHz, the rain fade depth becomes noticeable and severe at frequencies above 10 GHz [54]. Rain rate measurement is one of the key aspects of rain needed to estimate the amount of rain fade, which is frequency and location dependent. The extensive work

carried out on the rainfall characteristics at different locations in South Africa has confirmed a dynamic distribution of rain rate in the region [19].

This section presents the application of results found in a rain rate characteristics study in South Africa as documented in [19] and their application to terrestrial links.

3.1.2 Cumulative Distribution of Rain Rate

For practical purposes, rain attenuation prediction is usually based on 1-minute rain rate distribution at a defined percentage of exceedence. The cumulative rain rate distribution for different locations in South Africa is presented in Figure 3.2. The method used in converting available rain data from 5-minute integration to 1-minute equivalent is presented in [55].

Table 3.1 shows a summary of rain rate value at 0.01% of exceedence which is acceptable signal availability threshold for radio systems to perform well. The lowest $R_{0.01}$ (rain rate at 0.01%) is recorded in the Western Cape Province at 27.3 mm/hr while the highest $R_{0.01}$ value is recorded in Mpumalanga province at 78.0 mm/hr.

As reported in [55], the conventional rain rate designations from both ITU-R and Crane were interpolated with available rain data to a proposed rain rate classification for South Africa. It was observed that the ITU-R P.835-5 under-estimates the rain rate values and Crane confirms likewise.

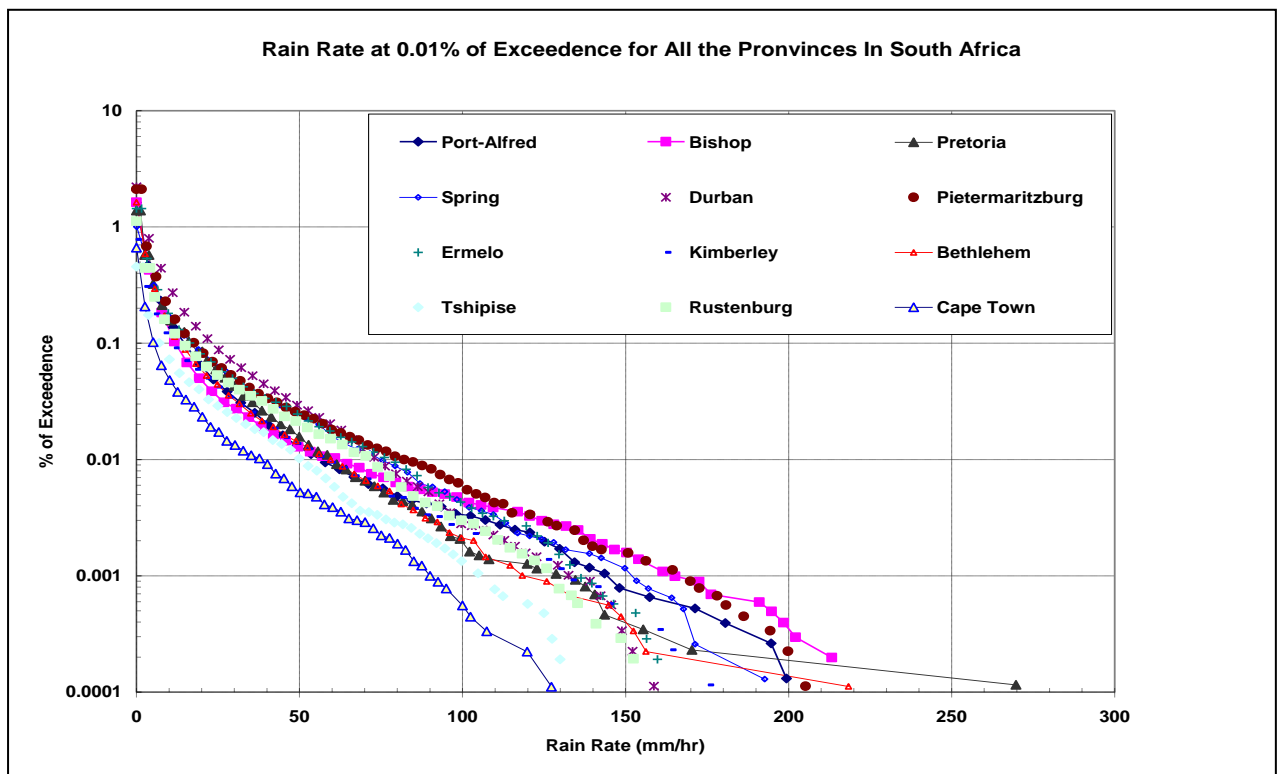


Figure 3.2: Average cumulative distribution of the rain rate in all provinces in South Africa

Also, rain rate contour map predicted using Crane and ITU-R rain rate models at 0.01% of exceedences are presented in [55]. In the contour maps, the inverse distance weighting (IDW) technique is employed because of its inherent advantage in the consistency of selecting grid points.

Table 3.1: Rain rate at 0.01% for all the Provinces in South Africa

South Africa Province/Site	Rain Rate at 0.01% mm/hr
Eastern Cape <ul style="list-style-type: none"> • Fort Beaufort • Bhisho • Umthatha • Port-Alfred 	53.0 57.0 70.0 58.0
Gauteng <ul style="list-style-type: none"> • Pretoria • Spring 	61.0 75.0
KwaZulu-Natal <ul style="list-style-type: none"> • Durban • Ladysmith • Pietermaritzburg 	63.0 75.0 79.0
Mpumalanga <ul style="list-style-type: none"> • Ermelo • Belfast • Nelspruit 	76.0 79.0 78.0
Northern Cape <ul style="list-style-type: none"> • Kimberley 	59.0
Free-State <ul style="list-style-type: none"> • Bethlehem • Bloemfontein 	60.0 67.0
Limpopo <ul style="list-style-type: none"> • Tshipise 	50.0
North West <ul style="list-style-type: none"> • Klerksdorp • Rustenburg 	67.0 70.0
Western Cape <ul style="list-style-type: none"> • Cape Point • Cape Town • Beaufort 	20.0 25.0 37.0

3.1.3 Specific Rain Attenuation Distribution for all the Provinces in South Africa

The distributions of specific rain attenuation of all the provinces in South Africa are shown in Figures 3.3 to 3.5 for horizontal, vertical and circular polarizations respectively. The results on the graphs are calculated using Table 3.2 coupled with the respective individual province rain rate at 0.01% of exceedences. The highest specific rain attenuations are recorded in Mpumalanga (Ermelo) and KwaZulu-Natal (Durban) provinces while the lowest is observed in the Western Cape (Cape Town). This is attributed to the low rain rate experienced by Cape Town. For horizontally polarized signals, the peak specific rain attenuation is observed at 200 GHz with the value of 28.65 dB/km and the lowest is 13.32 dB/km at the same frequency.

The majority of the provinces have their specific rain attenuation from 23.00 to 24.00 dB/km at the same frequency of 200 GHz. Using Figures 3.3 to 3.5, at the same frequency, it is observed that for horizontal, circular and vertical polarization predicted specific rain attenuation decreases respectively, though by small values. In addition, the figures confirm the expected increase in specific attenuation as rain rate increases. It seems constant above 100 GHz for the individual province rain rate. The reason may be due to the degree of impulse of raindrop shape to fast moving poles of electromagnetic waves at such high frequencies may not synchronise with each other.

Table 3.2: The specific attenuation parameters given by ITU-R [31]

Frequency GHz	a_H	a_V	b_H	b_V
1	0.000387	0.00000352	0.912	0.880
2	0.00154	0.000138	0.963	0.923
4	0.000650	0.000591	1.121	1.075
6	0.00175	0.0155	1.308	1.265
7	0.00301	0.00265	1.332	1.312
8	0.00454	0.00395	1.327	1.310
10	0.0101	0.00887	1.276	1.264
12	0.0188	0.0168	1.217	1.200
15	0.0367	0.0335	1.154	1.128
20	0.0751	0.0691	1.099	1.065
25	0.124	0.113	1.061	1.030
30	0.187	0.167	1.021	1.000
35	0.263	0.233	0.979	0.963
40	0.350	0.310	0.939	0.929
45	0.442	0.393	0.903	0.897
50	0.536	0.479	0.873	0.868
60	0.707	0.642	0.826	0.824
70	0.851	0.784	0.793	0.793
80	0.975	0.906	0.769	0.769
90	1.06	0.999	0.753	0.754
100	1.12	1.06	0.743	0.744
120	1.18	1.13	0.731	0.732
150	1.31	1.27	0.710	0.711
200	1.45	1.42	0.689	0.690
300	1.36	1.35	0.688	0.689
400	1.32	1.31	0.683	0.684

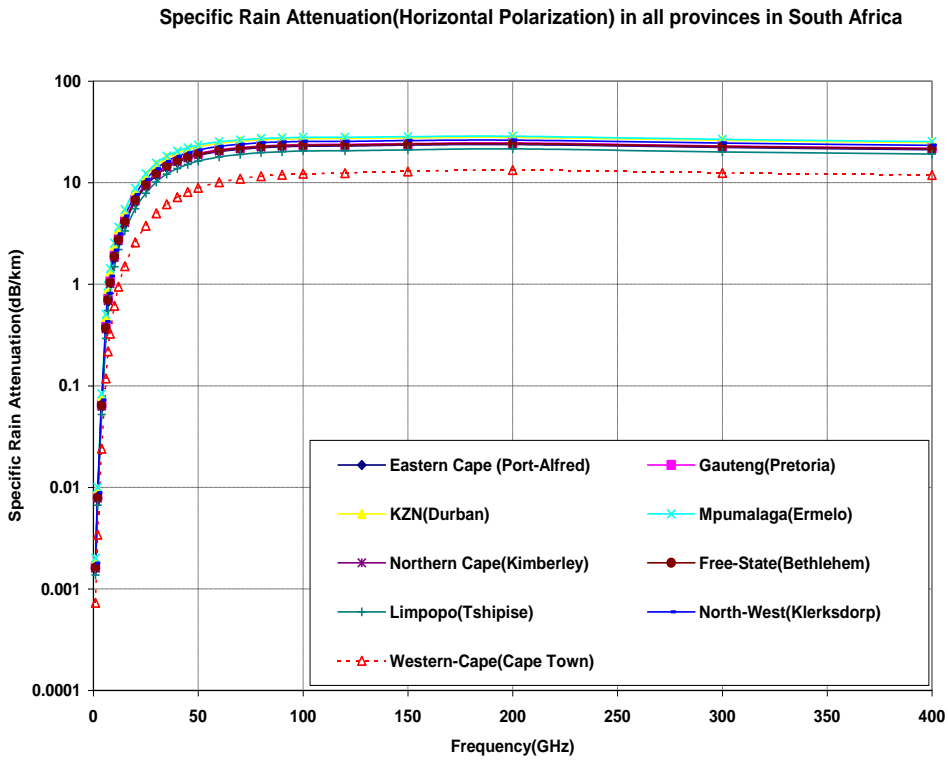


Figure 3.3: Frequency characteristics of specific rain attenuation for horizontally polarized signals for the Provinces in South Africa

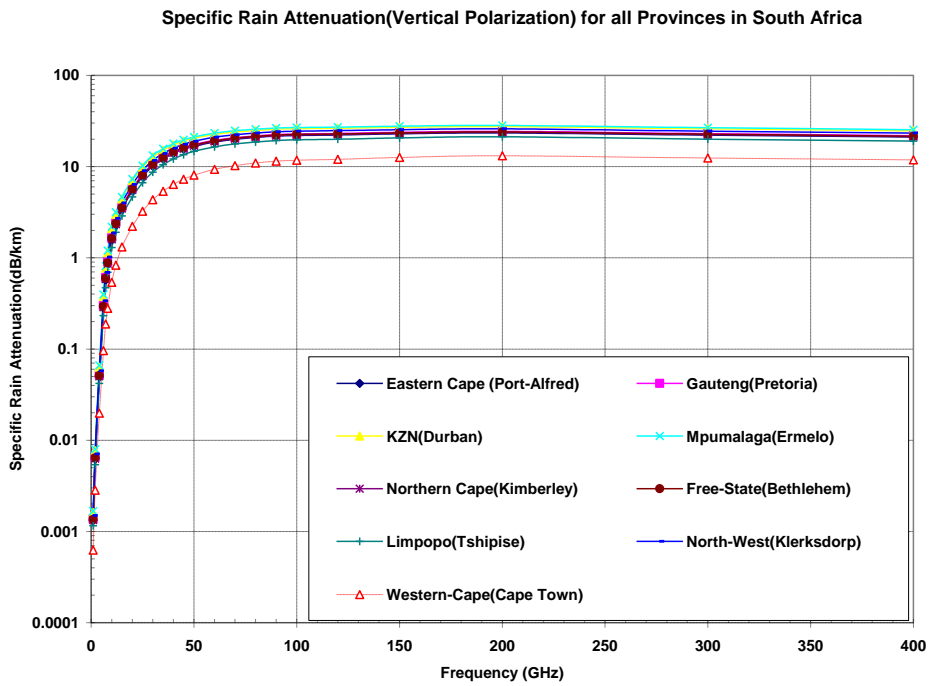


Figure 3.4: Frequency characteristics of specific rain attenuation for vertically polarized signals for the Provinces in South Africa

3.1.4 Estimation of total path attenuation for South African Provinces

The expected fade depth is calculated using Equation (2.20) with an effective path length. The characteristics of the fade depth at different polarization orientations in Durban with respect to propagation frequencies are shown in Figures 3.6a to 3.6c. The fade depth is observed at different distance ranges from 1 km to 60 km which is the valid ITU-R distance for the model. The steps to estimate rain attenuation using the ITU-R method are summarized as follows [56]:

1. Determine the rain rate at 0.01% of exceedence. This is done by measurement at 1-minute integration time as specified by the ITU-R or by using ITU-R P.837. In this work the former is considered to estimate the rain attenuation.
2. Compute specific rain attenuation at given polarizations, and rain rate of interest as given in Equations (2.17) – (2.19).
3. Compute the effective path length by as given in Equation (2.21), which will lead to the estimated path attenuation at 0.01% of exceedence in dB.
4. Estimate the attenuation exceeded for other percentages by using Equations (2.22) and (2.23).

According to ITU-R P.530-15, the prediction procedure outlined above is considered to be valid in all parts of the world at least for frequencies up to 100 GHz and path lengths up to 60 km.

The ratio of attenuation at any given percentage to attenuation at 0.01% of exceedence is given as 0.07 for p equal to 1.0, and for p equal to 0.1, 0.01, 0.001, the ratios are 0.36, 1.0 and 1.44 respectively. Here the fade margins are estimated for availability at 99.99% and at any availability that meets the needs of the operator.

Figures 3.5a – 3.5c show that the estimated total path attenuation increases with propagation frequencies up to 40 GHz as recommended by the ITU-R and this can be valid up to a hop length of 60 km. From 40 GHz to 200 GHz, the total path attenuation slightly increases with frequency with a dependency on the value of rain rate. There is a slight variation in total path attenuation with frequency above 100 GHz and the curves eventually level off, though not fully. Such small deviations could be due to errors associated with the measurements. These characteristics are visible in the three major polarization orientations of propagating signals at frequencies above 10 GHz.

South Africa falls under two important latitudes of ITU-R classifications as expressed in Equations (2.22) and (2.23). The majority of the provinces lie under the latitude that is less than 30 degrees and

the Eastern Cape and the Western Cape are the only provinces whose latitude is greater than 30 degrees.

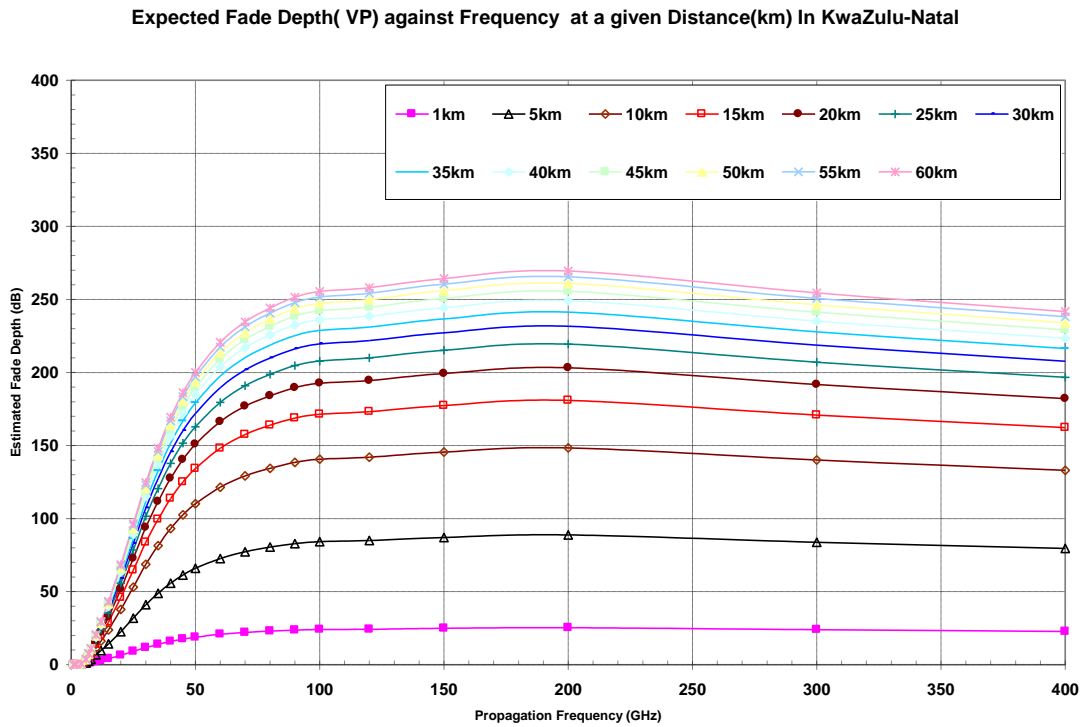


Figure 3.5a: Total path attenuation for vertically polarized signals at various frequencies

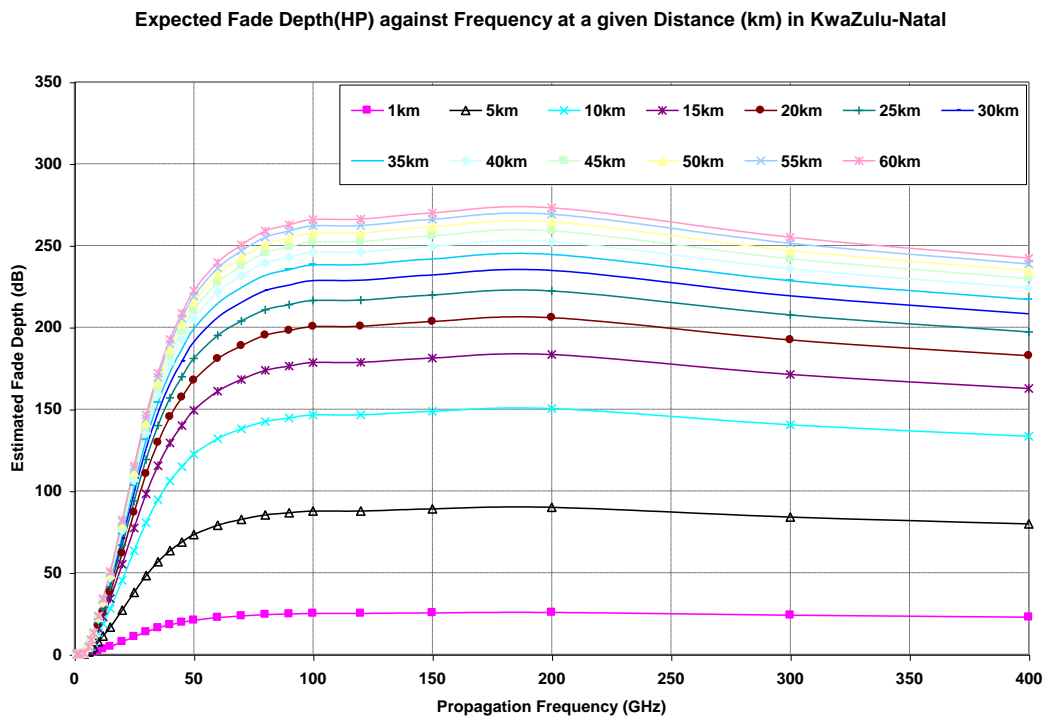


Figure 3.5b: Total path attenuation for horizontally polarized signals at various frequencies

Figures 3.5a and 3.5b represent KwaZulu-Natal province (Durban). In general, it is observed that the fade depth progressively increases starting from the vertical polarization, circular polarization and the highest fade depth is observed in horizontal polarization. This is because of the shape factor of the raindrop whose longer semi-major axis lies in the horizontal plane and that will result in the horizontally polarized signal travelling through a longer path length through water, thereby experiencing higher attenuation.

In the case of Durban, at 50 GHz, the fade depth is recorded as 18.81 dB for the 1 km path length for vertical polarization, while it is 19.0 dB and 20.90 dB for circular and horizontal polarization respectively. In another scenario in Durban, at 50 GHz, the fade depth is recorded as 255.4 dB for the 60 km path length in vertical polarization, while it is 202.12 dB and 222.30 dB for circular and horizontal polarization respectively. At 1 km path length, it is observed that the fade depth for Durban is more than what is recorded at Port-Alfred (that lies at latitude greater than 30 degrees) by an average of 14.78%.

In Figures 3.6a and 3.6b, the attenuation values at a defined availability percentage with the given frequency are presented. These were done for the two polarization states specifically for the Durban site in the KwaZulu-Natal Province and the Port Alfred site in the Eastern Cape Province. As shown in Figures 3.6a and 3.6b, the attenuation values at 99.999% availability for 20 GHz are 10.09 dB and 12.09 dB for vertical and horizontal polarization respectively for Durban. In the case of Port-Alfred the attenuation values at 99.999% availability for 20 GHz are 11.69 dB and 13.92 dB for vertical and horizontal polarization respectively. 99.999% availability, which translates to an outage of approximately 5 minutes a year, was used here as an illustration of the required fade margins at this stringent upper limit. In normal applications, fade margins for 99.99%, which translates to an outage of 53 minutes per year, suffice.

At the 30 GHz, the obtained attenuation values at 99.999% availability are 18.37 dB, 18.66 dB and 21.54 dB for vertical, circular and horizontal polarization respectively for Durban. For the Eastern Cape (Port-Alfred) the attenuation values at 99.999% availability are 21.62 dB, 21.95 dB and 25.26 dB for vertical, circular and horizontal polarization respectively. It can be seen that attenuation values decrease as the degree of availability decreases. For example in the case of Durban, the attenuation value is 10.09 dB at 99.999% and 2.55 dB at 99.9%. In addition, it is observed that attenuation values at latitudes less than 30 degree are less when compared with values at latitudes greater than 30 degrees as reflected in the figures at equal performance. The percentage differences between KwaZulu-Natal (Durban) and Eastern Cape (Port-Alfred) at an availability of 99.999% falls within 15.86% and for the 99.9% the least percentage difference is 25.75%.

For easy application of these results, any link design engineer can use frequency scaling to find the estimated attenuation value for the undetermined frequency in the reading as given in ITU-R P.530. Based on ITU-R link outages performance yard stick, 99.99% availability translates to approximately 53-minutes of outage per year while 99.999% availability translates to approximately 5-minutes of outage per year.

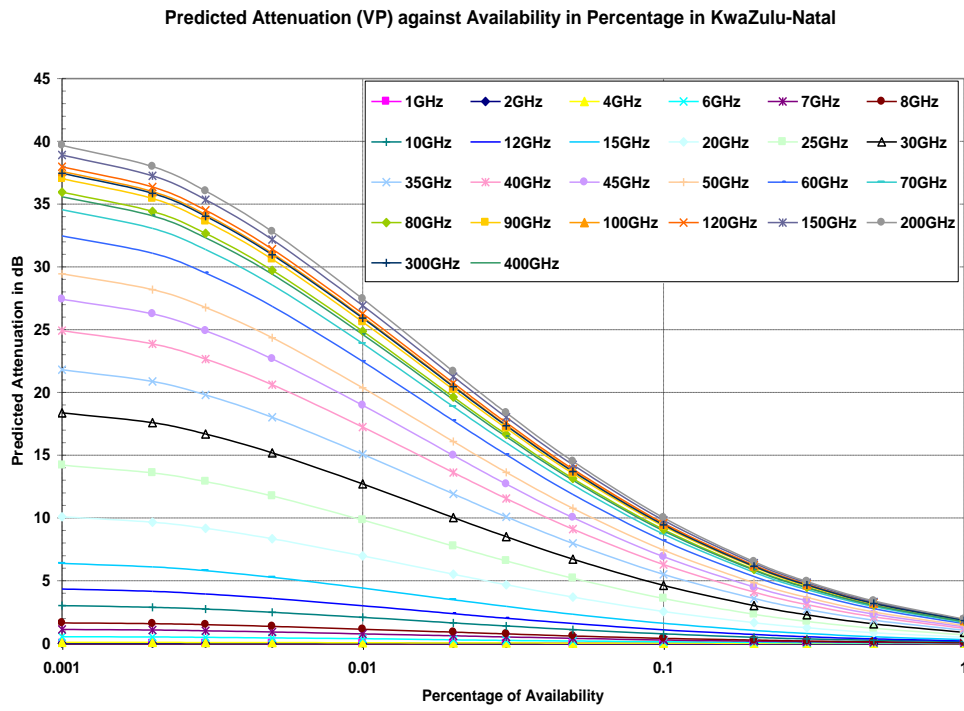


Figure 3.6a: Predicted Rain Attenuation (VP) against Availability

Predicted Attenuation (CP) against Availability in Percentage in KwaZulu-Natal

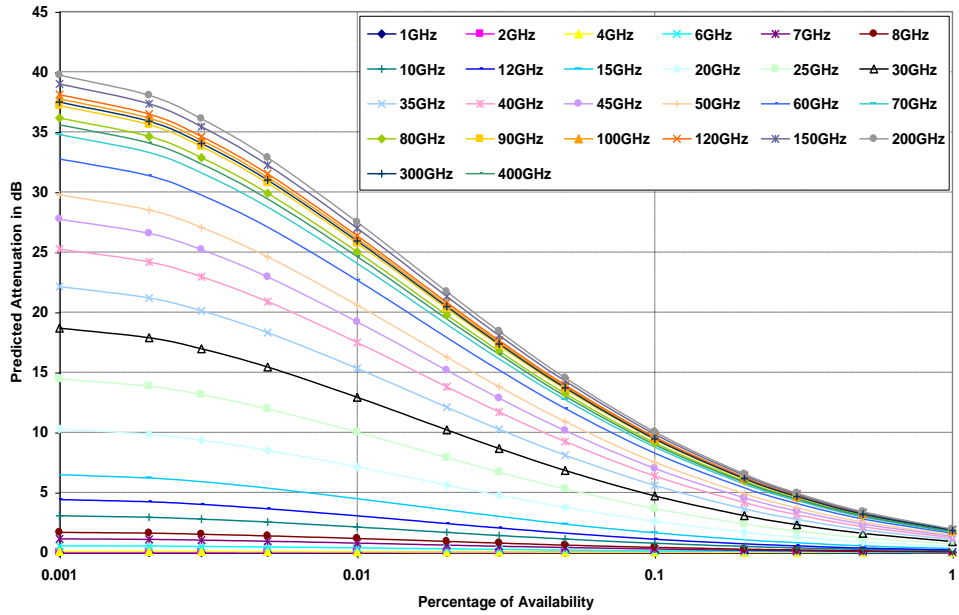


Figure 3.6b: Predicted Rain Attenuation (CP) against Availability

Predicted Attenuation (HP) against Availability in Percentage in KwaZulu-Natal

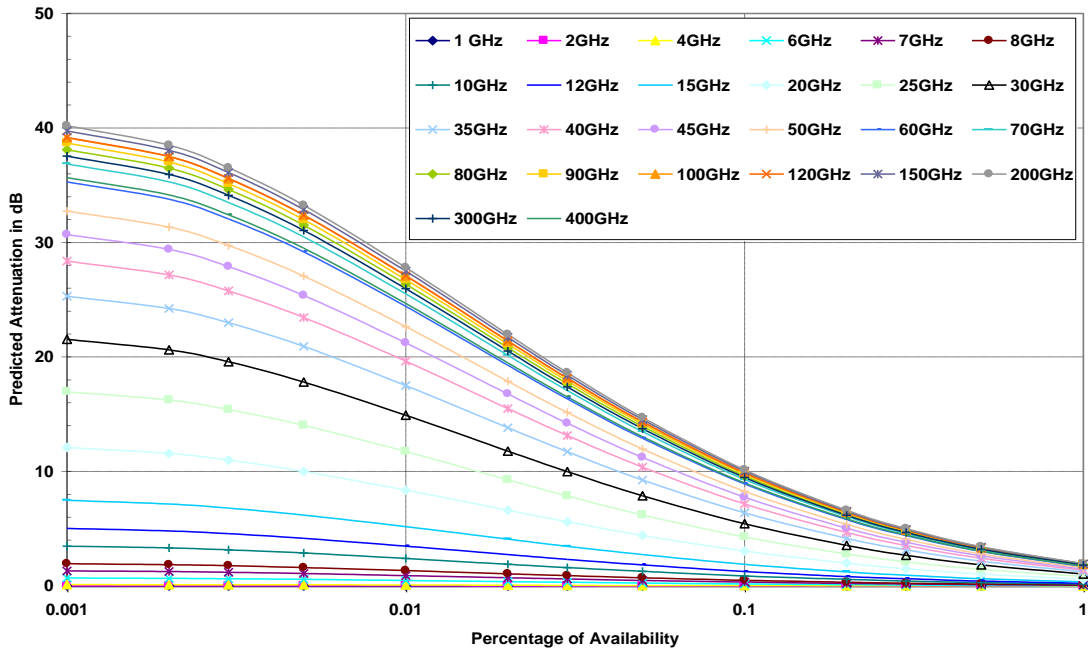


Figure 3.6c: Predicted Rain Attenuation (HP) against Availability

3.2 Rain Attenuation at Ka, Ku and V Bands for Satellite Links in South Africa

Despite the fact that over twenty (20) fibre optic cable networks have been rolled out in Africa, the satellite infrastructure continues to fulfill an important role in providing

communication access to rural, remote and inland areas across the globe. The fast growth in telecommunications, increased demand for bandwidth, congestion in lower frequency bands and miniaturization of communication equipment have forced the designers to employ higher frequency bands such as the Ku (12 to 18 GHz), Ka (26.5 to 40 GHz), and V (40 to 75 GHz) bands. Rain is the most deleterious source to signal propagation in these bands. The contribution of rain attenuation to the quality of signal in these bands, especially in the tropical and subtropical bands in which South Africa is located, needs to be studied. The aims of this section are to estimate the magnitude of rain attenuation using the ITU-R model, carry out link performance analysis, and then propose reasonable, adequate fade margins that need to be applied for all provinces in South Africa.

3.2.1 Introduction to earth-space links in South Africa

Consumer diversity, demands for bandwidth, and service convergence have led to a tremendous growth in communication systems. These have resulted in congestion at lower frequency bands, and consequently increased the need for higher frequency band usage. At these frequencies, however, the presence of rain causes degradation of signals, especially above 10 GHz [54]. The many advantages of telecommunications systems operating at higher frequencies include: large bandwidth, increased frequency reuse, small device size and wide range of spectrum availability. The major obstacle to these frequency ranges is rain. In South Africa, extensive studies done by Owolawi [55] have revealed the existence of different climatic zones in the country. In recent years, the roll-out of fibre optic networks has not diminished the importance of satellite communication systems, especially for rural, remote and inland cities across the globe. The earlier satellite networks operate at L, S, C, and X bands, while the recent ones start operating at Ku, K, Ka, Q and V bands.

Demand for broadband service is exhausting the available capacity of existing C- and Ku-band satellite networks. The recent motivation by Hughes to support Vodacom South Africa in their latest coverage expansion, by providing the first Ka-band satellite that will provide broadband internet access to South Africa and other African countries, is the key reason behind this work. The impacts of rain rate along the satellite path in Southern Africa, where mixed climate conditions of tropical, subtropical and temperate are common, demand special attention with respect to rain attenuation modeling [28, 57]. Electromagnetic waves passing through rain at any of these frequency bands will be absorbed or scattered. This scattering and absorption processes constitute rain attenuation. The attenuation caused by the rain depends on parameters such as the size of raindrops, rain temperature, drop velocity, polarization, rain rate, drop orientation and transmitting frequency. Since rain attenuation is the primary obstacle to good quality and availability of signal at these bands, the development of rain attenuation models has been the focus of many researchers, and several

measurement campaigns, theoretical and analytical models have been established. Many rain attenuation models, both for terrestrial and satellite paths, are semi-empirical in nature due to the lack of accurate characterization of the various sources that produce the impairments. Rain attenuation is estimated by integrating the specific attenuation along the earth-space path. The specific rain attenuation is mathematically calculated by using empirical parameters such as the cumulative distribution of one-minute rain rate at a given probability of exceedence. In this section, estimated specific rain attenuation at various satellite frequency bands is proposed, based on the ITU-R recommendations [33, 58], using a database of rainfall of over ten years in all the provinces in South Africa. Specific attention is given to Ku and Ka bands, which are of interest to systems designers and telecommunications operators alike.

3.2.2 Rain Height

The estimation of rain attenuation along a slant-path in a satellite link requires an understanding of the rain height. The method, adopted by ITU-R, assumes the rain structure to be uniform from the ground level to the $0^{\circ}C$ isotherm height, h_R , simply termed the effective rain height. Often, an empirical formula is used to estimate the value of h_R due to the scarcity of measured data. Most of the referenced rain height experiments were done in Europe and Asia, and very little data is available in Africa except in West Africa [32, 59 – 62]. As a result, the current work uses the latest ITU Recommendation P.839-3 [32]. Though the model is less accurate, it is widely employed to calculate the average rain height. The mean rain height above mean sea level is expressed as [32]:

$$h_R = h_0 + 0.36km \quad (3.1)$$

where h_0 is the average annual $0^{\circ}C$ isotherm height. If the h_0 is not available from local data, a global contour map is used, as presented in reference [32], and bilinear interpolation is used to determine any unavailable grid line on the map.

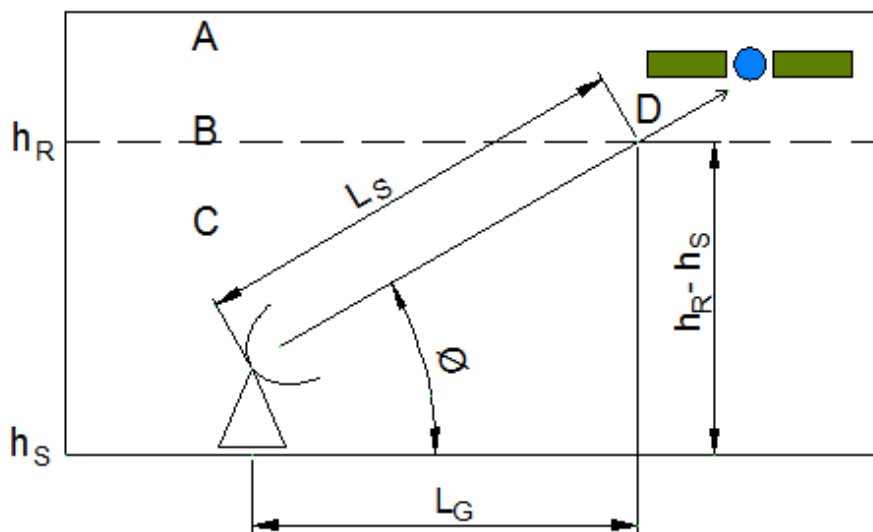
Table 3.3: Average rain rate at 0.01% for all provinces in South Africa

South Africa Province/Site	Rain Rate at 0.01% (mm/hr)	Lat/Long
Eastern Cape (Fort Beaufort)	53 mm/hr	-32.7/26.6
Gauteng (Pretoria)	61 mm/hr	-25.7/28.1
KwaZulu-Natal (Durban)	63 mm/hr	-29.9/30.9
Mpumalaga (Ermelo)	76 mm/hr	-26.4/29.9
Northern Cape (Kimberley)	59 mm/hr	-28.7/24.7
Free-State (Bethlehem)	60 mm/hr	-33.9/18.9
Limpopo (Tshipise)	50 mm/hr	-22.6/30.1
North West (Klerksdorp)	67 mm/hr	-26.8/26.6
Western Cape (Cape Town)	25 mm/hr	-33.9/18.6

3.2.3 Slant Path Rain Attenuation Models

In this subsection, a rain attenuation model is presented that has performed well for temperate regions and different rain types. This rain attenuation model is the ITU-R model, which is the most widely accepted international method and benchmark for comparative studies. This model is semi-empirical and often employs the local climatic parameters at a desired probability of exceedence.

3.2.3.1 ITU-R Rain Attenuation Model



- A: Frozen precipitation
- B: Rain height
- C: Liquid precipitation
- D: Earth-space path

Figure 3.7: Slant path through rain [28]

The ITU-R 618-10 [28] gives summarized procedures for the computation of rain attenuation on a satellite path. In order to compute the slant-path rain attenuation using point rainfall rate, the following parameters are required [28, 57]:

- f : the frequency of operation in GHz
- θ : the elevation angle to the satellite, in degrees
- φ : the latitude of the ground station, in degrees N and S
- h_s : the height of the ground station above sea level, in km

R_e : effective radius of the Earth (8 500 km)

$R_{0.01}$: point rainfall rate for the location of interest for 0.01% of an average year (mm/hr)

Step-by-step procedures for the computation of the rain attenuation along the slant-path of a satellite system are summarized as follows [28, 57]:

Step 1: Determine the rain height, h_R , as given in (3.1) and contour map in Recommendation ITU-R P.839 [32].

Step 2: Determine the slant-path length and the horizontal projection.

The slant-path length L_s , expressed in km, is calculated from [28]:

$$L_s = \begin{cases} \frac{(h_r - h_s)}{\sin\theta} & \text{for } \theta \geq 5^\circ \\ \frac{2(h_r - h_s)}{\sqrt{\left(\sin^2\theta + \frac{2(h_r - h_s)}{R_e}\right)} + \sin\theta} & \text{for } \theta < 5^\circ \end{cases} \quad (km) \quad (3.2)$$

The horizontal projection is then expressed as [28]:

$$L_G = L_s \cos(\theta) \quad (3.3)$$

where L_G and L_s are in km.

Step 3: Determine the rain rate at 0.01% for the location of interest over an average year. In this work, Table 3.3 is used, which is a derived rain rate at one-minute integration time at 0.01% of exceedance from long-term local data.

Step 4: Calculate the specific attenuation, a function of desired frequency, polarization and rain rate using (2.17).

Step 5: Calculate the horizontal reduction factor, $r_{0.01}$ at 0.01% probability, expressed as [28]:

$$r_{0.01} = \frac{1}{1 + 0.78 \sqrt{\frac{L_G \gamma_R}{f}} - 0.38(1 - e^{-2L_G})} \quad (3.4)$$

Note: L_G is the horizontal projection as determined in Step 2 and f is the operating frequency measured in GHz.

Step 6: Calculate the vertical adjustment factor, $v_{0.01}$, for 0.01% of the time [28, 57]:

$$v_{0.01} = \frac{1}{1 + \sqrt{\sin(\theta)} \left[31 \left(1 - e^{-(\theta/1+x)} \right) \frac{\sqrt{L_R \gamma_R}}{f^2} - 0.45 \right]} \quad (3.5)$$

$$L_R = \begin{cases} \frac{L_G r_{0.01}}{\cos \theta} \text{ km for } \xi > \theta \\ \frac{(h_R - h_s)}{\sin \theta} \text{ km for } \xi \leq \theta \end{cases} \quad (3.6)$$

and

$$\xi = \tan^{-1} \left(\frac{h_R - h_s}{L_G r_{0.01}} \right) \text{ deg rees} \quad (3.7)$$

$$x = \begin{cases} 36 - |\varphi| \text{ deg rees} & \text{for } |\varphi| < 36 \\ 0 & \text{for } |\varphi| \geq 36 \end{cases} \quad (3.8)$$

Step 7: The effective path length is then computed from [28, 57]:

$$L_E = L_R v_{0.01} \text{ km} \quad (3.9)$$

Step 8: Calculate the attenuation exceeded for 0.01% of an average year [28, 57]:

$$A_{0.01} = \gamma_R L_E \text{ dB} \quad (3.10)$$

The attenuation value for other percentages of exceedence is determined by using the expression below [28, 57]:

$$A_p = A_{0.01} \left(\frac{p}{0.01} \right)^{-[0.655 + 0.033 \ln(p) - 0.045 \ln(A_{0.01}) - \beta(1-p) \sin(\theta)]} \text{ dB} \quad (3.11)$$

where,

$$\beta = \begin{cases} 0 & \text{if } p \geq 1\% \text{ or } |\varphi| \geq 36^\circ \\ -0.005(|\varphi| - 36) & \text{if } p < 1\% \text{ and } |\varphi| < 36^\circ \text{ and } \theta \geq 25^\circ \\ -0.005(|\varphi| - 36) + 1.8 - 4.25 \sin \theta & \text{otherwise} \end{cases} \quad (3.12)$$

The results obtained in this section make use of the Intelsat 17 (IS-17) satellite located at 66° E, as its service footprint covers the area of study adequately. The geo-characteristic parameters for each

location are shown in Table 3.4. In this table the attenuation values (in dB) that are expected for 0.01% of the time and the effective path lengths (in km) for frequencies ranging from C-band up to V-band for circular, horizontal, and vertical polarizations are shown.

The elevation angle for each region is also shown (in degrees). The elevation angle is the angle between the horizontal along the earth's surface and the center line of the satellite's transmission beam as shown in Figure 3.8. This angle translates into the visibility (coverage) of the horizon to the satellite's beam, with an angle of zero degrees, ensuring visibility from all directions (ideal case). Rainfall attenuation, however, is strongly dependent on two factors: the operating frequency and the local rain rate. The results in Table 3.4 show that the area with the lowest rain rate at 0.01% exceedence (Cape Town with a value of 25 mm/h) will experience the least attenuation for the same percentage of exceedence at a given frequency. Conversely, it is true that the area with the highest rain rate at 0.01% exceedence (Ermelo with a value of 76 mm/h) experiences the highest signal degradation for the same percentage of exceedence at a given frequency.

The results of Table 3.4 are also displayed graphically in Figure 3.9 and Figure 3.10. Figure 3.9 shows the variation of the attenuation at 0.01% of exceedence with frequency, for all the areas under study. The effects of polarization are also shown as this is a consideration for antenna polarity needed by system designers.

The effective path length for each region is determined and its dependency on frequency and elevation angle is evident. This length is used instead of the actual geometric length due to the non-uniformity of rain density as the signal travels through a rainy medium. The location with the lowest elevation angle exhibits the longest effective path length (Cape Town with an elevation angle of 26.4 degrees).

However, the results in Table 3.4 suggest that the variability of local rain rate has an influence on the effective path length. Notwithstanding this observation, the general conclusion can still be drawn that areas of high elevation exhibit short effective path lengths given the small contribution due to varying local rain rates. Unlike attenuation, the effective path length depends strongly on elevation angle and frequency of operation. These results are displayed graphically in Figure 3.9 to show the variability of the effective path length with frequency for each location.

The elevation angles give designers an idea as to the positioning of ground station antennas for maximum energy transfer with little to no tracking required (considering geostationary orbit satellites). All the areas under study have an elevation angle above 25 degrees, which permits the use of the approximation given in the first condition of Equation (3.2).

Figures 3.8 (a) – 3.8 (c) show the attenuation expected to be exceeded for 0.01% of the time in an average year. The fade margins are higher for horizontally polarized signals as expected while the vertical polarization gives lower fade margins. Circularly polarized electromagnetic waves (EM) experience a fade margin whose value lies between that of horizontally and vertically polarized signals. Different polarizations are chosen by service providers for different reasons such as cross-polarization discrimination and frequency reuse.

Figures 3.9 (a) – 3.9 (c) show how the effective path length changes as the frequency of operation changes. At lower frequencies, such as C-band, the effective path length is quite long but decreases almost exponentially around Ku-band frequencies. As frequency increases into the Ka-band frequencies, the effective path length maintains a uniform value. It also appears that at V-bands, the effective path length begins to increase consistently with increasing frequency. The increase is, however, steady but could be rapid at millimetre bands.

Table 3.4: Characteristics for Locations in South Africa at 0.01% time of exceedence

Location	R _{0.01}	Frequency (GHz)	Elevation Angle (°)	Attenuation for 0.01% of time and Effective path length					
				Circular		Horizontal		Vertical	
				A _{0.01} (dB)	L _E (km)	A _{0.01} (dB)	L _E (km)	A _{0.01} (dB)	L _E (km)
Bethlehem	60 mm/hr	4	26.7°	0.4609	10.1799	0.7474	9.9343	0.4163	10.2298
		8		7.3072	6.6407	7.8191	6.4013	6.7780	6.9178
		12		16.2329	6.0082	17.4814	5.7842	15.1020	6.2317
		18		30.1983	5.7685	32.8390	5.5319	27.9804	5.9885
		26.5		50.9177	5.6110	54.7199	5.4154	47.2461	5.8180
		40		80.8603	5.6080	84.6843	5.4842	77.0819	5.7377
		48		95.0743	5.7014	98.7186	5.6002	91.4850	5.8060
		75		127.9248	6.1725	130.1286	6.1247	125.7473	6.2207
Cape Town	25 mm/hr	4	26.4°	0.1487	10.7497	0.1972	10.6436	0.1468	10.7542
		8		3.7325	11.4095	4.2487	11.7503	3.4142	11.6610
		12		8.3613	8.4816	8.8294	8.2262	7.9403	8.7469
		18		16.3508	7.7663	17.3737	7.5455	15.4870	7.9725
		26.5		28.7665	7.3542	30.5685	7.1546	27.0192	7.5667
		40		48.5640	7.1193	50.5434	6.9941	46.6038	7.2507
		48		58.6595	7.1351	60.5617	7.0352	56.7809	7.2384
		75		83.0914	7.5077	84.2548	7.4621	81.9398	7.5538
Durban	63 mm/hr	4	38.4°	0.4816	8.1551	0.8218	7.9794	0.4259	8.1937
		8		8.1321	5.6319	8.7098	5.4286	7.5383	5.8699
		12		17.3709	5.1296	18.8020	4.9335	16.0839	5.3265
		18		31.6598	4.9314	34.6613	4.7227	29.1568	5.1265
		26.5		52.6433	4.8044	56.8030	4.6357	48.6474	4.9835
		40		82.1961	4.8207	86.2863	4.7139	78.1667	4.9327
		48		95.9097	4.9088	99.7862	4.8211	92.1017	4.9996
		75		127.0373	5.3261	129.3459	5.2840	124.7595	5.3686
Ermelo	76 mm/hr	4	39.7°	0.5138	8.2385	0.8933	8.1325	0.4516	8.2636
		8		8.6734	5.6807	9.3008	5.4813	8.0292	5.9142
		12		18.2123	5.1343	19.7456	4.9401	16.8361	5.3293
		18		32.8177	4.9020	35.9913	4.6949	30.1757	5.0957
		26.5		54.1693	4.7560	58.5035	4.5891	50.0101	4.9330
		40		84.0374	4.7618	88.2608	4.6563	79.8791	4.8727
		48		97.8242	4.8466	101.8174	4.7596	93.9033	4.9365
		75		129.0140	5.2551	131.3815	5.2133	126.6785	5.2973
Fort Beaufort	53 mm/hr	4	33.3°	0.3368	8.7993	0.5302	8.5952	0.3080	8.8367
		8		6.1075	6.5913	6.5193	6.3420	5.6892	6.8905
		12		13.7248	5.8600	14.7515	5.6521	12.7973	6.0690
		18		25.7554	5.5977	27.9455	5.3837	23.9189	5.7971
		26.5		43.7342	5.4298	46.9708	5.2515	40.6136	5.6188
		40		70.0710	5.4034	73.3646	5.2908	66.8201	5.5215
		48		82.6717	5.4802	85.8119	5.3884	79.5812	5.5752
		75		111.8571	5.8989	113.7500	5.8556	109.9874	5.9428
Kimberley	59 mm/hr	4	34.1°	0.4044	9.1377	0.6622	9.0411	0.3649	9.1579
		8		7.0987	6.6031	7.6019	6.3706	6.5850	6.8785
		12		15.4464	5.8288	16.6621	5.6238	14.3513	6.0346
		18		28.3315	5.5074	30.8583	5.2936	26.2182	5.7067
		26.5		47.3760	5.3057	50.9807	5.1294	43.9060	5.4926
		40		74.8319	5.2650	78.4266	4.1535	71.2862	5.3819
		48		87.8138	5.3380	91.2260	5.2468	84.4577	5.4323
		75		117.6630	5.7461	119.7047	5.7029	115.6469	5.7898
Klerksdorp	67 mm/hr	4	36.7°	0.4595	8.7393	0.7769	8.6536	0.4091	8.7591
		8		7.8934	6.1563	8.4615	5.9418	7.3117	6.4086
		12		16.8355	5.4876	18.2102	5.2882	15.5996	5.6877
		18		30.5508	5.2029	33.3944	4.9925	28.1783	5.3992
		26.5		50.6980	5.0245	54.6579	4.8531	46.8923	5.2063
		40		79.3005	5.0047	83.1990	4.8962	75.4586	5.1184
		48		92.6614	5.0828	96.3537	4.9938	89.0329	5.1748
		75		123.1336	5.4896	125.3321	5.4472	120.9639	5.5325
Pretoria	61 mm/hr	4	38.6°	0.3939	8.5060	0.6509	8.4249	0.3541	8.5232
		8		7.2004	6.3954	7.7052	6.1648	6.6892	6.6732
		12		15.5001	5.6288	16.7346	5.4299	14.3913	5.8294
		18		28.2984	5.3134	30.8635	5.1070	26.1584	5.5065
		26.5		47.1866	5.1179	50.8224	4.9486	43.6930	5.2976
		40		74.2932	5.0802	77.9035	4.9732	70.7361	5.1925
		48		87.0530	5.1512	90.4749	5.0635	83.6904	5.2418
		75		116.2884	5.5450	118.3257	5.5031	114.2777	5.5873
Tshipise	50 mm/hr	4	42.0°	0.2892	8.1758	0.4560	8.1145	0.2654	8.1871
		8		6.1332	7.1756	6.4849	6.8410	5.8419	7.6677
		12		13.1683	6.0126	14.1444	5.8061	12.2962	6.2252
		18		24.2786	5.6065	26.3346	5.4034	22.5650	5.7980
		26.5		40.8491	5.3637	43.8846	5.1957	37.9347	5.5431
		40		65.1933	5.2841	68.2654	5.1782	62.1679	5.3955
		48		76.8522	5.3400	79.7687	5.2536	73.9868	5.4295
		75		103.8973	5.7128	105.6321	5.6713	102.1854	5.7548

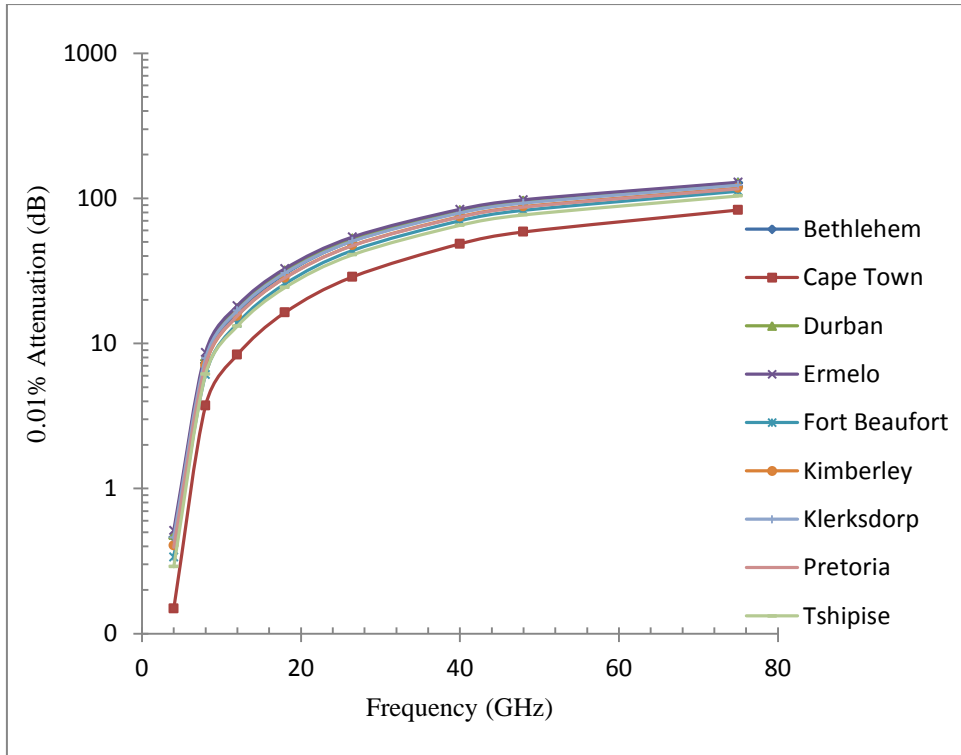


Figure 3.8 (a): Rain Attenuation at 0.01% exceedence for all regions for Circular Polarization

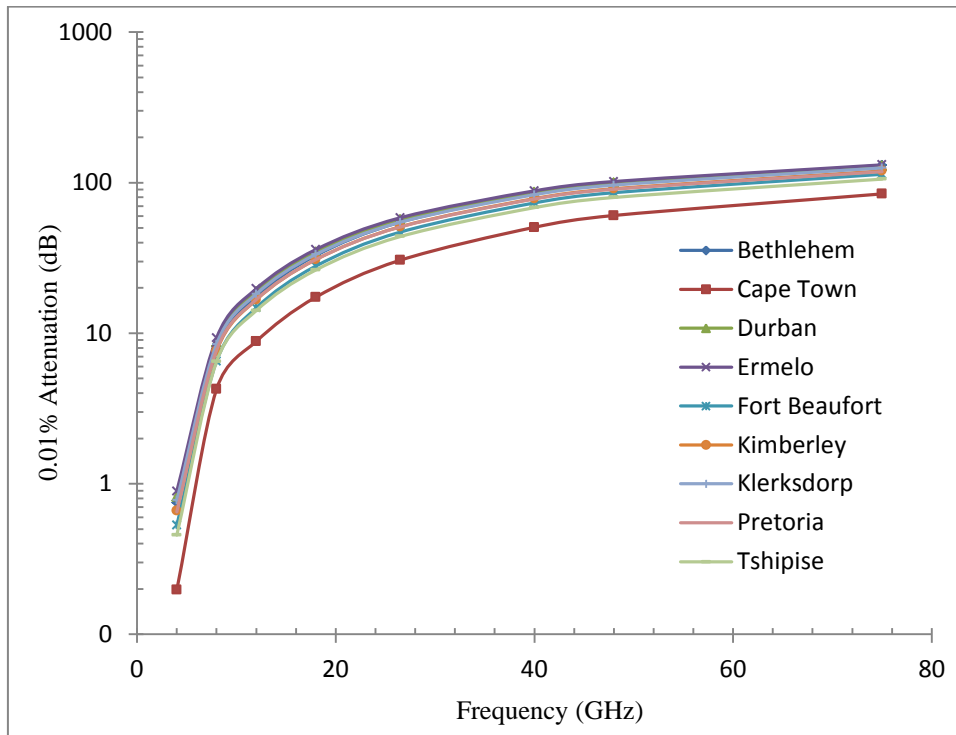


Figure 3.8 (b): Rain Attenuation at 0.01% exceedence for all regions for Horizontal Polarization

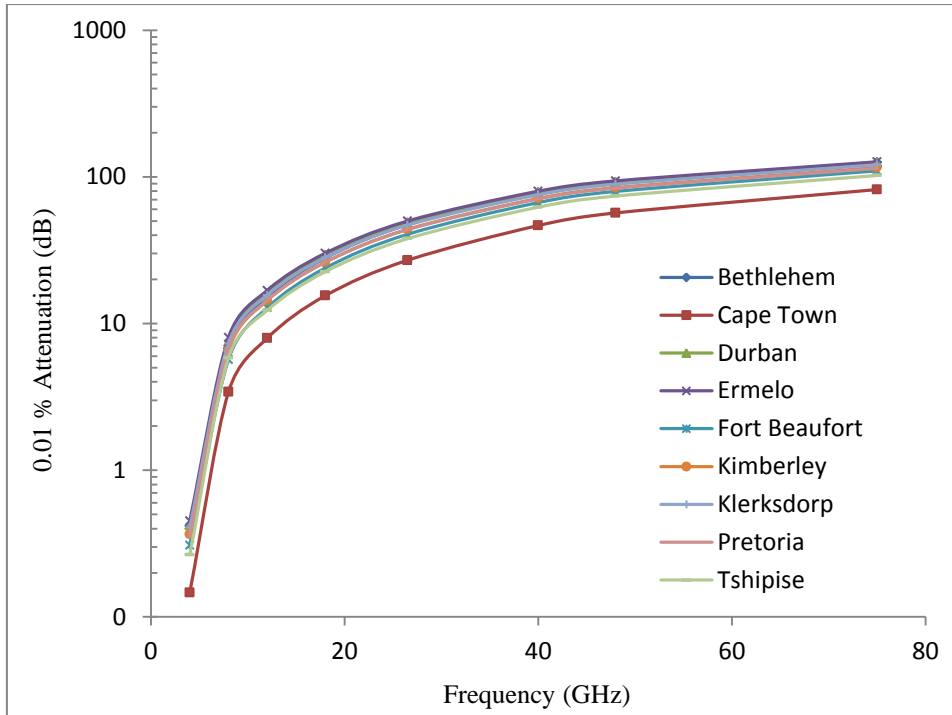


Figure 3.8 (c): Rain Attenuation at 0.01% exceedance for all regions for Vertical Polarization

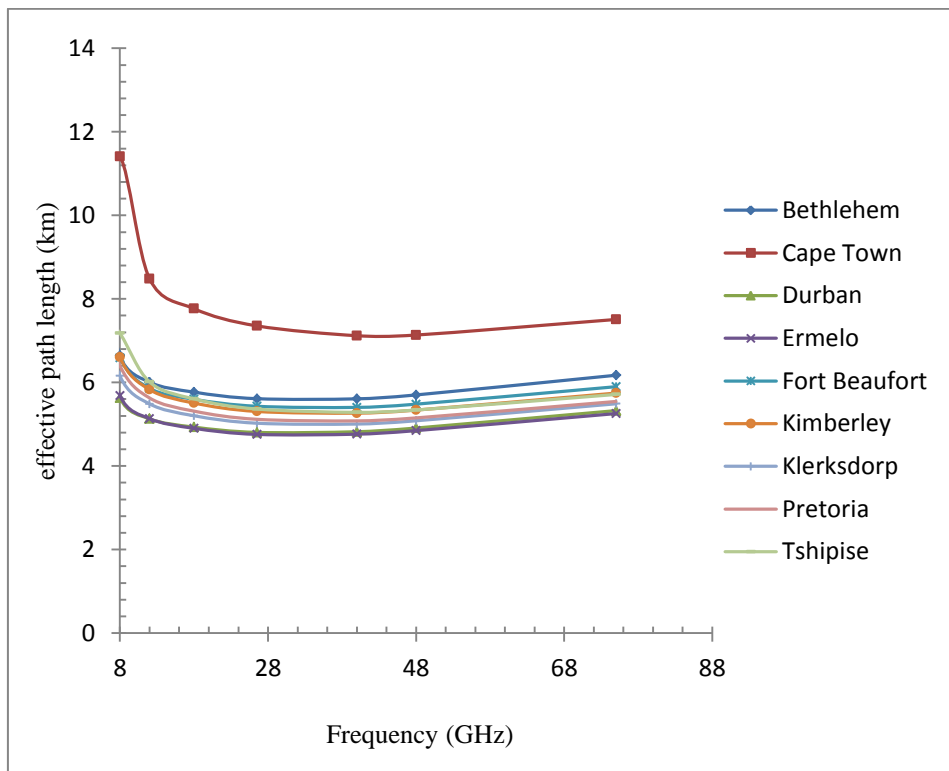


Figure 3.9 (a): Effective path length for all regions for Circular Polarization

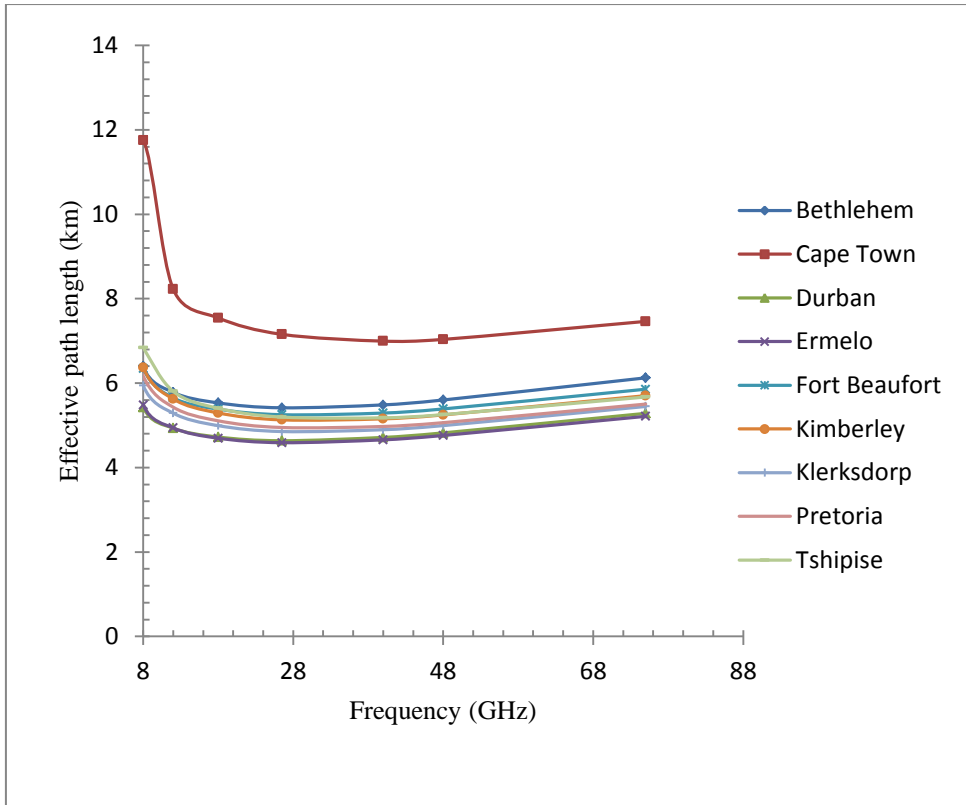


Figure 3.9 (b): Effective path length for all regions for Horizontal Polarization

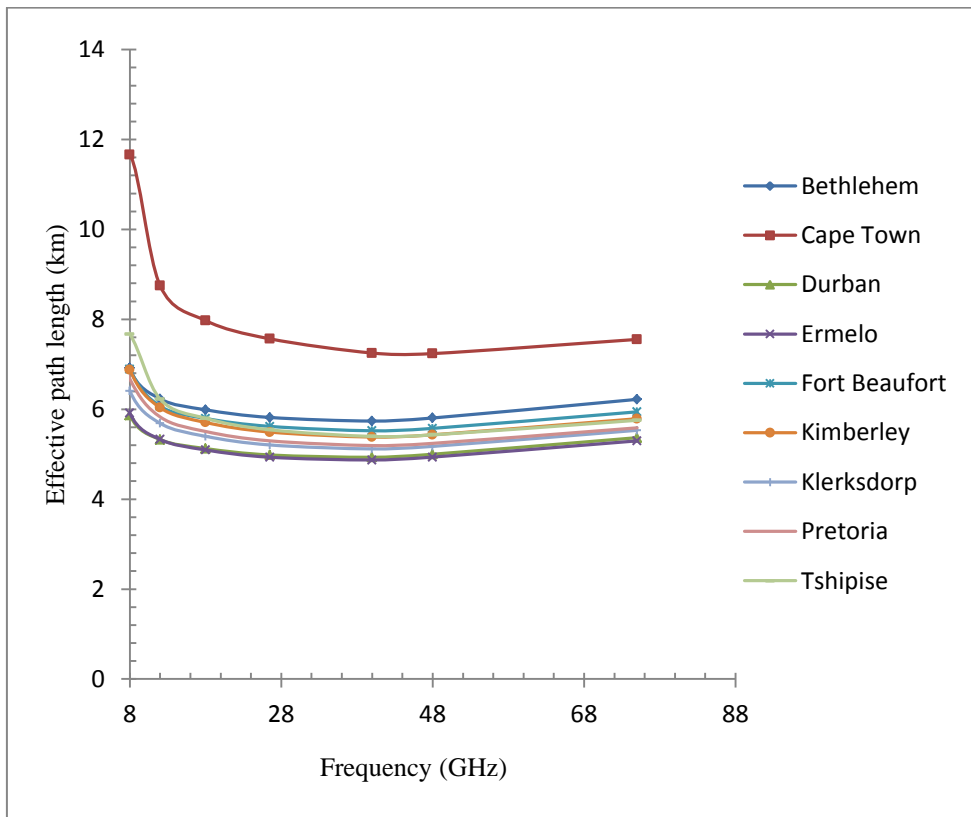


Figure 3.9 (c): Effective path length for all regions for Vertical Polarization

3.2.4 Earth-Space Rain Attenuation

Earlier satellites have been offering services at C-band frequencies but the demand for increased bandwidth has seen this band exhausted and inadequate in supporting the fast data rates associated with modern applications. The inherent advantages at these bands are quite evident from Figure 3.11 which depicts low attenuation levels even at high availability requirements. In this section, maximum fade depths were determined for probabilities ranging from 0.001% to 5%. Evidently, as the availability increases, so does the required rain fade margin. The variability of rainfall attenuation with availability is location as well as frequency dependent. For the two frequencies considered in Figure 3.10 (lower and upper bounds for C-band), as discussed in Subsection 3.2.5, Cape Town has the least attenuation for all the percentage availabilities considered. It also follows that, given the local rain rates, that Ermelo experiences the highest rainfall attenuation within the range of the probabilities considered. The results are consistent with the notion that higher rain rates require high fade margins. This may be true for terrestrial radio links where the elevation angle is considered to be uniform (zero) for all locations. However, the effect of elevation angle on attenuation (Equations (3.6) through (3.11)), is such that locations of higher rain rate may have lower attenuation as compared to those with lower rain rates for 0.01% of the time. This means that areas having the same rain rate do not necessarily have to have equal fade margins. The dependency of rainfall attenuation on geographical location plays an important role in this analysis.

The effect of effective path length on rain attenuation is observed in Figure 3.10 (a). For probabilities of outage above 2% of the time (availability of 98% or less), there is a noticeable overlapping behaviour amongst the graphs. The graph for Tshipise prominently displays this scenario. This is a result of different effective path lengths for different locations. The same scenario is less prominent in Figure 3.10 (b), which is probably nullified by the higher frequency of 8 GHz. It is even clearer at Ku-, Ka-, and V-band frequencies as shown in Figures 3.11, 3.12, and 3.13 respectively.

The Intelsat 17 (IS-17) provides good coverage in South Africa, transmitting at Ku-band frequencies with vertical polarization with a beam peak of up to 53.3 dBW. The uplink frequencies range from 13.75 – 14.50 GHz with the downlink range of 10.95 – 11.70 GHz [IS-17 factsheet]. The increased demand for bandwidth for greater data flow and the over-crowding of the electromagnetic spectrum may see this provision inadequate for the numerous applications of satellite systems. The trend recently has been to utilize Ka-band frequencies for satellite communications, with uplink frequencies of 30 GHz and downlink frequencies of 20.2 GHz [63].

Despite the obvious merits that include less propagation losses (due to hydrometeors), less free space loss and the ability to penetrate foliage, lower frequencies do not provide for restrictions in power

requirements, easy transmit-to-receive isolation, and antenna aperture size. Utilization of Ka-band frequencies and even higher can provide spectral relief for satellite applications with reasonably sized antennas and reduced power requirements. Figures 3.11 and 3.12 show that operating at Ka- and V-bands requires a considerable amount of fade margin as compared to operating at lower bands. The worst case difference, as expected, is between the vertical and horizontal polarizations, with a value of 4.7 dB at 75 GHz for Ermelo. For linear polarization, precision alignment is required for the earth station antenna to maximize reception from the satellite. Given the height of the satellite above the earth, transmission latencies are imminent. Since the satellite is of geostationary type, it has a fixed radius of orbit of about 42 242 km. Its height above the earth surface is therefore given by [57]:

$$h_{GEO} = (42242 - 6378) = 35864 \text{ km} \quad (3.13)$$

Unlike C- and Ku-bands, Ka-band employs multiple spot beams which makes it attractive in terms of focus and frequency reuse. Over a wide geographical area, the same frequency range can be reused many times provided adjacent spot beams use a different frequency.

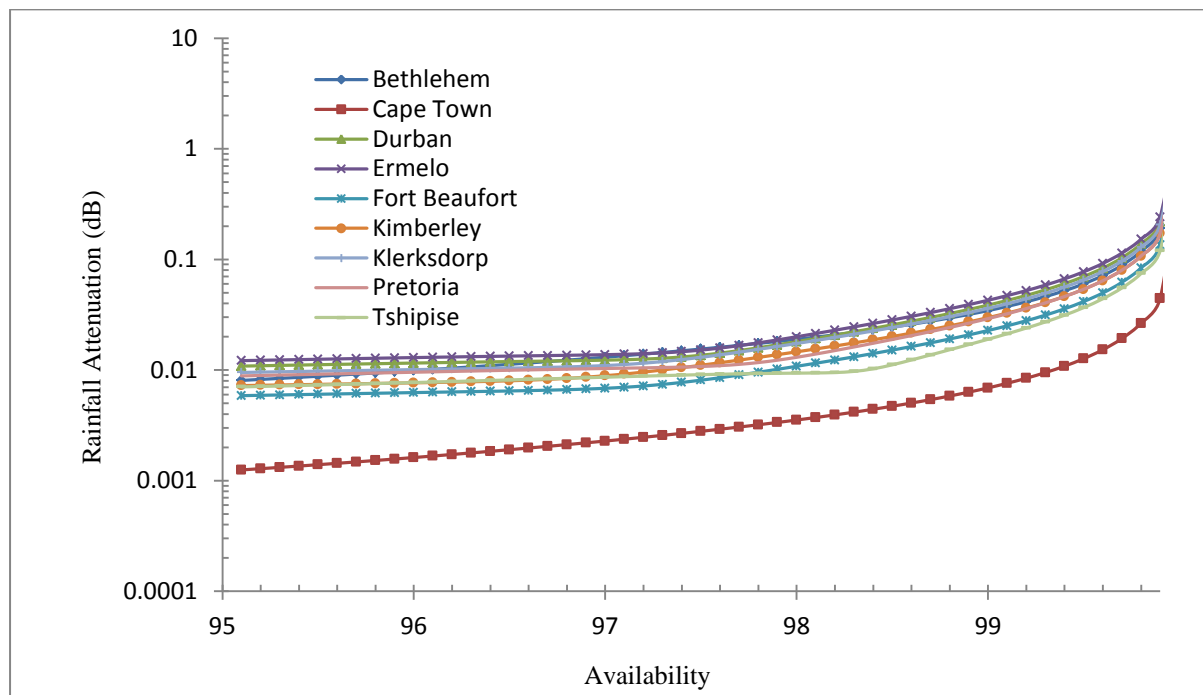


Figure 3.10 (a): Rain Attenuation at C-band for Horizontal Polarization for all locations at 4 GHz

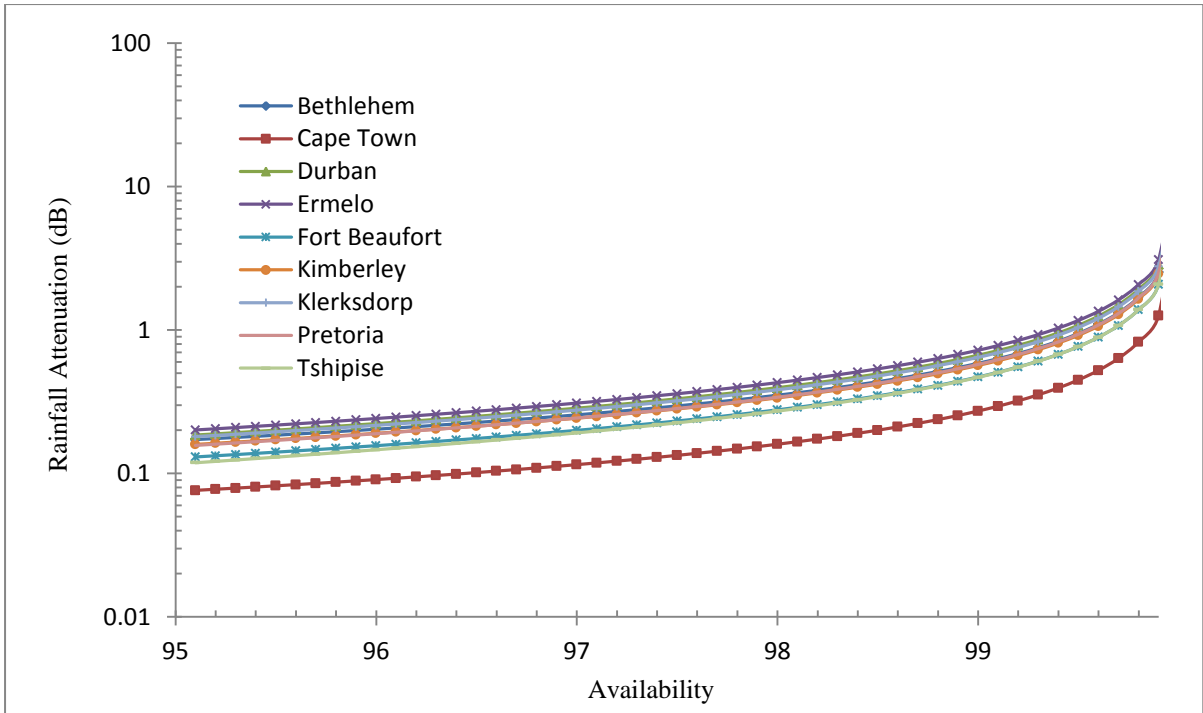


Figure 3.10 (b): Rain Attenuation at C-band for Horizontal Polarization for all locations at 8 GHz

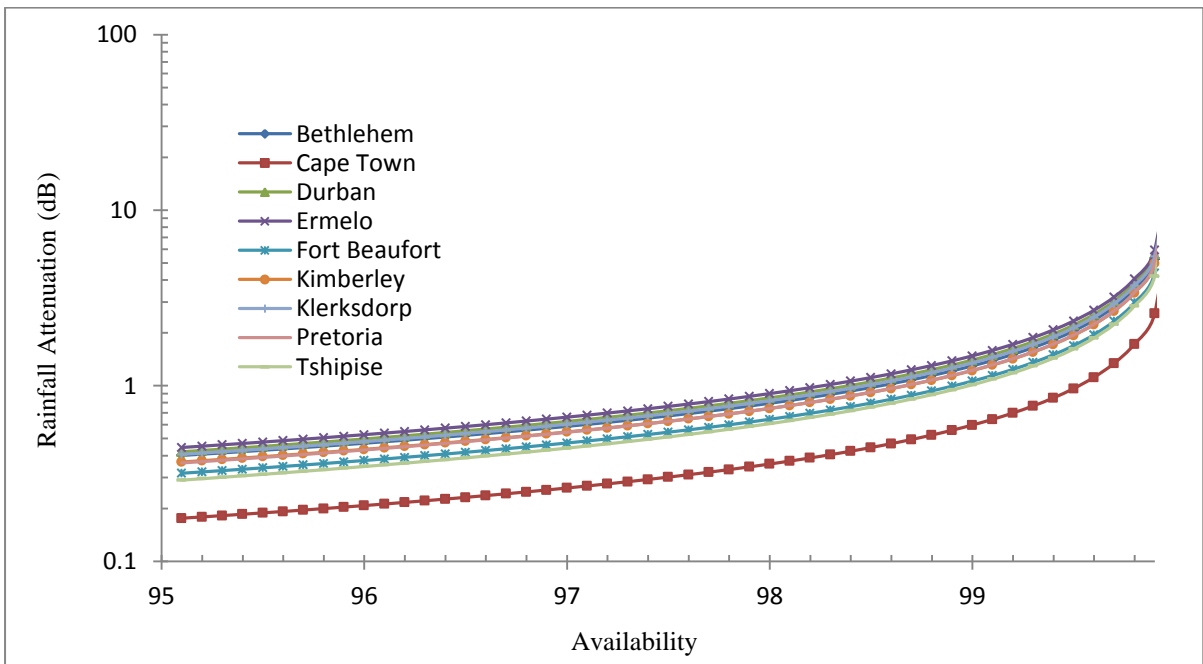


Figure 3.11 (a): Rain Attenuation at Ku-band for Vertical Polarization for all locations at 12 GHz

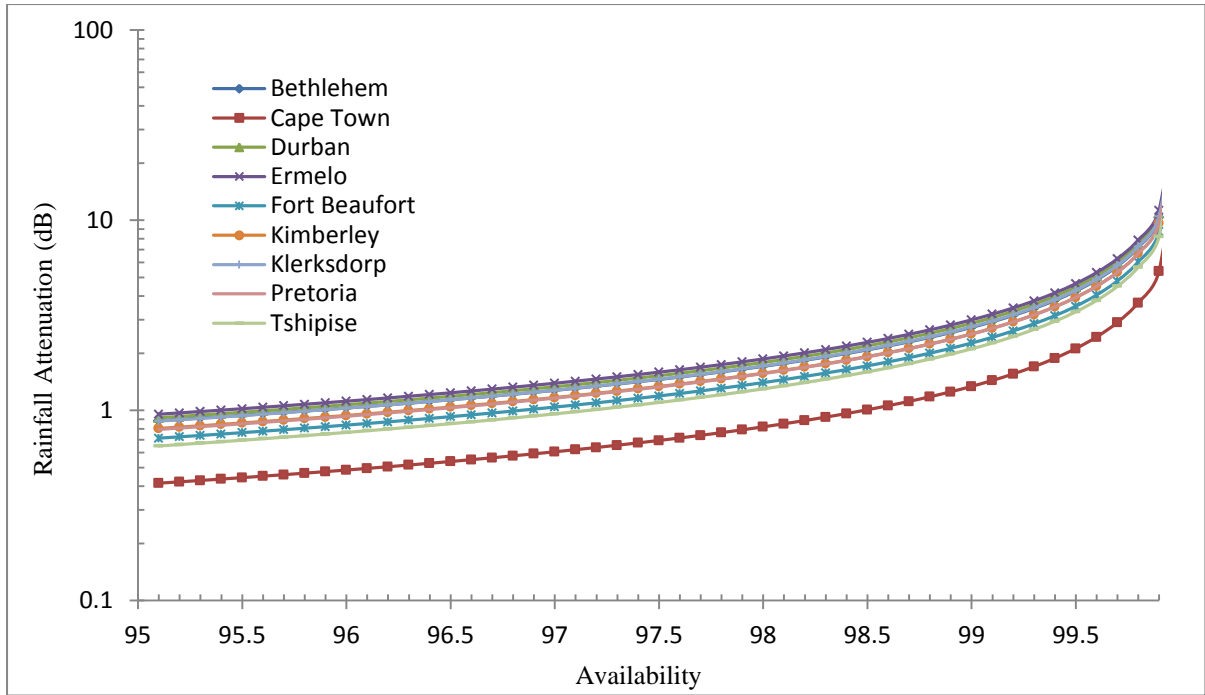


Figure 3.11 (b): Rain Attenuation at Ku-band for Vertical Polarization for all locations at 18 GHz

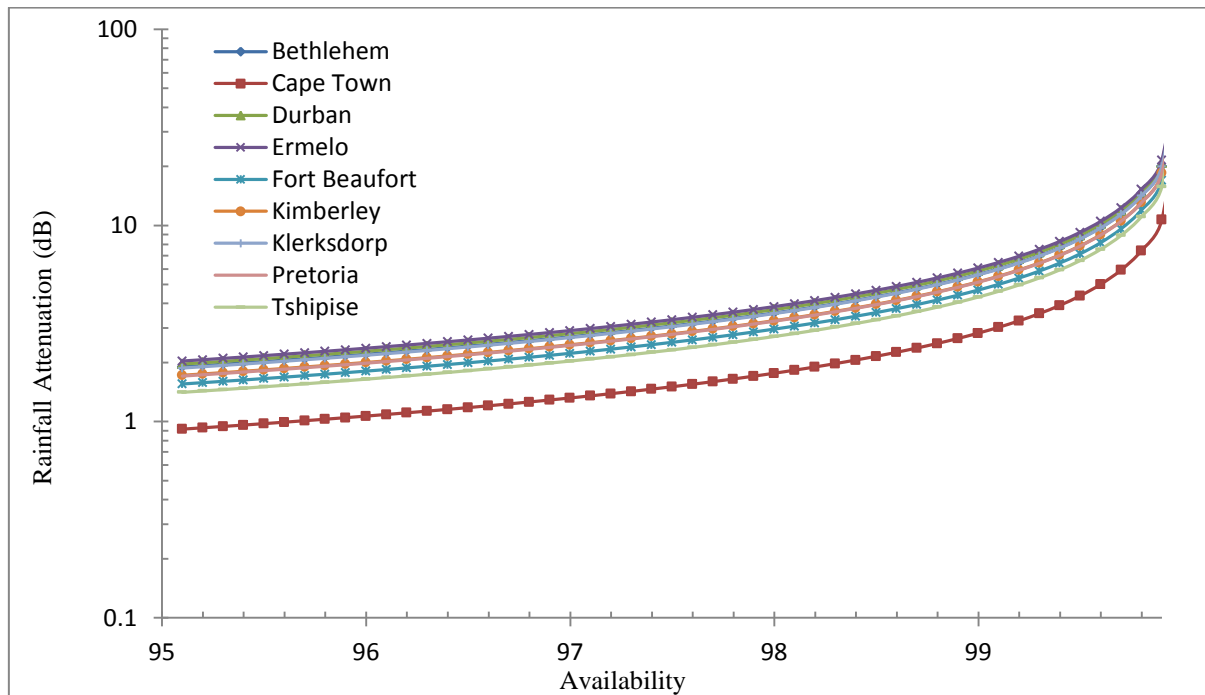


Figure 3.12 (a): Rain Attenuation at Ka-band for Circular Polarization for all provinces at 26.5 GHz

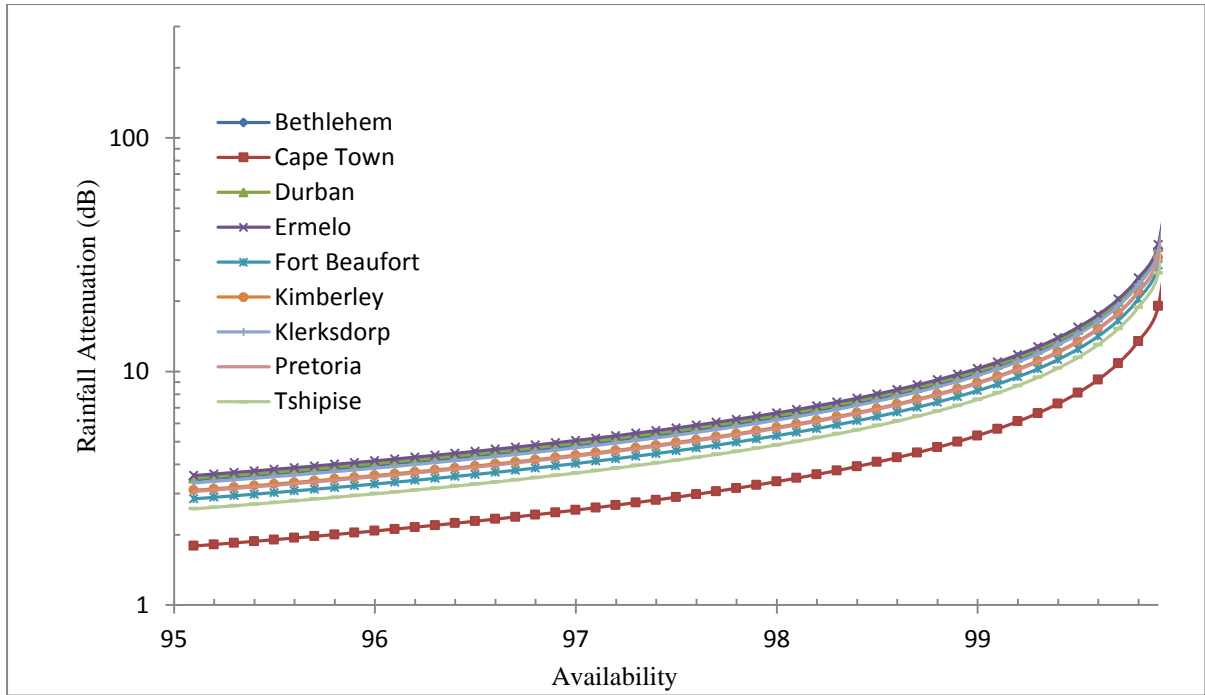


Figure 3.12 (b): Rain Attenuation at Ka-band for Circular Polarization for all provinces at 40 GHz

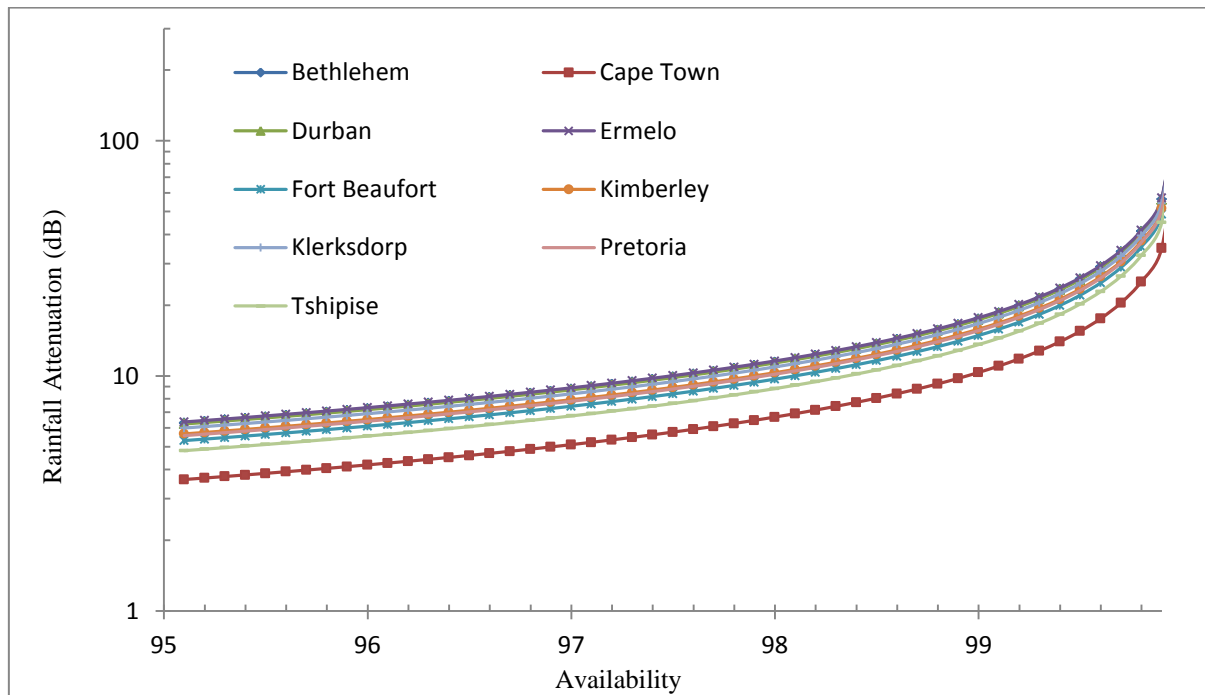


Figure 3.13 (a): Rain Attenuation at V-band at 75 GHz for all provinces for Horizontal Polarization

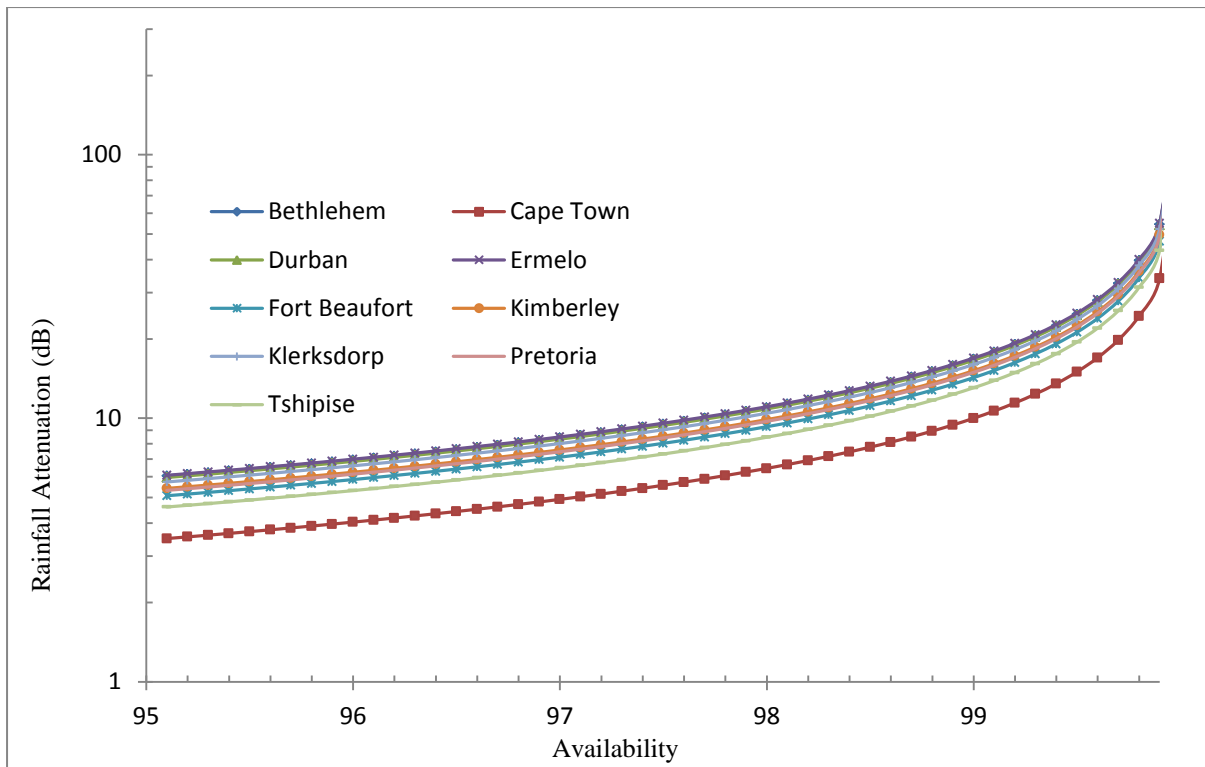


Figure 3.13 (b): Rain Attenuation at V-band at 75 GHz for all provinces for Vertical Polarization

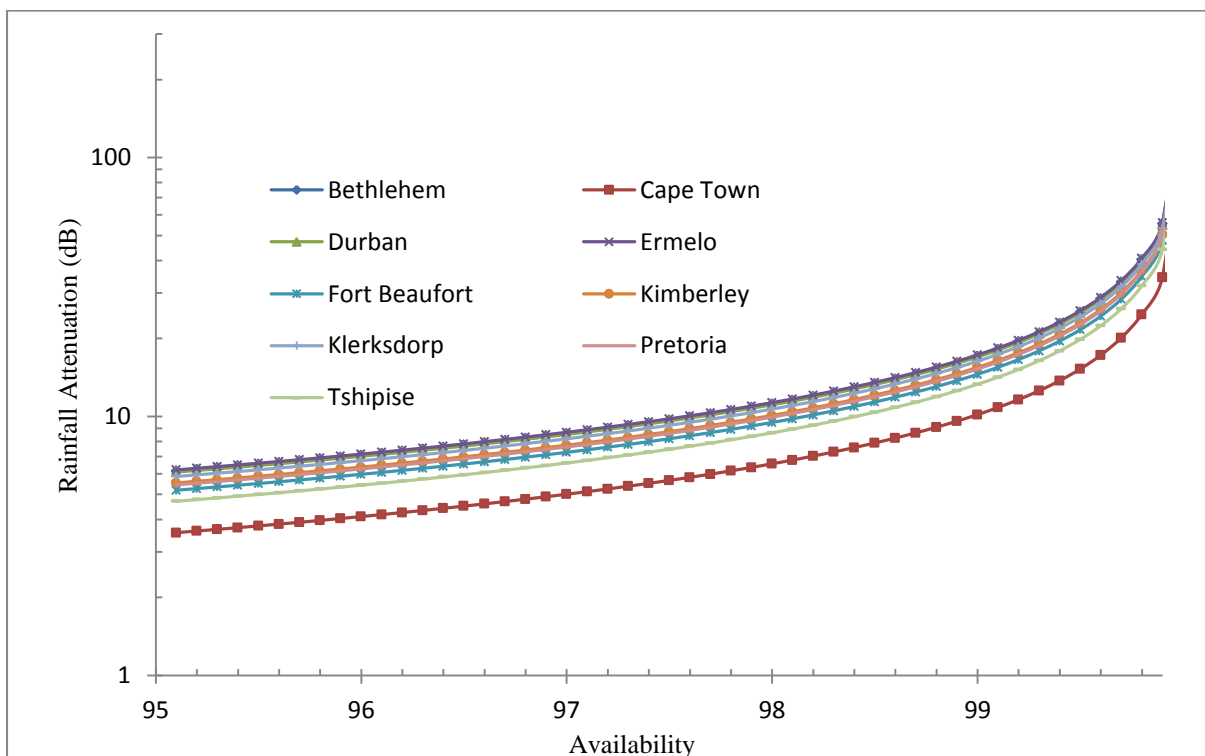


Figure 3.13 (c): Rain Attenuation at V-band at 75 GHz for all provinces for Circular Polarization

3.3 Chapter Summary and Conclusion

Section 3.1 presents rain attenuation estimation using both the ITU-R model and measured regional rain rate data collected over 10 years. In addition, the results of 1-year rain attenuation measurements are used to design a link budget for the University of KwaZulu-Natal microwave links. Also, the hop distance chart is used to estimate the maximum hop distance a defined link can have under a pre-defined rain fade margin and system gain. The results will be useful in the proper planning of radio links by radio network planners in South Africa. They will improve precision in the estimation of link availability, link performance, link budget and management of the link frequency between the ranges from 1 GHz to 400 GHz.

Section 3.2 presents results that are based on the Intelsat 17 (IS-17) satellite characteristics which operate at C- and Ku-band and projections are made into higher frequency bands. Across all the frequency bands from C-band up to V-band, rainfall attenuation, elevation angle, and effective path length have been determined for satellite link applications in South Africa. Consideration has been given to link availabilities from 95% up to 99.999% of the time. It is noted that the severity of the degradation of the propagating signal increases with increasing availability. However, for a given percentage availability, the signal degradation increases with an increase in operating frequency of the satellite link. It is observed for example in Figure 3.6 (a) and more clearly from Table 3.4, that a fade margin in excess of 50.7 dB is required for 99.99% availability in Klerksdorp considering circular polarization at 26.5 GHz. For the same location, availability, and polarization, a fade margin of 79.3 dB is required for the operating frequency of 40 GHz.

Results displayed in Table 3.4 show that areas of lower elevation angles have longer effective path lengths. These areas are expected to suffer higher loss in dB during operation since signals traverse a longer atmosphere and the overall slant path is increased. For any of the locations studied, the effective path length varies inversely proportional to the frequency of operation up to 40 GHz. Beyond this frequency a direct proportionality relationship is observed consistently up to 75 GHz. It can thus be inferred that this relationship is valid for even higher frequencies not under consideration in this thesis.

Considering all the locations under study for South Africa, Cape Town is associated with the lowest fade margin at all frequencies and availabilities. Conversely, Ermelo had the highest fade margin at all frequencies and availabilities. A number of other locations also experience almost the same level of degradation as Ermelo. The two notable ones are Bethlehem and Durban. In comparison with Ermelo, at 75 GHz, Bethlehem is lower by 1.25 dB, while Durban is 2.04 dB lower for horizontal polarization. For circular polarization Bethlehem and Durban are lower by 1.09 dB and 1.97 dB, respectively,

while for vertical polarization they are lower by 0.93 dB and 1.92 dB, respectively. It should be noted that all these comparisons are made for 99.99% availability. Despite having the smallest elevation angle of 26.4 degrees, Cape Town maintains a low fade margin requirement and this can only be attributed to its significantly low local rain rate of 25 mm/h. Tshipise has the highest elevation angle of 42 degrees and local rain rate of 50 mm/h (twice that of Cape Town). It remains in need of higher fade margins as compared to Cape Town though less prone to degradation as compared to the other locations in the country.

At the lower bound of the Ka-band, 26.5 GHz, it is observed that the lowest rain attenuation of about 27 dB (for Cape Town) is obtained with the highest value of 50 dB obtained for Ermelo for 0.01% of the time. For the same demand at 40 GHz, the minimum and maximum fade margins required are 46.6 dB and 79.9 dB respectively. So 27 dB and 80 dB can be considered the minimum and the maximum attenuation levels at Ka-bands for 99.99% availability for satellite communications links in South Africa.

Chapter 4

Raindrop Size Modelling Using Method of Moments and Its Applications for South Africa Radio Systems

4.0 Introduction

In this chapter, raindrop size distribution (DSD) modelling and analysis are presented. Rainfall is classified into four main categories, namely: drizzle, widespread, shower and thunderstorm, depending on the rain rate. The Gamma and Lognormal distribution models are employed using the method of moments estimator and considering the third, fourth and sixth order moments. The models obtained are compared with the existing raindrop size distribution models. This is then followed by the implementation of the proposed raindrop size distribution models on the computation of the specific rain attenuation. Finally, suitable raindrop size distribution models are proposed for the South African region. The proposed models are very useful for the determination of rain attenuation for terrestrial and satellite systems.

4.1 Raindrop Size Distribution Modelling

The quest for a huge bandwidth for higher data rates coupled with the congestion of lower frequencies has forced communication systems designers to explore the higher frequency bands. The higher frequencies such as microwave and millimeter waves are available and allow multi-Gbit/second signal transmission in terrestrial, satellite and wireless communications. The other advantages that are associated with the frequencies in this range are the immunity to interference, short range capacity coverage, frequency reuse, large bandwidth and easy deployment. At these higher frequencies, attenuation due to environmental factors such as atmospheric gases, oxygen absorption, foliage blockage, scattering effect (diffused and specular reflection), fog, clouds and precipitation [1, 64-67] is more pronounced. The chief contributor to impairment at these frequencies is the raindrop, which has roughly the same size as the radio wavelength at higher frequency, and thus causes scattering of the radio signal [65].

The microwave and millimeter wave attenuation depends considerably on rain rate and raindrop size distribution [65]. In view of the complexity of communication systems required to meet the demands of today's users, adequate knowledge of the rain characteristics of these bands is required in order to appropriately compensate for the associated signal loss [1, 64 – 67].

In the field of climatology, meteorology, hydrology and radio communications, the spatial and temporal studies of rainfall characteristics such as rain rate and raindrop size distribution are important [68]. The reason lies in the unpredictability and stochastic behaviour of climatic parameters.

Several researchers have solved this problem by employing empirical, analytical and statistical approaches [19, 69, 70]. The measurement of raindrop size distribution is very much a statistical process which depends on the data collected [69]. There are several measurement methods that have been used in the past for sampling the raindrop size distribution such as the filter paper method, the Doppler radar method, the Opto-electronic method and the electromechanical method. The latter is considered in this paper by using the Joss-Waldvogel RD-80 distrometer [19, 69]. The limitation of such equipment is in the spatial and temporal variation of raindrop size distribution. This limitation can be overcome through the use of radar equipment or employing advanced mathematical techniques to extrapolate point measurements by a Distrometer [1]. It should be noted that the most common reference available for calculating rain attenuation often uses rain intensity R , probably because of a scarcity of rain drop size data. The relationship between rain rate and drop size distribution $N(D)$ is given as [70]:

$$R = 6\pi \times 10^{-4} \int_0^{\infty} D^3 v(D) N(D) dD \quad (4.1)$$

where $v(D)$ represents the terminal velocity of raindrops in still air and is measured in meters per second, and D is the equivalent spherical diameter in millimetres.

To account for the total attenuation at higher frequency in a system, the first step is to calculate the specific rain attenuation which depends on rain rate and the raindrop size. Extensive work in the South African context has been done by Owolawi [19] on raindrop size distributions which are simply expressed by using statistical distribution expressions such as the Power law, exponential distribution, gamma and lognormal distribution. It is widely known that three popular distribution functions are used to describe raindrop size spectra. The models of Laws and Parsons [3] and Marshall and Palmer [71] are based on exponential distribution, and are generally used in temperate regions. The other two models, the Lognormal and modified Gamma models are appropriate for tropical and sub-tropical regions [72 – 76]. Researchers from Brazil [8, 9, 74], India [77], Malaysia [10, 11, 78], and Nigeria [15, 79], all from the tropical regions, have employed the latter two distribution functions to model the raindrop size for all kinds of rainfall characteristics in their respective regions. It has been established that the exponential method may not be suitable for tropical and sub-tropical regions, in which South Africa falls [15, 69,]. The traditional modeling method with experimental DSD data is achieved by fitting the raw data which may result in large discrepancies between the modeled and the measured DSD data. The method of moments is often used to represent an estimated DSD input parameter.

The aim of the present work is to employ the method of moments to obtain the DSD parameters and apply the appropriate statistical distributions such as the Lognormal and modified Gamma functions. The results are tested against the existing models and true DSD population spectra. The model

parameters are further employed to determine the specific attenuation coefficients from 5 to 100 GHz using the proposed Lognormal models, and the extinction cross-sections that are based on Mie scattering for different rain rate regimes.

4.2 Experimental Setup and Data Sorting

In this work, the raindrop size distribution data is measured by the J-W RD-80 Distrometer. The equipment is capable of measuring raindrop diameters between 0.3 mm and 5 mm with an accuracy of $\pm 5\%$. The JWD is an impact distrometer that has two main components: a sensor and a processor, as shown in Fig. 4.1. The sensor is an electro-mechanical unit that measures the vertical momentum of raindrops as they impact on it, and then transforms this momentum into a pulsed signal that is processed by the processor by relating the amplitude of the pulses from the sensor to the raindrop sizes. The sensor further sorts the drop diameters into 127 channels, each representing the number of drops in a size interval, and this data is further compressed into 20 classes. 4 classes are then averaged every minute and stored. The resultant DSDs are then available in the output form of a table, graph, or plot using DISDRODATA software.

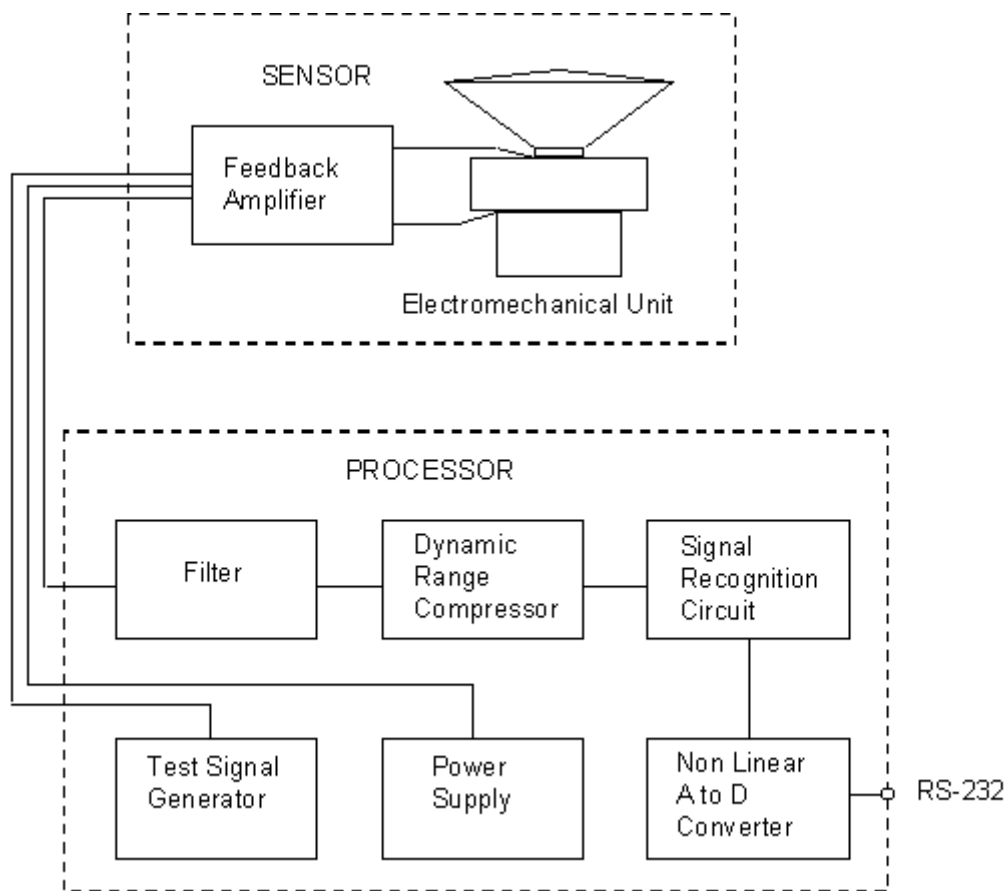


Figure 4.1: Block diagram of the JWD-RD 80 Distrometer [115]

The equipment is positioned on the roof top of the School of Electrical, Electronics and Computer Engineering, Durban, South Africa. The geographical coordinates of where the equipment is positioned are latitude $29^{\circ} 52'S$ and longitude $30^{\circ} 58'E$, with an altitude of 139.7 meters above sea level. At this height, the windy conditions are taken into consideration. It is noted from many literature sources that windy condition serves as the largest single factor degrading measurement accuracy. It is often observed that small drops may pass the observing sensor area at low angles without falling in the sampling area. This problem has led to false terminal velocity [80 – 84]. In order to minimize this problem, the Distrometer is placed within two rectangular wall enclosures as presented in Figure 4.2. Since the sampling area of a Distrometer is 50 cm^2 , the inner rectangular wall ($2\text{m} \times 2\text{m} \times 0.8\text{m}$) is to prevent birds from damaging the cone part of the Distrometer and the outer rectangular wall ($3\text{m} \times 4.14\text{ m} \times 11.6\text{m}$) is to prevent the wind from drifting the rain drops away from reaching the sampling sensor area.

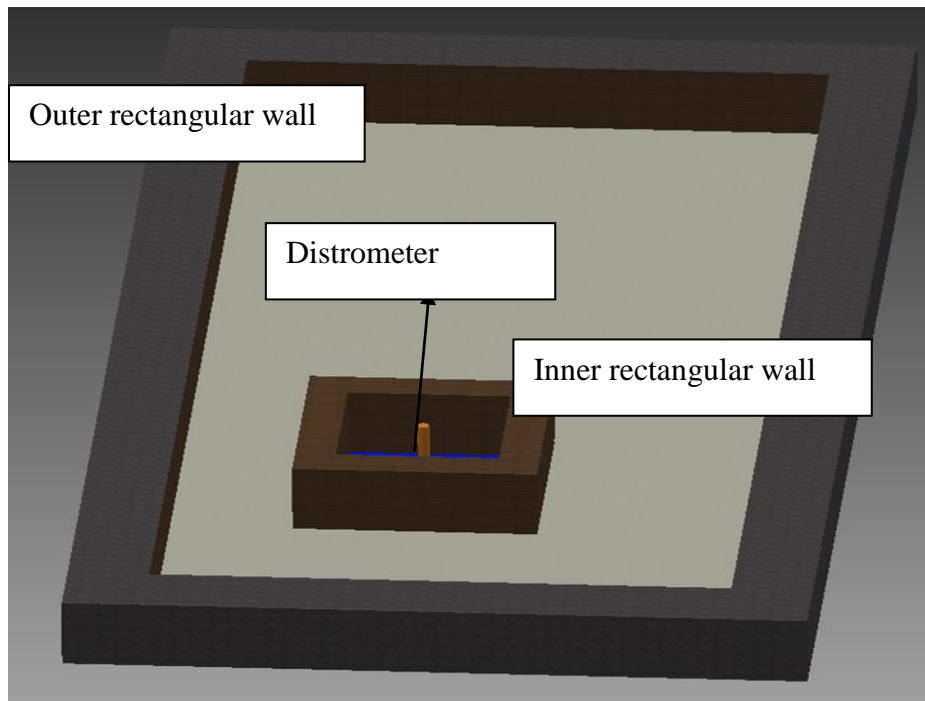


Figure 4.2: Distrometer enclosure on Durban Site

The data were collected over a period of two years and grouped into four rain regimes based on the rain rate and the general regime where all the raindrop size data is combined. The details of data sorting are described in reference [73]. Reference [73] and this work used the same database but the focus of [73] was on the employment of the maximum likelihood estimator approach with lognormal distribution to model the dropsize distribution for Durban while the focus of this work has been on the classification of drop sizes into different rain types, namely: drizzle, widespread, shower and thunderstorm, and the employment of the gamma and Lognormal distribution models using the

method of moments estimator, considering the third, fourth and sixth order moments. Several authors have employed rain rate for the classification of raindrop size distribution into their respective rain types such as drizzle, widespread, shower and thunderstorm [2, 79, 85 – 89]. As presented by Afullo [2], raindrop size is classified into the four classes based on the characteristic of unimodal and bimodal effects on the probability density of the drop size distribution in South Africa. Based on this reason, the same classes of rain rate classes are employed in this paper to categorize the raindrop size distribution into the following types:

- Drizzle ($0.1 \text{ mm/hr} < R < 5 \text{ mm/hr}$)
- Widespread ($5 \text{ mm/hr} \leq R < 10 \text{ mm/hr}$)
- Shower ($10 \text{ mm/hr} \leq R < 40 \text{ mm/hr}$)
- Thunderstorm ($R \geq 40 \text{ mm/hr}$)

It should be noted that the rain rate sampling rate is at 1-minute integration time as recommended by the ITU-R. The drop density decreases from drizzle to thunderstorm regime progressively, i.e. drizzle records over 46 000 samples while the thunderstorm sample number is less than 34.

4.3 DSD Models with the Method of Moments (MoM)

In this section, two main statistical distributions are considered using the method of moments to describe the probability density distribution of the raindrop size data as classified in section one of the paper. The two distributions are the Lognormal and modified Gamma functions. The general expression to describe the rain rate, R , (in mm/hr) from the distrometer is given in [75]:

$$R = \sum_{i=1}^{20} \frac{3600\pi}{6ST} D_i^3 n_i \quad (4.2)$$

where S is the area of the sensitive surface of the distrometer in m^2 ($S = 0.005 \text{ m}^2$), T is the time interval for the measurements in seconds (the standard value of the $T = 60\text{s}$ was used) and n_i is the i^{th} channel with diameter D_i in mm. Note that the distrometer measured raindrop size distribution $N(D_i)$ ($\text{m}^{-3}\text{mm}^{-1}$) based on the semi-empirical expression is:

$$N(D_i) = \frac{n_i \times 10^6}{v(D_i) \times S \times T \times \Delta D_i} \quad (4.3)$$

where n_i is the number of drops measured in drop size class i during the time interval T , ΔD_i is the diameter interval of drop size class i , and $v(D_i)$ is the terminal velocity of rain drop in m/s based on the Gunn and Kinzer expression [90]. The equivalent general model using any form of distribution function is summarized as in [73]:

$$N(D) = N_T \times pdf(D) \quad (4.4)$$

where N_T is the raindrop concentration per unit volume of rainfall drops for the different rain regimes and $pdf(D)$ is the probability density function of the raindrop distribution. In this chapter, we limit the discussion to the two distributions mentioned earlier to describe the $pdf(D)$. The advantages inherent in the application of MoM includes the simplicity of analytical application on the DSD parameters, and physical interpretation of the chosen function parameters of the DSD.

The statistical moment at n^{th} order moment is theoretically expressed as [91]:

$$M_n = \int_{D_{min}}^{D_{max}} D_i^n N(D_i) dD = \sum_{i=1}^{20} D_i^n N(D_i) dD_i \quad (4.5)$$

where D_{min} and D_{max} are 5 mm and 0.3 mm for the J-W RD-80 . To compute raindrop size distribution parameters from the distrometer, Equation (4.5) is employed and re-expressed as [92]:

$$M_n = \sum_{i=1}^{20} D_i^n \left[\frac{ni}{S \times T \times v(D_i)} \right] \quad [m^{-3} mm^n] \quad (4.6)$$

Equation (4.6) is applied to the distrometer measured data and the collected data are then equated to the statistical equivalent at the chosen order of the moment.

4.4 Gamma Distribution Model and MoM

In this study, J-W RD-80 distrometer data was fitted using a modified gamma distribution by employing an estimator method of moments. The modified Gamma distribution technique is considered because of its ability to represent DSD parameters at low and high diameter of drops. The general expression for the Gamma distribution model for raindrop size distribution is given as [2, 75, 93]:

$$N(D_i) = f(D_i)N_T = N_0 D_i^\mu \exp(-\Lambda D_i) \quad (m^3/mm) \quad (4.7a)$$

where:

$$f(D) = C D^{\alpha-1} \exp\left[-\frac{D}{\beta}\right]$$

$$N_0 = N_T C = N_T \frac{\Lambda^{\mu+1}}{\Gamma(\mu+1)} ; \mu = \alpha - 1 ; \Lambda = \frac{1}{\beta} \quad (4.7b)$$

where the DSD parameters $N_0 (mm^{-1} m^{-3})$, μ , and $\Lambda (mm^{-1})$ are the intercept, shape and slope parameters respectively. Note that α is the shape parameter, β is the scale parameter, and C is a

constant that depends on α and β as shown in Equation (4.7b) above. By equating M_n in Equation (4.6) to Equation (4.7a), the resulting solution for the constants of the modified gamma distribution considering the moment order $n = 3, 4,$ and $6,$ as presented in [76], is:

$$\mu = \frac{11F-8+\sqrt{F(F+8)}}{2(1-F)} \quad (4.8)$$

where:

$$F = \frac{M_4^3}{M_3^2 M_6} \quad (4.9a)$$

$$\Lambda = (\mu + 4) \frac{M_3}{M_4} \quad (4.9b)$$

$$N_0 = \Lambda^{\mu+4} / \Gamma(\mu + 4) \quad (4.10)$$

In this chapter, the statistical relationship between rain rate and DSD parameters are employed in order to explain the characteristics of raindrop size distributions as demonstrated by many authors in the past. Popular among them are, Marshall-Palmer [71], Ulbrich [93], Timothy et al. [94], Ajayi et al.[79], Fišer et al [85] and Afullo [2]. These constants are computed with the available raindrop size distribution data, and the scatter plots obtained are shown in Figure 4.3. For simplicity, the results are fitted with their respective suitable relationships as presented in Table 4.1. The same approach is applied to all the rain regimes and only the shower category is presented as a sample. It is observed that the results produced weak correlation coefficients (R^2), hence the second distribution (Lognormal distribution) is considered and used in this chapter due to the improvement in the value of the correlation coefficients. Based on the rain regimes discussed in Section 4.2 of this chapter, the scatter plots for the shower rain type are presented in Figure 4.3. The summary of the fitted raindrop distribution parameters for gamma are presented in Table 4.1.

The presence of different forms of relationships between rain rate and DSD parameter as presented in Table 4.1 may be due to secondary peaks/bimodal and shifts that are present in the DSD spectral as confirmed by several authors [2, 95]. The types of relationships chosen are often used based on the best correlation coefficients by authors who had worked on the microphysics of DSD [75 – 87]. Based on the reasons stated earlier, the choice of different relationships between rain rate and DSD parameters is considered in fitting the DSD parameters. It consists of a mix of power, logarithm, polynomial (2nd order) and linear relationships.

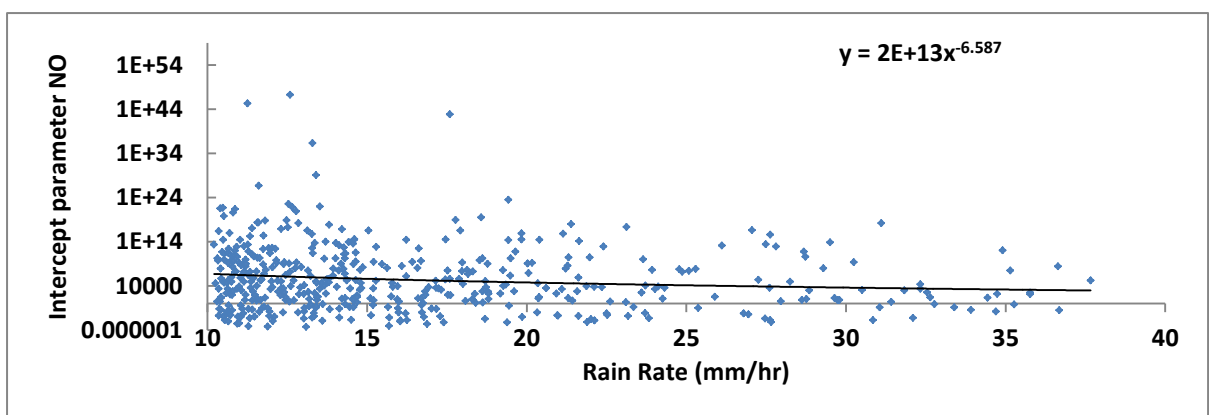
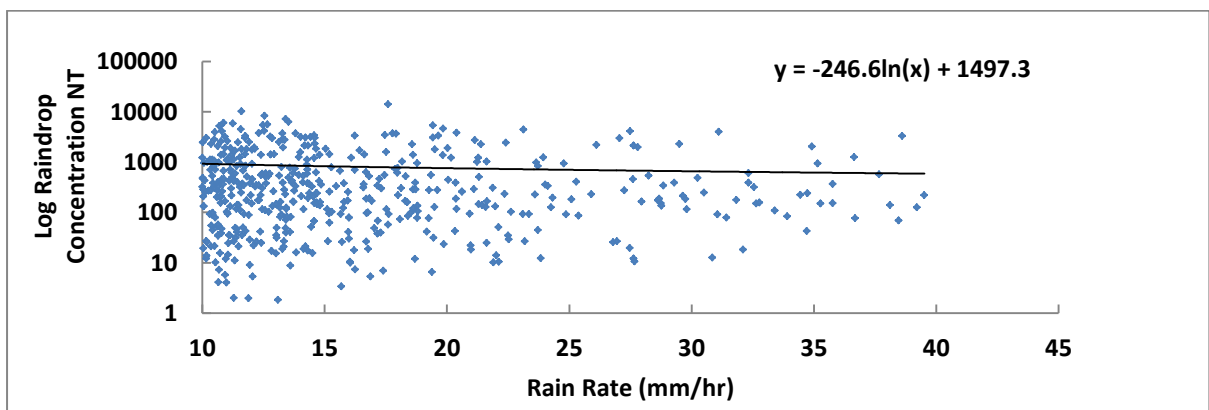
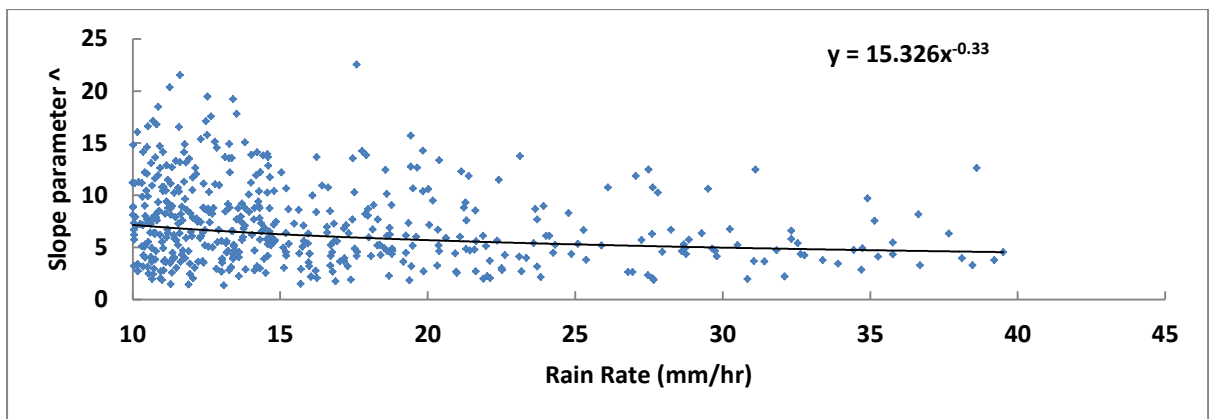
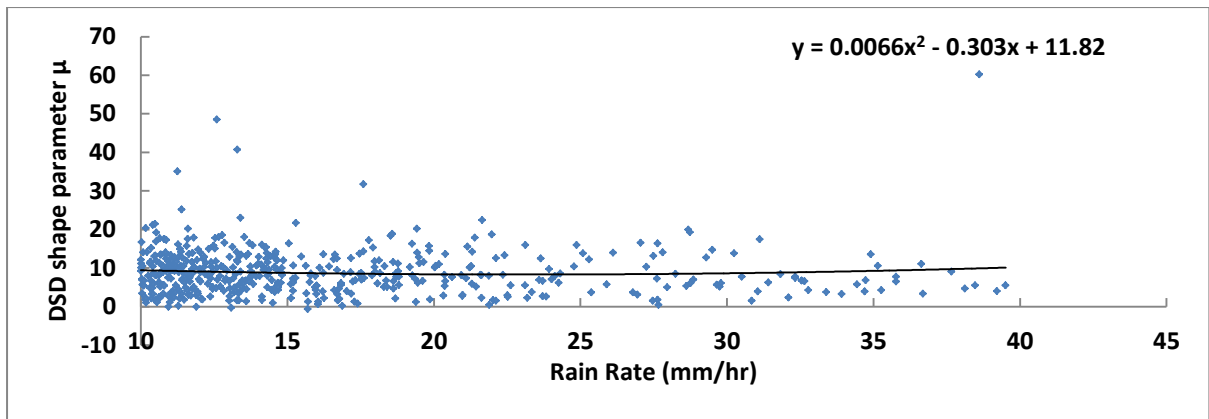


Figure 4.3: Scatter plots for shower: Gamma parameters against rain rate

Table 4.1: Summary of gamma Parameter Model for Raindrop Size Distribution in Durban

Rain regime	Raindrop Count	Raindrop Concentration N_T	Intercept N_0	Slope parameter, Λ	DSD slope Parameter μ
Thunderstorm	$531.39R^{0.0912}$	$639.31\text{Ln}(R) - 1679$	$10^{6\gamma}R^{0.2727}$	$13.697R^{-0.316}$	$0.0028R^2 + 0.390R - 5.7139$
Shower	$403.89R^{0.1}$	$-246.6\text{Ln}(R) + 1497.3$	$2 \times 10^{+13}R^{-6.587}$	$15.326R^{-0.33}$	$0.0066R^2 + 0.303R + 11.82$
Widespread	$284.31R^{0.3317}$	$2 \times 10^{44}R - 2 \times 10^{44}$	$6 \times 10^{58} (\text{Ln}(R) - 1)$	$8 \times 10^{+12} \text{Ln}(R) - 2 \times 10^{13}$	$9 \times 10^{+12} \text{Ln}(R) - 2 \times 10^{13}$
Drizzle	$250.93R^{0.424}$	$10^{45}R - 3 \times 10^{44}$	$-6 \times 10^{29} \text{Ln}(R) + 2 \times 10^{296}$	$9 \times 10^{+13} \text{Ln}(R) - 2 \times 10^{14}$	$-2 \times 10^{15}R^2 + 8 \times 10^{14}R - 6 \times 10^{13}$
General	$270.36R^{0.407}$	$-2 \times 10^{44} (\text{Ln}(R) + 1)$	$7 \times 10^{270}R^2 - 5 \times 10^{272}R + 3 \times 10^{273}$	$-3 \times 10^{12} (\text{Ln}(R) + 1)$	$2 \times 10^{10}R^2 - 10^{12}R - 10^{12}$

It is noted that the raindrop counts are well represented by the power law while other parameters are fitted with different relationship types attaining the best correlation coefficients. The correlation coefficient in the gamma distribution is weak; this may be due to the clusters of the data used. It is observed in Figure 4.3 that the spread of variability of DSD parameters decreases as the rain rate progressively increases. The reduction in variability of DSD parameters observed may be as a result of reduction in the DSD parameter range.

It should be noted that the relationship between R and different DSD parameters are fitted using the least-squares criterion, after the method of moments has been used to deduce the values of the DSD parameters from the raindrop size spectra, which take into account the third, fourth and sixth order moments.

4.5 Lognormal Distribution Model and MoM

The probability density function of the three-parameter lognormal distribution is considered here with a little modification of the distribution input variables. The three-parameter lognormal distribution is expressed as [96] :

$$N(D) = N_T \times pdf(D; \gamma, \mu, \sigma) \quad (4.11)$$

where the random variable mean droplet diameter, D is said to have a three-parameter lognormal distribution if the random variable $Y = \ln(D - \gamma)$, where D is greater than γ , is normally distributed (μ, σ^2), and σ is considered to be greater than zero. The probability density function of the three-parameter lognormal distribution is then given by Pan *et al.* [97] as:

$$pdf(D; \gamma, \mu, \sigma) = \frac{1}{\sigma\sqrt{2\pi(D-\gamma)}} \exp\left\{-\frac{1}{2\sigma^2} [\ln(D - \gamma) - \mu]^2\right\} \quad (4.12)$$

$$\gamma < D < \infty; \quad \sigma > 0$$

Equation (4.11) will be zero if the conditions in Equation (4.12) are not met. Parameter σ^2 is the variance of Y ; it defines the shape parameter of D , where μ is the mean of Y . The method of moments is considered with a condition that $= 0$, with an expression such that [96]:

$$M_n = N_T \exp \left[n\mu + \frac{1}{2} (n\sigma)^2 \right] \quad (4.13)$$

Using the same moment order as presented in the gamma distribution, the three input parameters are expressed as follows [51, 96]:

$$N_T = \exp[(24L_3 - 27L_4 + 6L_6)/3] \quad (4.14)$$

$$\mu = [(-10L_3 + 13.5L_4 - 3.5L_6)/3] \quad (4.15)$$

$$\sigma^2 = [(2L_3 - 3L_4 + L_6)/3] \quad (4.16)$$

where L_3 , L_4 , and L_6 represent the natural logarithms of the measured moments M_3 , M_4 and M_6 respectively.

In the case of Lognormal distribution, the scatter plot for widespread rain is chosen and presented in Figure 4.4. The lognormal model parameters are fitted with different laws as with the case of the gamma distribution, the only change is in the correlation coefficients, which is better compared to the gamma distribution. Table 4.3 shows a summary of the fitted lognormal model parameters for different rain regimes.

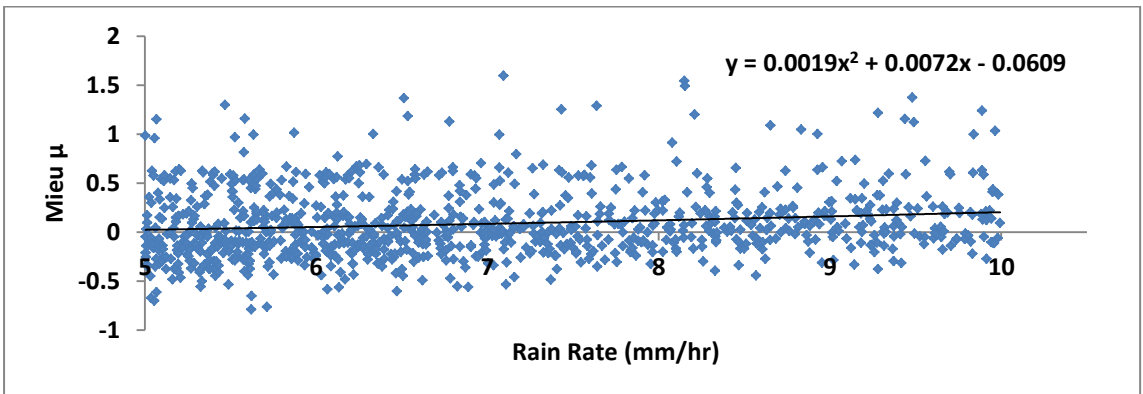
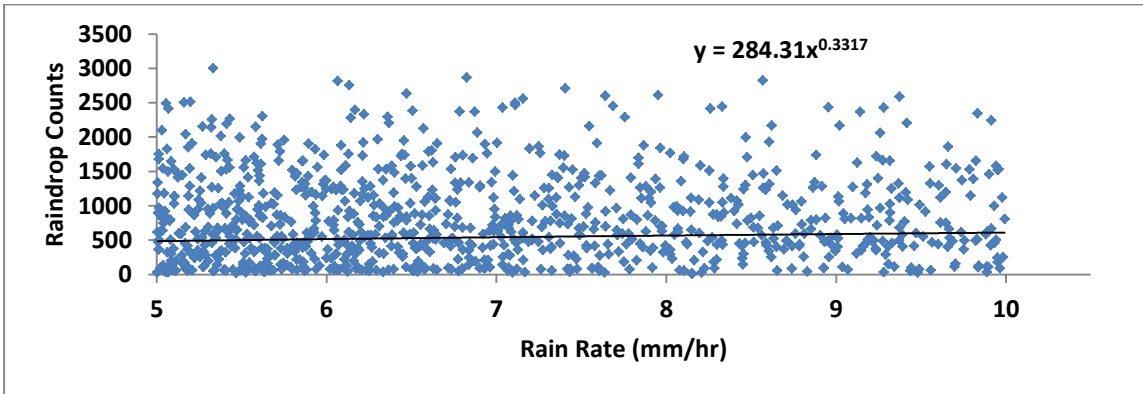
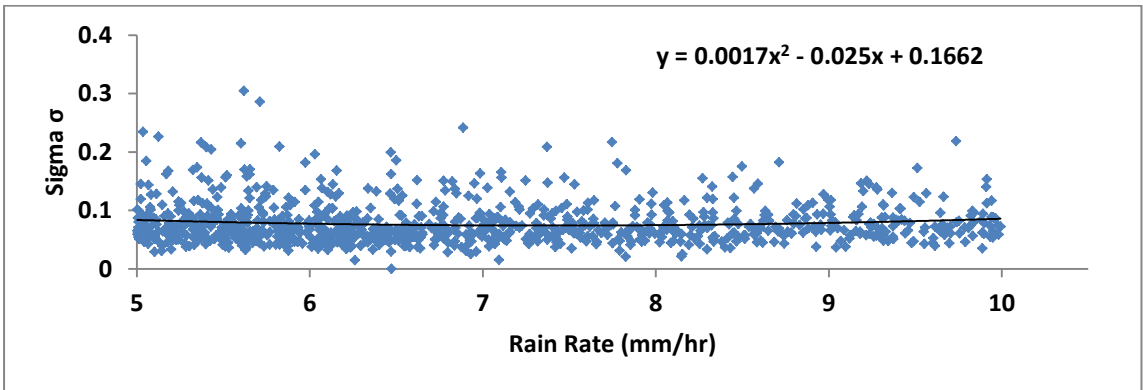
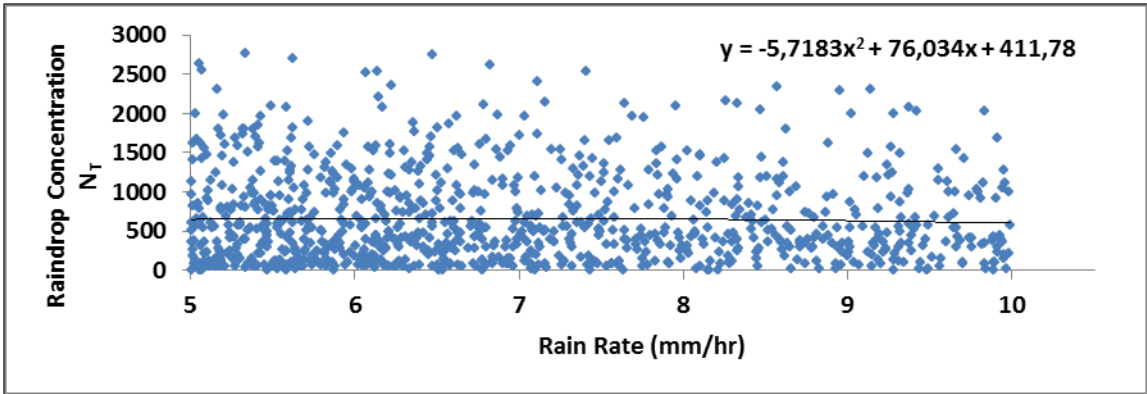


Figure 4.4: Scatter plots for widespread: Lognormal parameters against rain rate

Table 4.2: Summary of Lognormal Parameter Model for Raindrop size Distribution in Durban

Rain regime	Raindrop Count	Raindrop Concentration N_T	Mieu, μ	Sigma, σ
Thunderstorm	$531.39R^{0.0912}$	$0.051R^2 - 4.0654R + 662.28$	$0.17R^{0.2727}$	$2 \times 10^{-3}R^2 - 0.003R + 0.1895$
Shower	$403.89R^{0.1}$	$-0.0619R^2 + 0.5595R + 518.44$	$0.0003R^2 + 0.0269R + 0.0034$	$0.0644R^{0.0738}$
Widespread	$284.31R^{0.3317}$	$-5.7183R^2 + 76.034R + 411.78$	$0.0017R^2 - 0.025R + 0.1662$	$0.0019R^2 + 0.0072R - 0.0609$
Drizzle	$250.93R^{0.424}$	$-856.82R^2 + 1381.5R + 33.89$	$-5.6587R^2 + 3.22R - 0.8686$	$-0.5759R^2 + 0.3181R + 0.0286$
General	$270.36R^{0.407}$	$221.45R^{0.354}$	$0.1504 \ln(R) - 0.2594$	$0.0088 \ln(R) + 0.0742$

4.6 Comparison and Validation of Results

The accuracy of the proposed models can be evaluated by performing the Root Mean Square Error (RMSE) test as a percentage. The performance technique is employed as prescribed and used by several authors who have worked in this area of study [75, 76, 87]. The expression is presented as:

$$RMSE = 100 X \sqrt{\frac{1}{N} \sum_{i=1}^N [N(D_i) - modelled N(D_i)]^2} \quad (4.17)$$

where $N(D_i)$ is the calculated droplet size of the measured data, and N denotes the number of channels provided by the distrometer measurement system. The modeled $N(D_i)$ represents the proposed and existing models from other regions of the world. Although, the RMSE is used in this work because it is widely employed to describe the average model performance, nevertheless, it has been reported to be inappropriate and could lead to misinterpretation of the average error [98].

Figure 4.5 shows the measured DSD data and existing models like the modified gamma distribution model [99, 100] (Singapore model) and lognormal model [15] (proposed and West African model) and the proposed gamma model. Table 4.3 gives a summary of the percentage of RMSE for different rain rates and raindrop size distribution models. Table 4.3 shows that the RMSE ranges between 3.72% and 52.73%. The table reveals that as the rain rate increases, the RMSE increases progressively in all the compared models. The highest value of RMSE is recorded in the modified gamma model (Singapore) and the least RMSE is observed in the proposed lognormal model. Based on the RMSE, the best performance of the proposed and existing models are presented as follows: modified gamma

model (Singapore), Lognormal model (Singapore), proposed gamma model, Lognormal model (West Africa) and proposed Lognormal model.

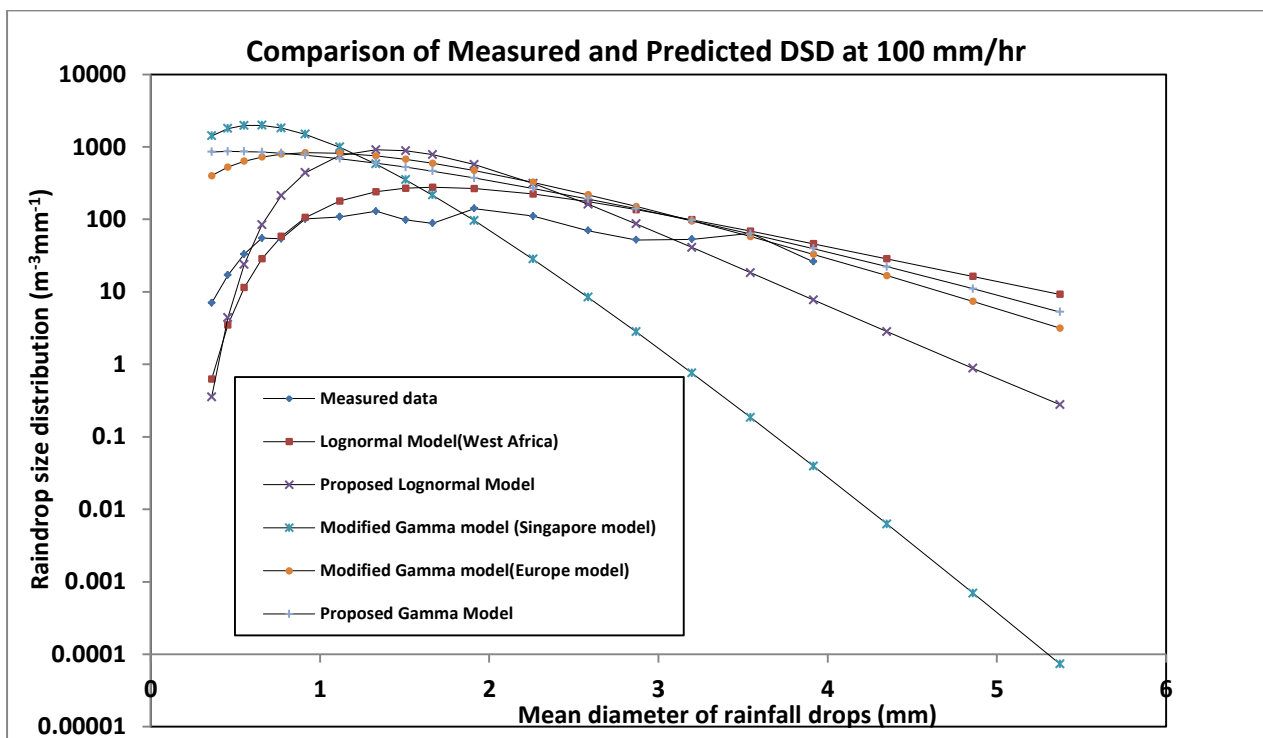
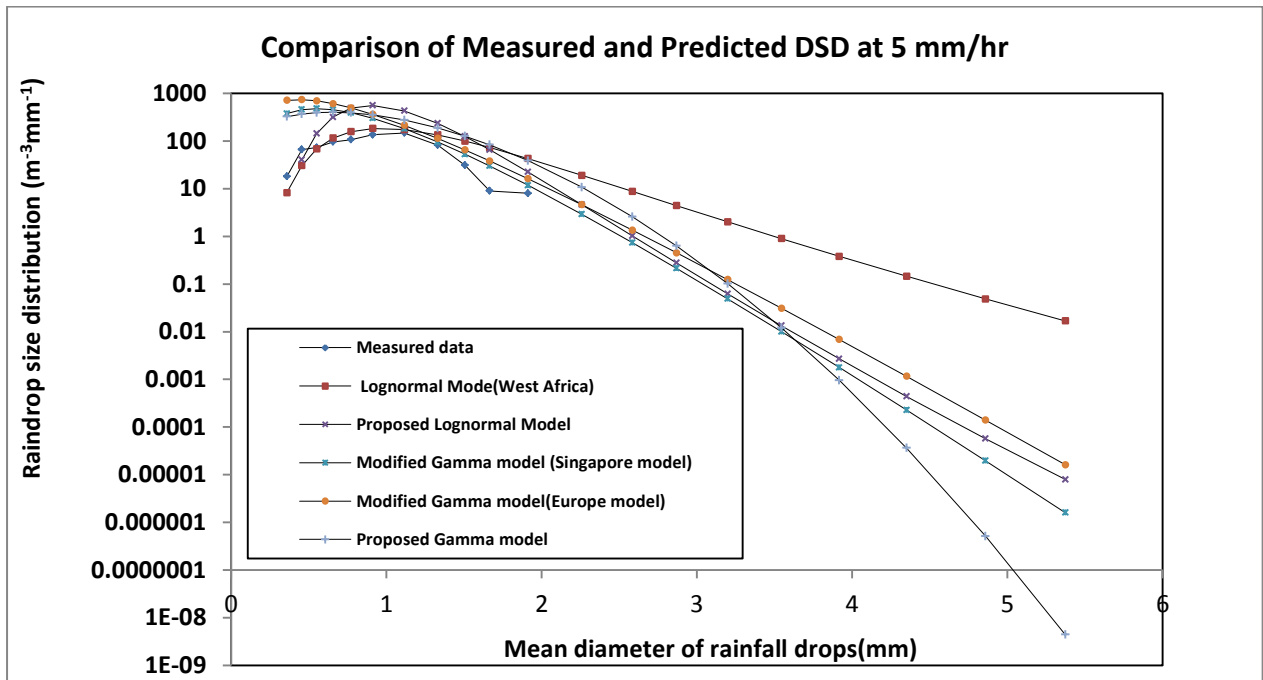


Figure 4.5: Comparative studies of the proposed model with existing ones at different rain rate

Table 4.3: RMSE for different raindrop size distribution models in Percentage

Rain Rate (mm/hr)	Lognormal Model: West Africa	Lognormal Model: Singapore	Modified Gamma: Singapore	Proposed Lognormal Model for South Africa	Proposed Gamma Model for South Africa
5	7.99	11.89	9.05	3.72	9.14
10	9.23	14.90	12.19	4.21	11.15
25	10.85	19.49	19.55	4.72	13.92
100	13.73	28.33	52.73	6.38	17.94

4.7 Specific Rain Attenuation

In this chapter, we used the Mie Scattering theory to calculate specific rain attenuation using local rain rate and drop size distribution data collected in Durban, South Africa. Since in this chapter our interest is to study the characteristics of the specific attenuation in different rain classes, the adoption of the Mie Scattering has been considered. The polarization independent specific rain attenuation denoted by A_s (dB/km) is calculated by integrating the raindrop size distribution models and is given, as in [95, 96, 101], by:

$$A_s = 4.343 \times 10^{-3} \int_0^{\infty} Q(D, \lambda, m) N(D) dD \quad (4.18)$$

where Q is the total extinction cross-section in mm^2 which depends on the drop diameter D , the wavelength λ , and the complex refractive index of the raindrop m . The refractive index of the raindrop also depends on the propagating frequency, temperature and drop size distribution. Q is given as:

$$Q(D, \lambda, m) = \frac{\lambda^2}{2\pi} \text{Re} \sum_{n=1}^{\infty} (2n+1)(a_n + b_n) \quad (4.19)$$

where Re is the real part of the expression (18), a_n and b_n are the Mie scattering coefficients which depend on the drop diameter, wavelength and the complex refractive index of the raindrops. The complex refractive index is determined by using the Liebe model [95]. The average maximum temperature of $20^\circ C$ in Durban is adopted. Using the general power law, the specific rain attenuation is equivalent to that shown in Equation (2.17).

In order to determine the coefficients a and b , in Equation (2.17), Equations (4.18) and (4.19) are used for specific attenuation computations and the results fitted as a function of rainfall rate via the regression technique. The specific attenuation is determined for different rain types by using the Liebe complex refractive index model, the terminal velocity and the different raindrop size distribution models based on the rain type regimes. Due to the non-spherical shape of raindrops, a circular polarization is assumed. In order to determine the coefficients for the power law relationship between

specific attenuation A_s and rain rate R (mm/hr), the non-linear optimization regression method is used as recommended by ITU-R P.838-3 [31] and the same approach has been employed by several authors [45, 102]. Thus, the coefficients a and b for different rain types are developed considering circular polarization. Table 4.4 gives a summary of the coefficients with respect to the corresponding rain types. It is noticed that the value of coefficient a decreases progressively as the trend moves from drizzle to the thunderstorm raindrop regime. In the case of the coefficient b , the reverse is the case. As a function of frequency, as the frequency increases, the coefficient a increases as well, while the coefficient b decreases with the increase in frequency in each rain regime.

Figure 4.6 (a) – 4.6(d) represent the specific rain attenuation for the drizzle, widespread, shower, thunderstorm and the models compared with the general model derived from the combined rain drop size data, and ITU-R P.838-3 specific rain attenuation for the frequency range 1 – 100 GHz [31]. It is worth mentioning here that the ITU-R model is based on the Laws-Parsons DSD model, which may not be adequate in a region such as Durban, which is located in the sub-tropical region of the country. It is observed from Figure 4.6 that the specific rain attenuation increases with frequency. The most pronounced specific rain attenuation is recorded in the thunderstorm rain regime while the least value of the specific rain attenuation is found in the drizzle regime.

Considering the frequency of 5 GHz at rain rates of 4 mm/hr, 9 mm/hr, 30 mm/hr and 100 mm/hr, the specific rain attenuation will increase by 67% between the drizzle rain regime and the widespread rain regime. In the case of drizzle and thunderstorm regimes, the increase is approximately 2145 %.

At the same specified rain rates and frequency of 50 GHz, the drizzle/widespread increase is 69%, while drizzle/thunderstorm increase records approximately 1182%. At 100 GHz, the least percentage difference is observed for the drizzle/widespread and drizzle/thunderstorm; the values are 35% and 431% respectively. In the case of the general models, the results obtained for drizzle shows about 10% increase in specific attenuation compared to that obtained using the dedicated drizzle model. For rain rates of 9 mm/hr, 30 mm/hr and 100 mm/hr, the specific rain attenuation is less compared to that obtained through the corresponding regime dedicated models for widespread, shower and thunderstorm respectively. Another notable point in Figure 4.6 is that the ITU-R model overestimated almost in all rain regimes with a less discrepancy at low rain rates. The progressive increase in the differences between the ITU-R model and the proposed models with increased rain rate is an indication of the difference between the proposed DSD models and the Laws-Parsons DSD model.

Table 4.4: Specific rain attenuation power law coefficients for different rain types

Frequency (GHz)	Drizzle		Widespread		Shower		Thunderstorm		General	
	<i>a</i>	<i>b</i>	<i>a</i>	<i>b</i>	<i>a</i>	<i>b</i>	<i>a</i>	<i>b</i>	<i>a</i>	<i>b</i>
5	0.0008	0.9679	0.0007	0.905	0.0004	1.0816	0.0003	1.18	0.00055	1.0336
10	0.0047	1.0554	0.0034	1.199	0.0026	1.2983	0.0029	1.2661	0.0034	1.2048
15	0.0152	1.1032	0.0127	1.177	0.0143	1.1396	0.0177	1.0833	0.01497	1.1258
20	0.0333	1.072	0.0287	1.112	0.0302	1.0989	0.0377	1.0392	0.03247	1.0807
25	0.0591	1.0303	0.0523	1.037	0.0482	1.069	0.0568	1.0252	0.0541	1.0405
30	0.0937	1.0125	0.086	0.989	0.0772	1.0296	0.0906	0.9871	0.0868	1.0046
35	0.1368	1.004	0.1302	0.955	0.1196	0.9871	0.143	0.9394	0.1324	0.9713
40	0.1872	0.9934	0.1849	0.917	0.1709	0.9473	0.2053	0.8984	0.18707	0.9391
50	0.3094	0.9591	0.3373	0.806	0.2889	0.8621	0.3176	0.8371	0.3133	0.8662
60	0.4665	0.9271	0.5784	0.681	0.4621	0.7592	0.4363	0.7752	0.4858	0.7856
70	0.6538	0.9086	0.9017	0.589	0.7272	0.6632	0.6185	0.7072	0.7253	0.7171
80	0.8273	0.9003	1.2113	0.541	1.0107	0.6028	0.8267	0.6571	0.969	0.6753
90	0.932	0.8967	1.4023	0.520	1.196	0.5735	0.9659	0.6312	1.12405	0.6554
100	0.9586	0.8954	1.457	0.512	1.2534	0.5625	1.0071	0.6215	1.16902	0.6479
ITU-R,P.838-3 [31]										
Frequency (GHz)	<i>a(Horizontal)</i>		<i>b(Horizontal)</i>		<i>a(Vertical)</i>		<i>b(Vertical)</i>			
5	0.0002162		1.6969		0.0002428		1.5317			
10	0.01217		1.2571		0.01129		1.2156			
15	0.04481		1.1233		0.05008		1.0440			
20	0.09164		1.0568		0.09611		0.9847			
25	0.1571		0.9991		0.1533		0.9491			
30	0.2403		0.9485		0.2291		0.9129			
35	0.3374		0.9047		0.3224		0.8761			
40	0.4431		0.8673		0.4274		0.8421			
50	0.6600		0.8084		0.6472		0.7886			
60	0.8606		0.7656		0.8515		0.7486			
70	1.0315		0.7345		1.0253		0.7215			
80	1.1704		0.7115		1.1668		0.7021			
90	1.2807		0.6944		1.2795		0.6876			
100	1.3671		0.6815		1.3680		0.6765			

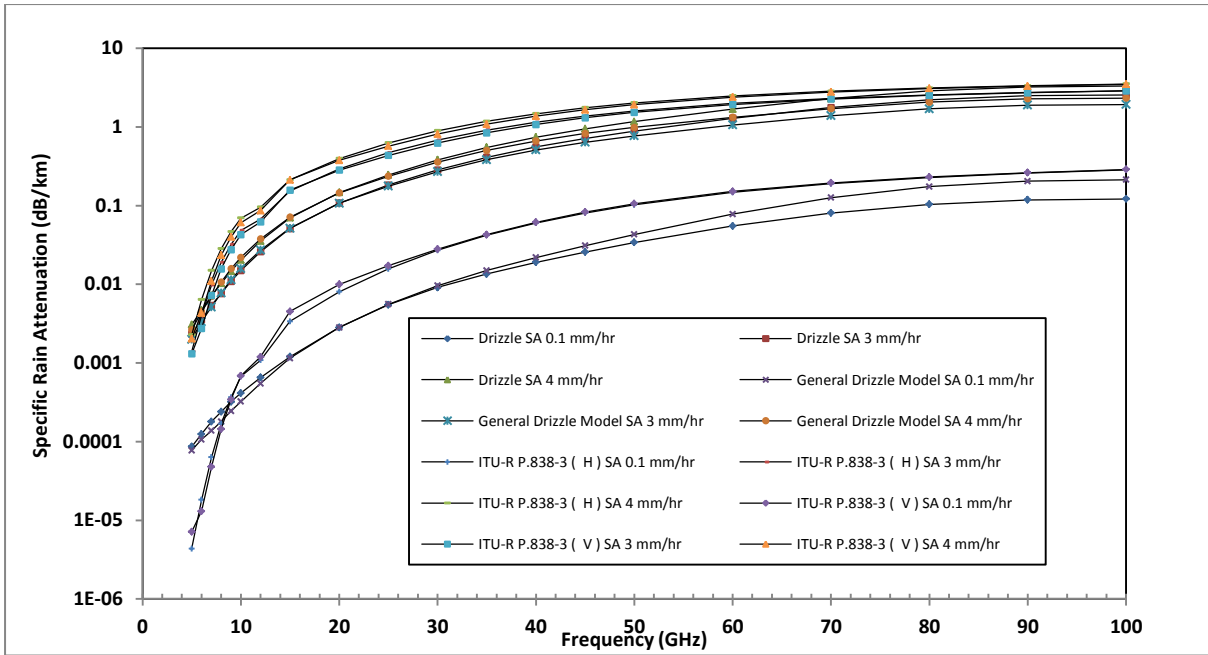


Figure 4.6a: Specific rain attenuation for different rain types and general model

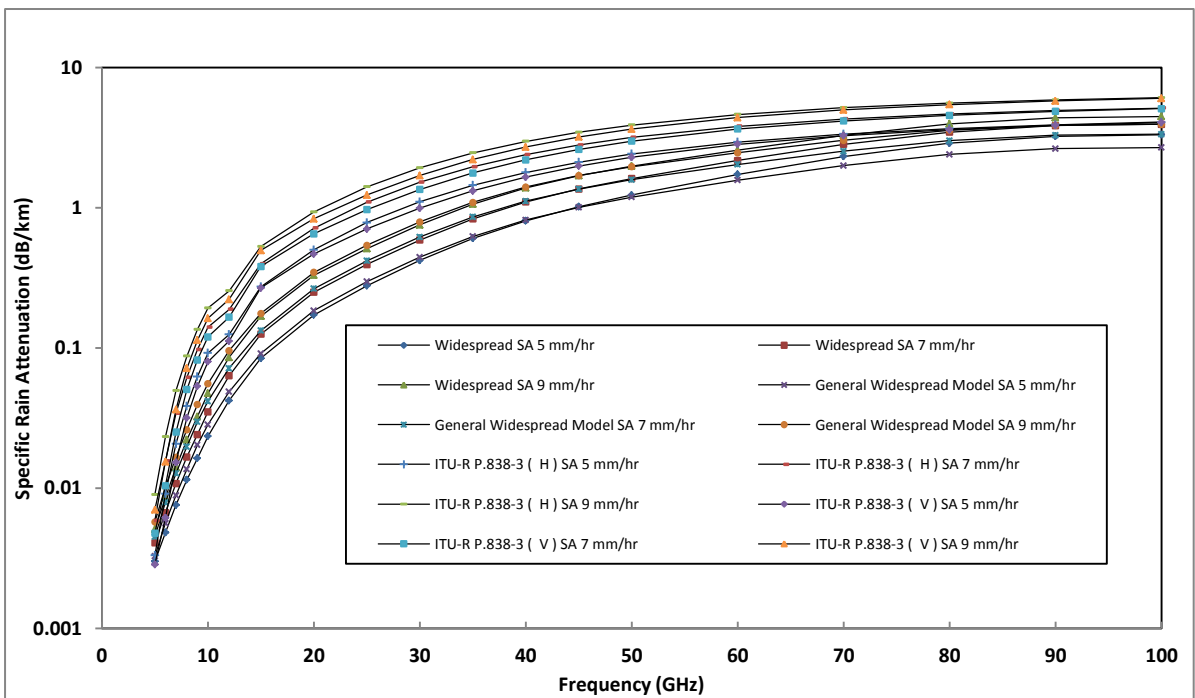


Figure 4.6b: Specific rain attenuation for different rain types and general model

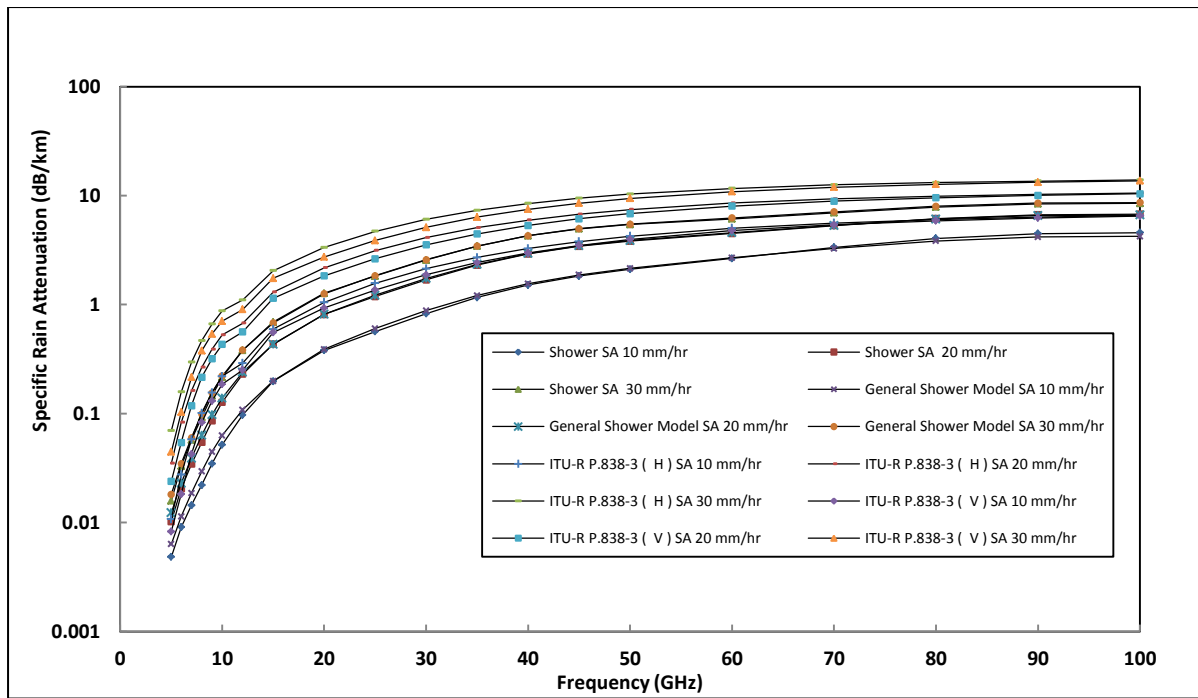


Figure 4.6c: Specific rain attenuation for different rain types and general model

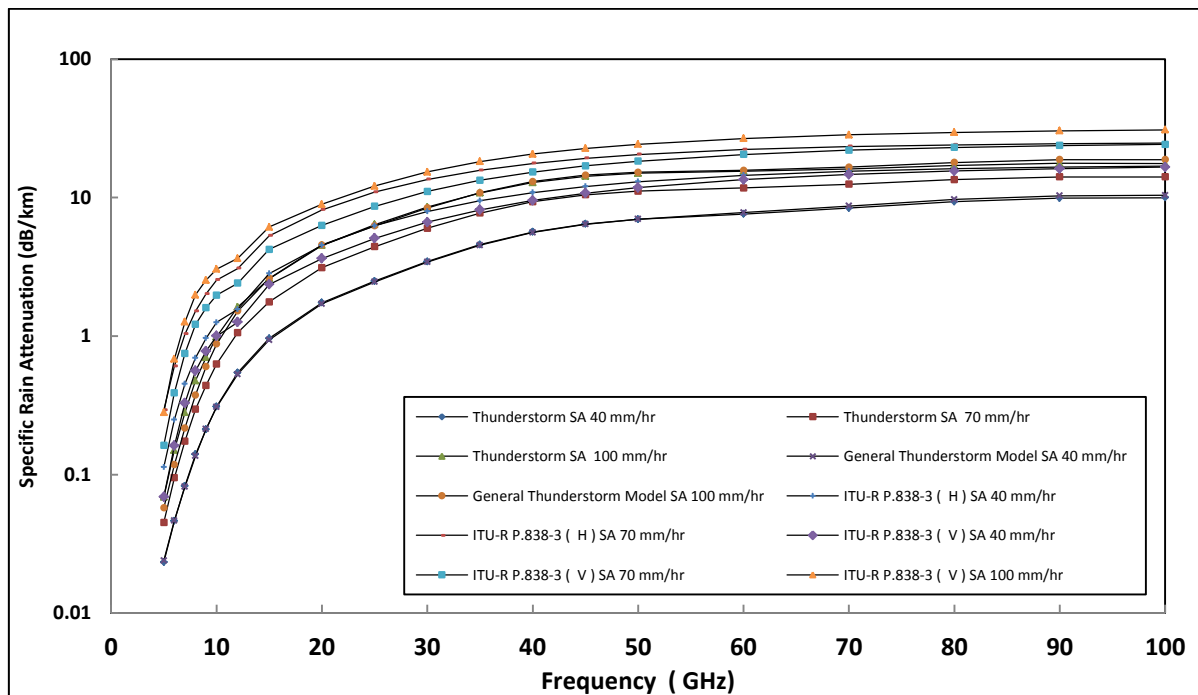


Figure 4.6 d: Specific rain attenuation for different rain types and general model

4.8 Chapter Summary and Conclusion

In this chapter, raindrop size distribution data is modeled using the method of moments and fitted with Lognormal and modified Gamma distributions. The former is considered because of its average

correlation coefficients. The results of the proposed model are compared with two sub-tropical and tropical models: West Africa's Lognormal model and Singapore's modified Gamma and Lognormal model. The results show that the proposed model performs better at all chosen rain types.

The proposed rain dropsize models are applied to determine specific rain attenuation coefficients for different rain types and compared to the general model which comprises of all raindrop size distributions. With the exception of the drizzle rain type, the value of the specific rain attenuation obtained using the general model is less compared to the one obtained through their respective dedicated models. The specific rain attenuation for drizzle is 10% higher when employing the general model as opposed to that obtained from the dedicated model. The results of the proposed raindrop size distribution models and specific rain attenuation coefficients may be of great interest to satellite and terrestrial systems designers in Southern Africa.

Chapter 5

Specific Rain Attenuation Computation Using Different Total Cross Section Models

5.0 Introduction

In this chapter, the specific attenuation due to rain is computed using different total cross section models, while the raindrop size distribution is characterized for different rain regimes in the frequency range between 1 and 100 GHz. The Method of Moments is used to model raindrop size distributions, while different extinction coefficients are used to compute the specific rain attenuation. Comparison of theoretical results of the existing models and the proposed models against experimental outcomes for horizontal and vertical polarizations at different rain rates are presented.

5.1 Rain Drop Size Modelling

The advantages offered by Super High Frequency (SHF) and Extremely High Frequency (EHF) bands such as large bandwidth, small antenna size, and easy installation or deployment have motivated the interest of researchers to study various factors that prevent optimum utilization of these bands. Factors such as cloud, hail, fog, snow, ice crystals, and rain degrade terrestrial and satellite link performance at these frequencies. Rain fade remains the dominant factor in signal fading over satellite and terrestrial links, especially in the tropical and sub-tropical regions like South Africa. In this chapter, the focus is on signal attenuation due to absorption and scattering by rain. While other types of hydrometeors such as water vapour, snowfall, and hail are considered secondary deleterious factors to link design at these frequency bands, attenuation due to rain is a fundamental quantity in the estimation of signal degradation in the presence of precipitation for terrestrial and satellite links. As presented in several articles, a simple power-law relationship of specific rain attenuation as given in equation (2.17) is widely used, and the values of the coefficient parameters k and α are listed in the International Telecommunication Union Recommendation ITU-R P.838.3 [31].

It is evident from several contributors in this area of research [15, 103, 104] that the parameters k and α in Equation (2.17) vary with the raindrop size distribution (DSD). It is observed as well that the rain DSD is location and climate dependent. In order to account for the degree of rain attenuation or rain fade in a link, two methods are often considered: the direct method (which refers to direct measurements at the receiver using a spectrum analyzer), and the statistical method (which involves rain rate and raindrop size measurement). The rain rate and raindrop size measurements allow for the estimation of rain attenuation in a cost-effective way as compared with the direct method. Regional and global efforts have been made to obtain suitable distribution functions and related parameters for the raindrop size distribution (DSD). The early DSD models were based on exponential [3]

distribution functions which poorly represented the very small and very large raindrops. The other distribution functions that have been suggested are the Lognormal [15, 87], the Weibull [95, 105], and the gamma [106] distribution functions. There are several ways of fitting measured DSD data, of which the method of moments [107] and maximum likelihood estimation [108] are the most popularly used by many authors. While DSD measurement campaigns have been reported over a considerable period of time in West Africa [65, 109], less work has been done in this particular area in Southern Africa [2, 73].

One of the aims of this chapter is to give a report on the current DSD modelling for the South African region and its application using different extinction cross section models. The resulting fitted DSD is integrated over the scattering cross section to calculate the specific attenuation due to rain. In order to estimate the total cross sectional area of raindrops, the choice of rain shape is the key parameter. Morrison and Cross [110] fitted the rain drop shape with a spheroidal model, using the least-squares method. The contribution of Pruppacher and Pitter [5], presented theoretical results of raindrops at different sizes, while Li *et al.* [111, 112] further simplified Pruppacher and Pitter's model, with the expression:

$$r = a(1 - v_1) \left[f_0(\theta) + \frac{v_1}{1 - v_1} f_1(\theta) \right]$$

$$= \begin{cases} a(1 - v_1) \left[1 + \frac{v_1}{1 - v_1} \sin^2 \theta \right], & 0 \leq \theta \leq \pi/2 \\ a(1 - v_2) \left[1 + \frac{v_2}{1 - v_2} \sin^2 \theta \right], & \pi/2 \leq \theta \leq \pi \end{cases} \quad (5.1)$$

where,

$$a = 1.111582a_0 \quad (5.2a)$$

$$v_1 = 1.375447 \times 10^{-2} + 6.543960 \times 10^{-2}a \quad (5.2b)$$

$$v_2 = -7.239211 \times 10^{-2} + 1.827561 \times 10^{-1}a \quad (5.2c)$$

$$f_0(\theta) = 1 - \frac{v_2 - v_1}{1 - v_1} H\left(\theta - \frac{\pi}{2}\right) \quad (5.2d)$$

$$f_1(\theta) = \left[1 + \frac{v_2 - v_1}{1 - v_1} H\left(\theta - \frac{\pi}{2}\right) \right] \sin^2 \theta \quad (5.2e)$$

where a_0 denotes the mean raindrop radius, theoretically given as 0.25 mm to 3.00 mm with an incremental interval of 0.25 mm, and $H(\theta)$ denotes the step function. Equations (5.1) to (5.2) represent the spherical raindrop size model. Another approach with a new formula was presented [113] - in which case the scattered electromagnetic fields were deemed due to spheroidal raindrops. Considering spheroidal raindrop scatterers, the surface of the drops is described by [113]:

$$r = \frac{a}{\sqrt{1 - v \sin^2 \theta}} \approx a \left[1 + \frac{1}{2} v \sin^2 \theta \right] \quad (5.3)$$

where $v = 1 - ((a/b)^2)$, and a and b represent the raindrop's minor and major semi-axes respectively, and are measured in centimeters. In [113] Oguchi's method was used to obtain a and b from the mean drop size radius \bar{a} that was developed to determine the specific rainfall attenuation. Oguchi [114] assumed that:

$$ab^2 = \bar{a}^3 \quad ; \quad \frac{a}{b} = \left(1 - \frac{4.1}{4.5} \bar{a}\right) \quad (5.4)$$

The other method presented in [113] is that of Morrison and Cross [110], which assumes that:

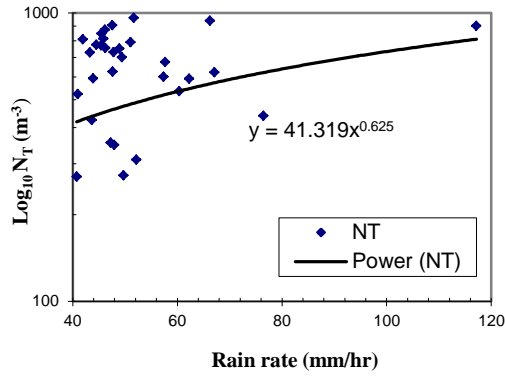
$$ab^2 = \bar{a}^3 \quad ; \quad \frac{a}{b} = 1 - \bar{a} \quad (5.5)$$

The parameters obtained using the method of Morrison and Cross have shown reasonably consistent results when considering larger raindrops as opposed to that proposed by Oguchi [114]. In this chapter, the aforementioned total scattering cross section of Morrison and Cross [110], alongside the Pruppacher and Pitter model [5] as well as the Mie scattering model, are used to compute the specific attenuation due to rain for Southern Africa.

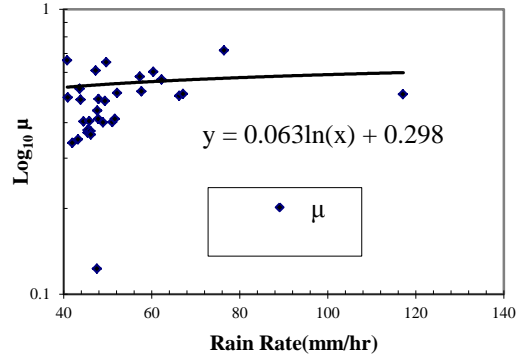
5.2 Data Collection and Modelling

For the purpose of this work, two-year DSD data was collected using the Joss-Waldvogel RD-80 disdrometer (JWD) [115] at an integration time of one minute. This equipment is placed at latitude $30^{\circ}58' E$ and longitude $29^{\circ}52' S$ on top of the Electrical, Electronic, and Computer Engineering building, University of KwaZulu-Natal, at an altitude of 139.7 m above sea-level. It measures raindrop diameters in the range of 0.3 mm to 5 mm in 20 different bins, with the accuracy of $\pm 5\%$.

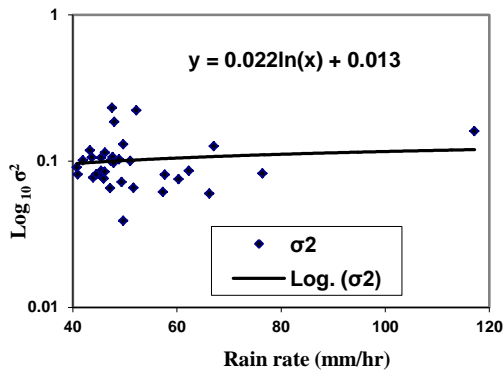
The expressions used to estimate the measured rain rate (mm/hr) by the equipment is presented in the JWD manual as in (4.2, 4.3). With the nature of rain distribution in Southern Africa, the rain rate is used to classify the raindrop size distribution models into four classes as given in Section 4.2. The rain rate is estimated from the modelled $N(D_i)$ for each class of rain rate type, as given in Equation (4.1). Comparative studies of the measured $N(D_i)$ and modelled $N(D_i)$, are done using the percentage RMSE as given in Equation (4.17). The MoM method is then used to determine the three parameter Lognormal DSD model (refer to Section 4.5).



(a)



(b)



(c)

Figure 5.1: Scattergrams of estimated Lognormal parameters (a) N_T (b) μ and (c) σ^2 , versus the rain rate for the thunderstorm rain type

Figure 5.1 presents logarithmic scattergrams of Lognormal DSD parameters versus rain rate for the thunderstorm rain type. These parameters are derived from Equations (4.14) –(4.16). For the other rain types such as drizzle, widespread and shower, Table 5.1 and expressions presented in Equations (5.6) and (5.7) give details of Lognormal DSD parameters and their coefficients for the Southern African region as summarized in the expressions below:

$$N_T = a_0 R^{b_0} \quad (5.6)$$

$$\mu = A_\mu + B_\mu \ln R \quad (5.7)$$

5.3 Application of Rainfall Regimes

It has been established that the raindrop size distribution varies considerably for different types of rainfall regimes or classes. These rainfall types, as defined in Section 4.2, are: drizzle, widespread, shower and thunderstorm. The corresponding parameters of their Log-normal distributions are shown in Table 5.1. A general distribution model has often been used by many researchers. However, there is a notable difference in the specific attenuation due to rain produced by the general model, hence the need to develop regime-specific rain attenuation models [86, 96].

Table 5.1: Coefficients of Lognormal DSD parameters in Equation (5.6, 5.7) for Southern Africa (SA) and for West Africa (WA) [33]

Rain Type	a_0		b_0		A_μ		B_μ		A_σ		B_σ	
	SA	WA	SA	WA	SA	WA	SA	WA	SA	WA	SA	WA
Drizzle	212.3	718.00	0.387	0.399	-0.281	-0.51	0.131	0.128	0.086	0.038	0.013	0.013
Shower	258.3	137.00	0.095	0.370	-0.321	-0.41	0.242	0.234	0.072	0.223	0.005	-0.03
Wide spread	322.4	264.00	0.102	-0.23	-0.392	-0.47	0.249	0.174	0.083	0.161	-0.003	0.018
Thunder storm	41.3	63.00	0.625	0.491	0.299	-0.18	0.063	0.195	0.014	0.209	0.022	-0.03
General model	220.0	108.00	0.392	0.363	-0.267	-0.20	0.137	0.199	0.077	0.137	0.010	-0.01

Table 5.2: Error analysis (RMSE in %) of the proposed Lognormal model and West Africa model

Rain Type	Lognormal model (West Africa)	Proposed Lognormal Model
Drizzle	8.01	4.03
Shower	9.85	4.53
Widespread	10.98	5.01
Thunderstorm	13.15	6.95
General	11.49	4.14

5.4 Comparison of DSD models in South Africa and West African countries

The performance test analysis of the proposed Log-normal model and its counterpart from West Africa [86] are evaluated using Equation (4.17). The comparison is done by substituting the coefficients in Tables 5.1a and 5.1b into Equations (5.6, 5.7) with measurements carried out in Durban as discussed in section 4.2.

The RMSE model performance test is carried out by taking at least three rain rate samples of each rain type, with the average RMSE in percentage then calculated for each rain type. The proposed Log-normal model performs better than its counterparts across all the rain regimes. The test results agree with RMSE results presented in [96].

The slight deviations of RMSE values recorded are due to the optimum best fit function employed (such as linear, power law, and exponential fits) in [96] and the averaged RMSE calculated for each rain type. The summary of the RMSE performance test is presented in Table 5.2.

5.5 Scattering Properties of Distorted Raindrops

The investigation and successful prediction of the attenuation of plane electromagnetic waves caused by a rainy medium involves an assumption of a particular physical model for the raindrop shape. The total scattering cross-section (extinction cross-section) of the raindrop depends to a great deal on this physical model. Many researchers have adopted a simple approach that assumes raindrops to be spherical in shape and employed the Mie theory to obtain the specific attenuation due to rain. However, it has been established through photographic measurements [116, 117] that realistic raindrops become oblate spheroidal in shape as the drop size gets larger. Raindrops of fairly large size experience severe distortion, and as such, they are no longer spheroidal in shape but look like hamburgers [118, 119]. This loss of shape is accompanied by a loss of symmetry along their axes. The assumption that raindrops are spherical, as adopted by many researchers, is therefore valid only for small raindrops.

5.6 Scattering Coefficients

Scattering coefficients can be obtained by considering different orders of approximations, with the zeroth-order scattering from the spheroid representing the Mie scattering from a sphere [112, 120]. Li *et al* [112, 120] discuss two approaches for obtaining the first-order scattering approximation. The first approach is to modify the scattering coefficients $S_n^a(a_e)$ and $S_n^b(a_e)$ through the use of an effective radius of the spheroid, while the second approach involves the modification of the spherical vector wave functions to the spheroidal ones. The second approach involves lengthy and error-prone

calculations hence it is much easier and more realistic to use the first approach. This approach suggests that the variability of the raindrop shape merely translates to the variability of the effective raindrop radius. For spherical raindrops, the scattering coefficients are expressed in terms of the mean drop radius of the sphere.

The following equation was thus considered to represent the surface of an arbitrarily-distorted scatterer [112, 120]:

$$r = a[1 + vf(\theta', \phi')] \quad (5.8)$$

where θ' and ϕ' represent the zenith and the azimuth angles of the incident waves at which reflection occurs. The above equation clearly shows that for small values of v , $r \approx a$. This implies that the second term in the above equation represents a distortion with respect to a sphere of radius a . It can therefore be considered that the term $a[1 + vf(\theta', \phi')]$ represents the effective radius a_e of an arbitrarily-shaped scatterer [112, 120].

The scattering coefficients are thus given by [100, 101, 109]:

$$S_n^a = -\frac{j_n(\zeta D)[Dj_n(D)]' - j_n(D)[\zeta D j_n(\zeta D)]'}{j_n(\zeta D)[Dh_n^{(2)}(D)]' - h_n^{(2)}(D)[\zeta D j_n(\zeta D)]'} \quad (5.9)$$

$$S_n^b = -\frac{j_n(D)[\zeta D j_n(\zeta D)]' - \zeta^2 j_n(\zeta D)[Dj_n(D)]'}{h_n^{(2)}(D)[\zeta D j_n(\zeta D)]' - \zeta^2 j_n(\zeta D)[Dh_n^{(2)}(D)]'} \quad (5.10)$$

and the parameter D is given by:

$$D = k_0 a [1 + vf(\alpha, 0)] \quad (5.11)$$

where k_0 is the free space wave number and α is the incidence angle.

The parameter D is analogous to the size parameter commonly used in the Mie calculations. Once the shape of the raindrops is known the scattering coefficients can be determined. The extinction (total) cross-section is then calculated based on the different shapes for different models as follows [110, 114]:

$$Q_{ext} = -\frac{2\pi}{k_0^2} \text{Re} \sum_{n=1}^{\infty} (2n+1) [S_n^a(a_e) + S_n^b(a_e)] \quad (5.12)$$

where a_e is the effective raindrop radius given by [114, 115]:

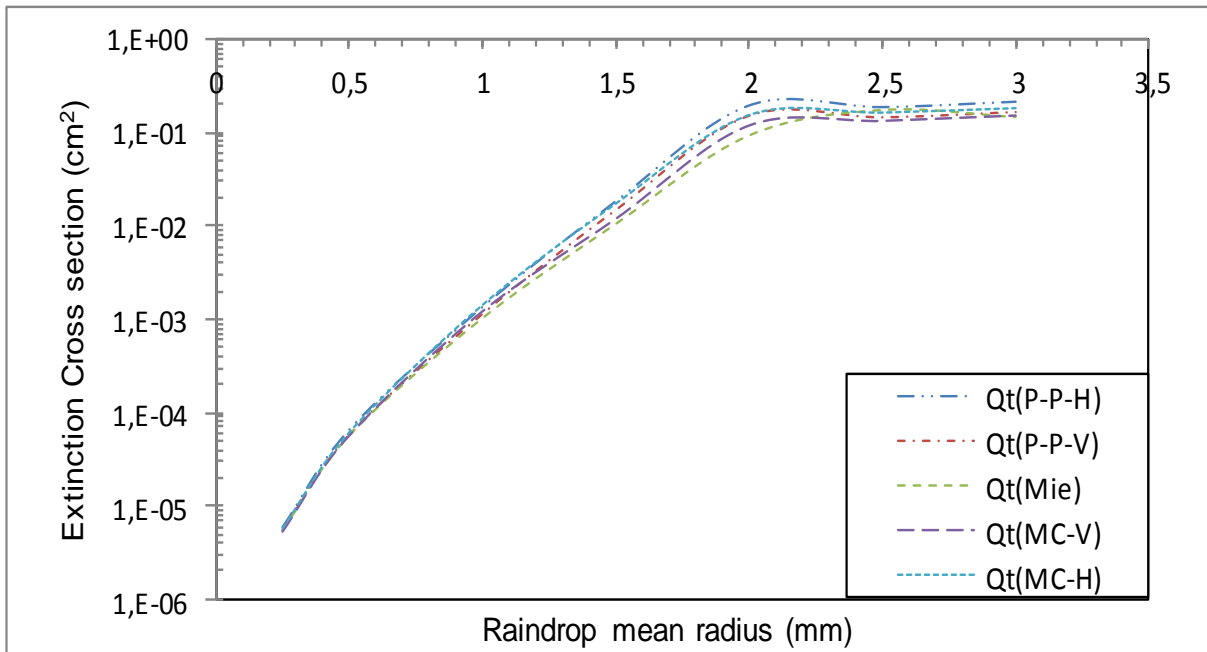
$$a_e = \frac{a}{\sqrt{1-v}} \quad (5.13)$$

5.7 Total Scattering Cross Section

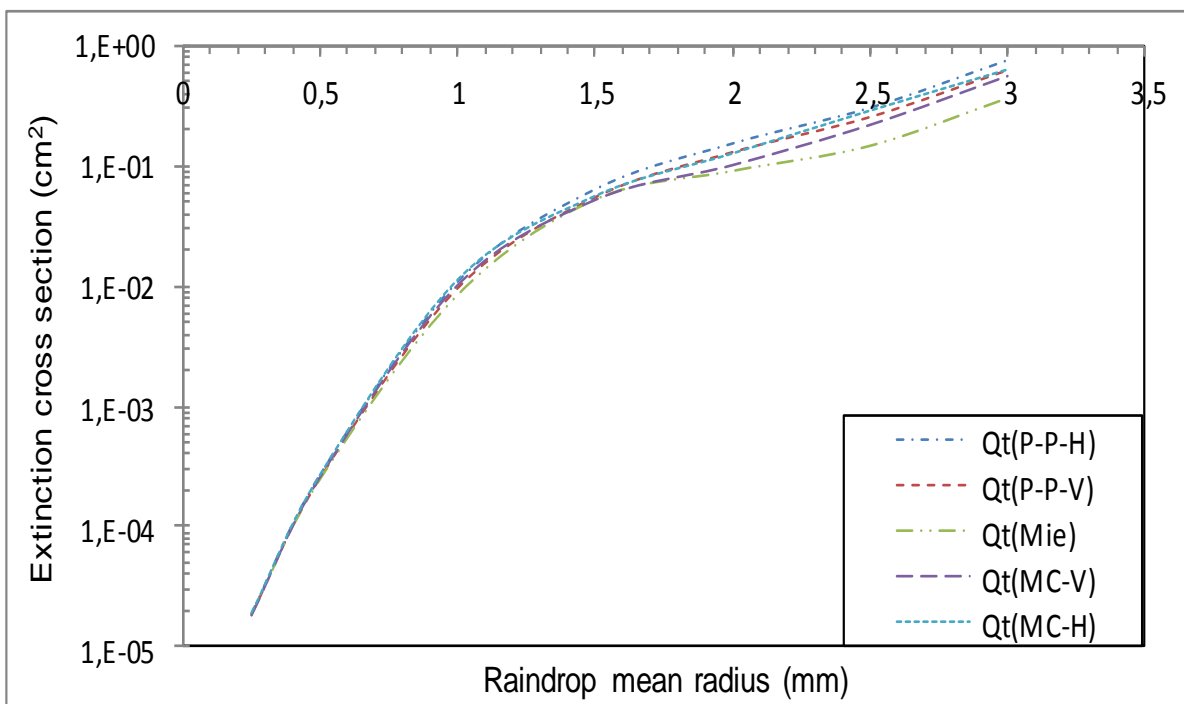
In this chapter, the total scattering cross-section is evaluated and plotted against the mean raindrop radius for three different raindrops shape models. We consider the Morrison and Cross (M-C) model for spheroidal raindrops; the Pruppacher and Pitter (P-P) model for raindrops of any size and shape; and the Mie model for spherical rain drops. The first two models are polarization dependent while the third model is polarization independent. In order to evaluate the effect of polarization using the three total cross-section models, the following six frequencies are used: 7.8 GHz, 13.6 GHz, 19.5 GHz, 34.8 GHz, 140 GHz, and 245.5 GHz. The corresponding complex refractive indices of water at a temperature of 20 degrees Celsius using the method of Liebe *et al* for these frequencies are: $(8.3614+i1.697)$, $(7.5307+i2.4231)$, $(6.7189+i2.7566)$, $(5.2534+i2.8091)$, $(2.9701+i1.5635)$, and $(2.5945+i1.1046)$, respectively.

Fig. 5.2 shows that the different models are in agreement in terms of the extinction cross section for small raindrop diameters and lower frequencies. As the drop diameter increases, a noticeable difference is observed among the models. The Mie model gives the lowest values of extinction cross-section while the higher values are obtained from the M-C and P-P models due to the degree of the raindrops' distortion. The results confirm the inability of the Mie model to realistically represent the raindrop shape, reducing it to a smaller sized sphere in comparison with the realistic spheroid of the M-C and P-P models. Figure 5.2 confirms that different polarizations have different effects on the total cross section. The horizontally-polarized wave records a larger value of total cross-section than its vertical counterpart.

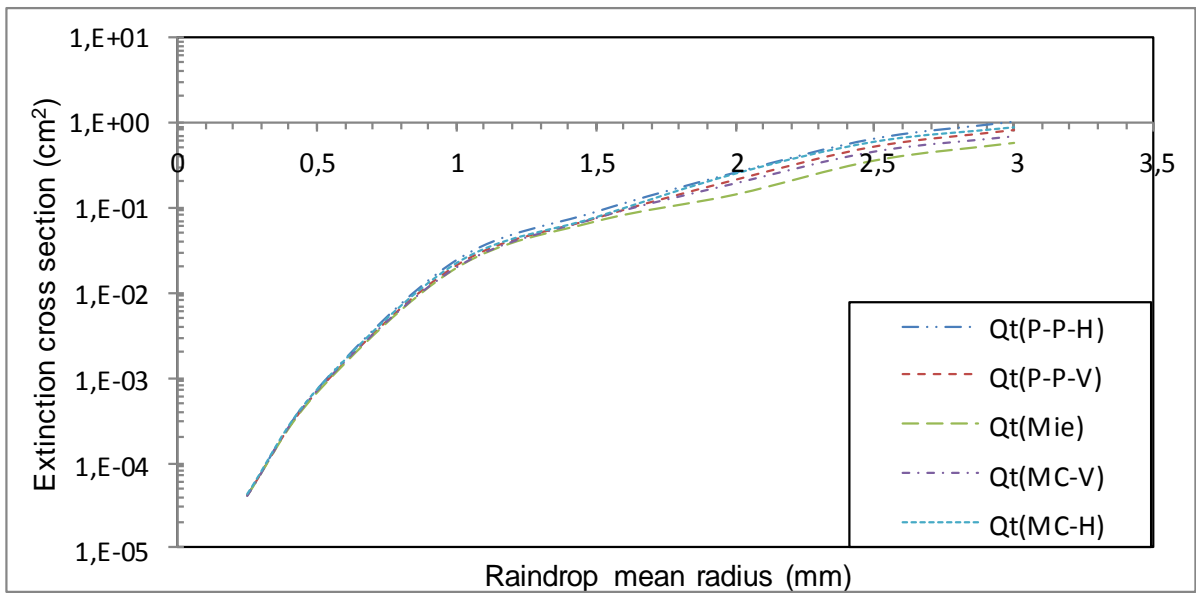
By using the percentage difference between the P-P model and the Mie model at 7.8 GHz, it confirmed that at lower diameters, the percentage difference is minimal. At a diameter of 2 mm, it is seen that the percentage difference with respect to vertical polarization is 11.76%. In the case of horizontal polarization, a similar trend is observed, with the percentage difference of 18.99% at the same diameter. The lower percentage difference is recorded in the M-C model against the Mie model. At a diameter of 2 mm, the percentage differences between the M-C model and the Mie model are 5.60% and 12.23% for vertical and horizontal polarization, respectively. At a frequency of 245.5 GHz, in Figure 5.2(f), the same trend is observed as was the case for the lower frequency (7.8 GHz). The percentage difference at the 245.5 GHz frequency is approximately twice the values reported at the lower frequency.



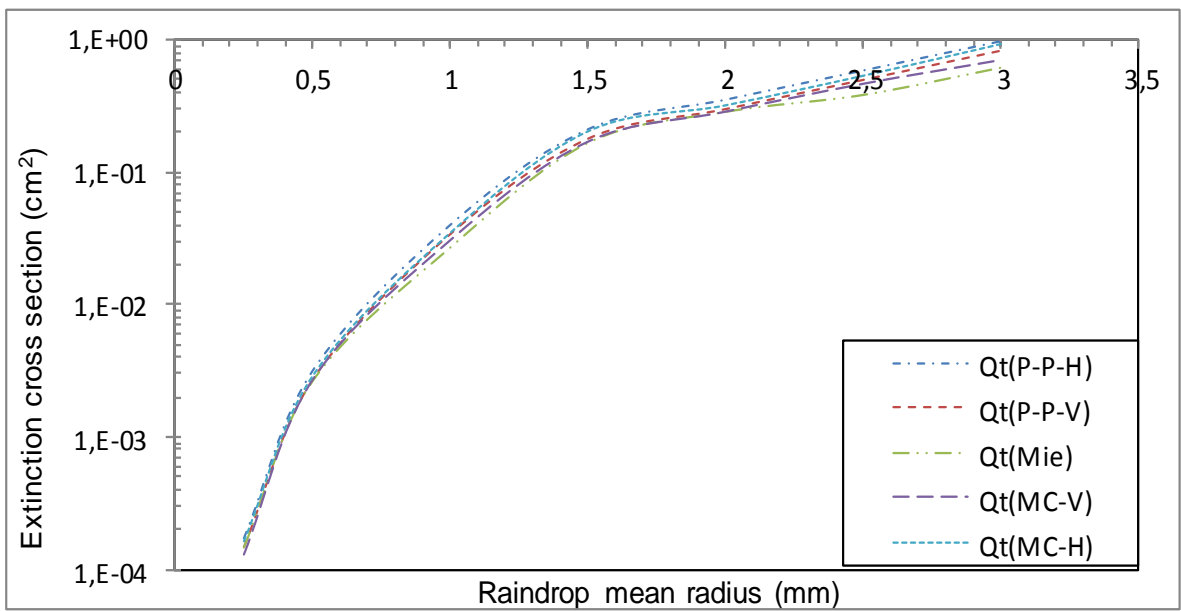
(a) 7.8 GHz



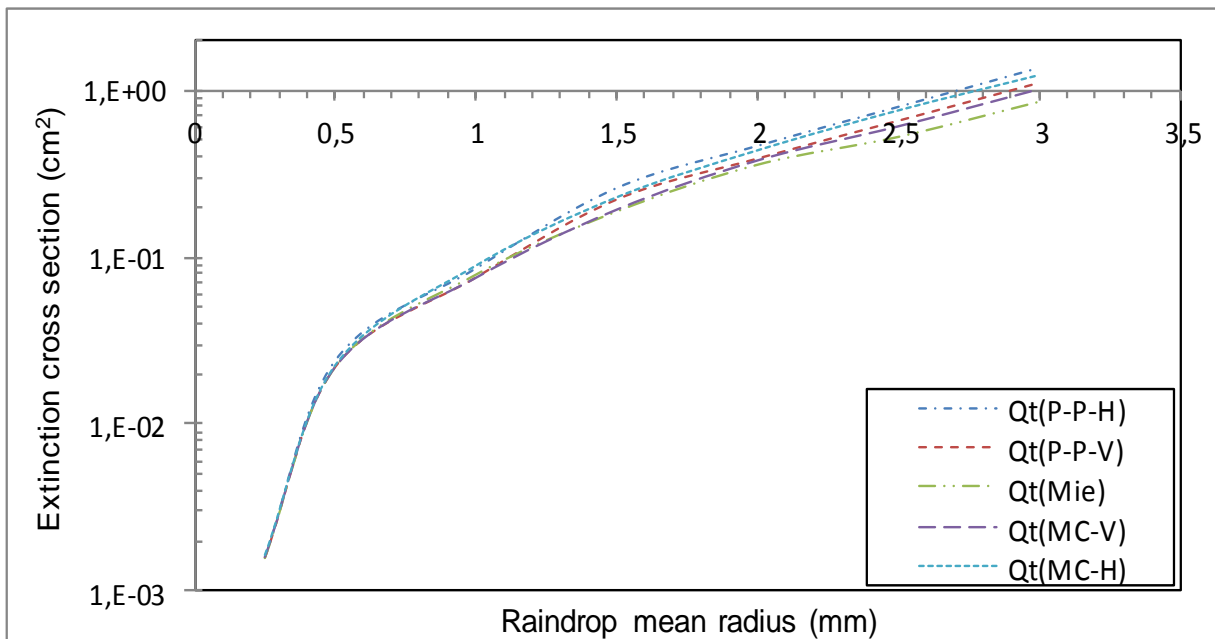
(b) 13.6 GHz



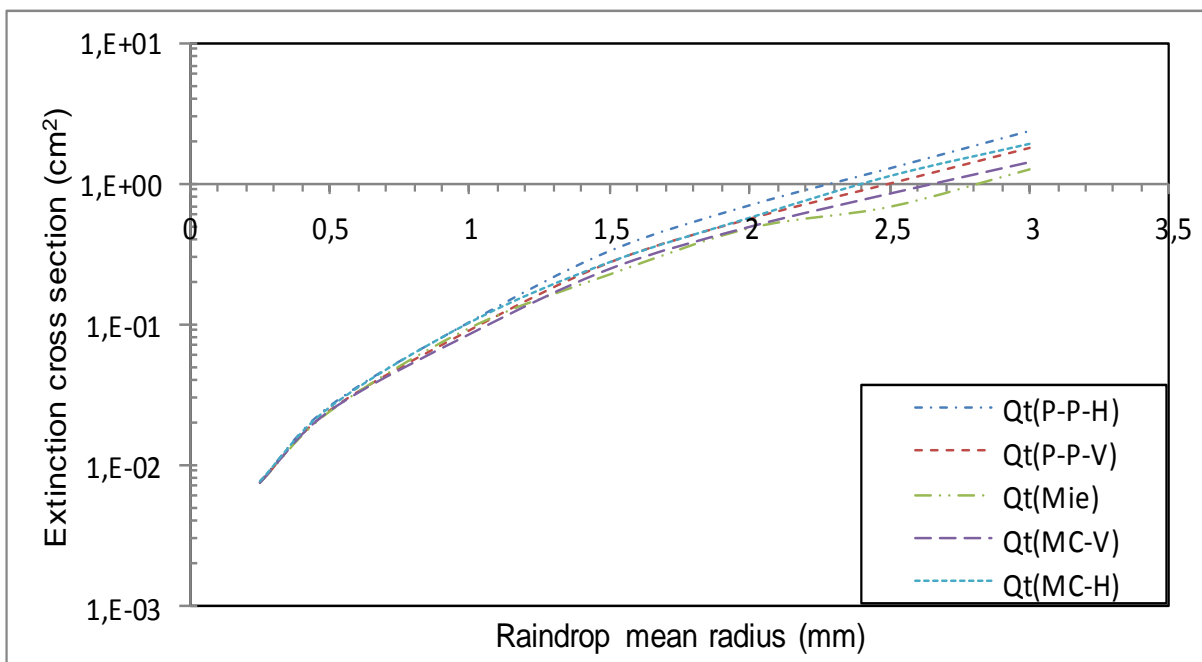
(c) 19.5 GHz



(d) 34.8 GHz



(e) 140 GHz



(f) 245.5 GHz

Figure 5.2: Comparison of extinction cross-sections of MC, P-P, and Mie models at horizontal and vertical polarization versus mean drop radius at (a) 7.8 GHz; (b) 13.6 GHz; (c) 19.5 GHz; (d) 34.8 GHz; (e) 140 GHz; (f) 245.5 GHz

5.8 Specific and Total Rain Attenuation

The prediction of rainfall attenuation is achieved through the numerical integration of the following equation:

$$A = 4.34 \times 10^{-3} \int_0^{D_{max}} Q_{ext}(D)N(D)dD \quad (5.14)$$

where $Q_{ext}(D)$ represents the extinction cross section as given in Equation (5.12) above. $N(D)$ is the mean drop size distribution of the rainfall drops. The impact of distorted raindrops on attenuation due to rain is determined for the P-P model, M-C-model, and Mie model for frequencies up to 100 GHz. The results are plotted on the same set of axes for ease of comparison. As indicated in Section 5.4, comparisons are made by using different total scattering cross-section models at circular polarization to determine specific rain attenuation as shown in Figure 5.3. The choice of circular polarization is considered because of its popularity in satellite communications at SHF and EHF ranges. In order to investigate the variability of specific rain attenuation, a single rain rate has been chosen from each rainfall regime to show the degree of the attenuation impact on the link operating at a given frequency, as shown in Figures 5.3 (a) to 5.3(d).

To highlight the worst case scenarios, the upper band of rain rate values were used for each rain type, namely: 5 mm/hr, 10 mm/hr, 40 mm/hr, and 100 mm/hr for drizzle, widespread, shower, and thunderstorm rain types, respectively. The percentage difference between the specific attenuation due to Mie model and that due to the M-C model is high compared to the difference due to the Mie and the P-P models. The highest average percentage difference in specific attenuation is thus obtained for the thunderstorm rain type with the M-C model, giving a value of 31.47%; while its P-P model counterpart gives a difference of 30.95%. The lowest difference in specific attenuation is observed with the drizzle rain type, returning values of 9.27% and 15.11% between the Mie and the P-P model and the Mie and the M-C model, respectively.

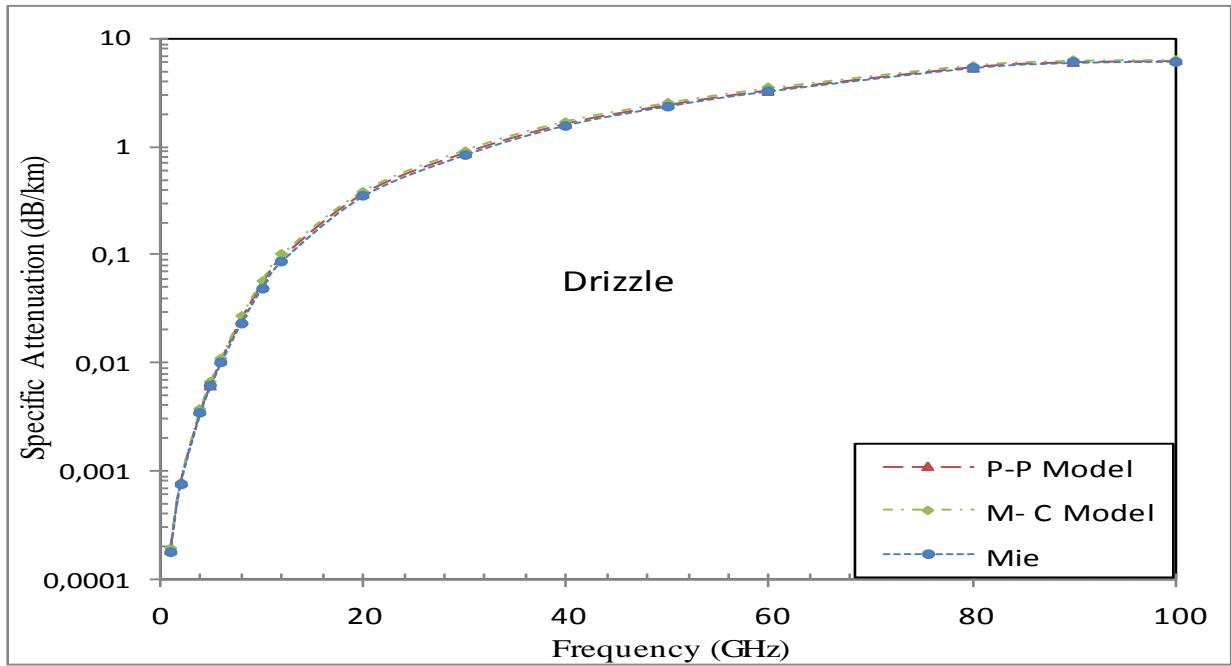
Table 5.3: Comparison of rain attenuation for P-P and MC model against the Mie model at different rain rates at 100 GHz

Rain Type	Attenuation Percentage Difference (%) between Mie and P-P and MC-model	
	P-P model	MC model
Drizzle	4.36	8.98
Widespread	5.96	10.81
Shower	15.35	17.83
Thunderstorm	30.95	31.47

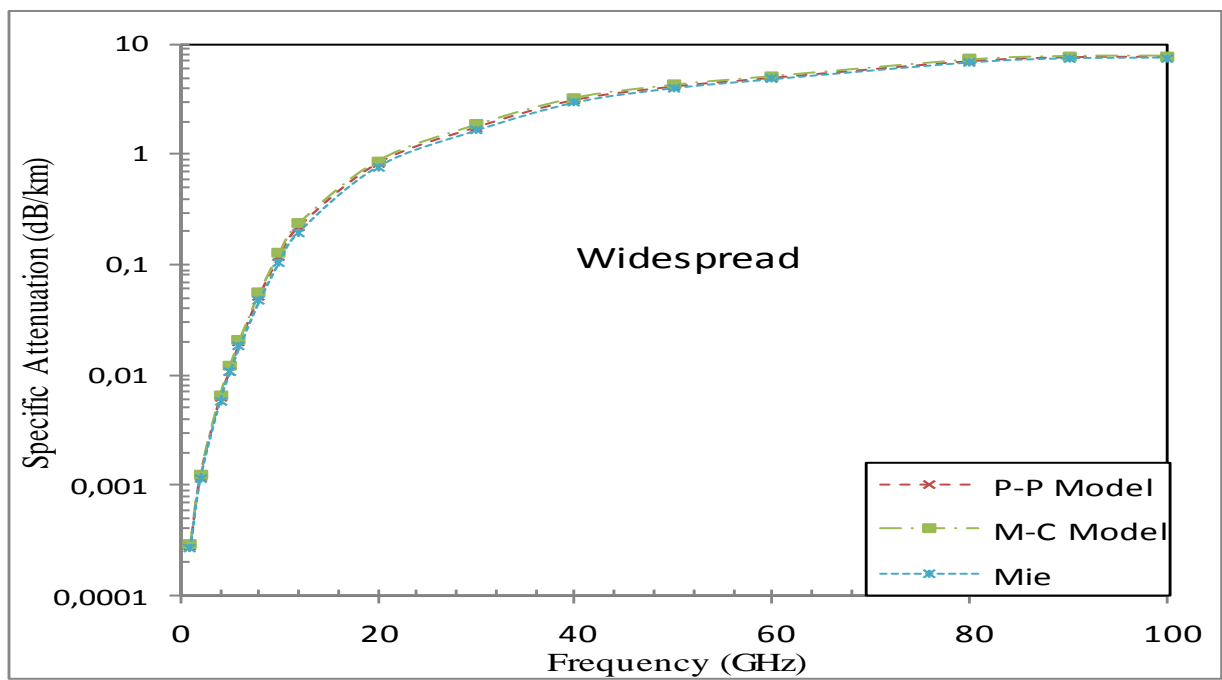
The specific attenuation due to rain in an area gives the radio planner information about the extent to which the transmitted signal will be degraded in the presence of rain. The choice of operating frequency of a radio link is influenced by the rain attenuation and availability stipulations for the service on offer. Figure 5.3 shows the frequency characteristics of the specific rain attenuation for a radio link operating in the four different rain types. It is clear that the severity of signal degradation increases with increasing frequency. This translates into higher fade margin requirements at high frequencies to ensure reliable service for radio link users. Of the three models used in this study, the Mie model stipulates lower fade margin demands at all frequencies, while the M-C model calls for the highest fade margin requirements for all frequencies. The P-P model gives fade margins that lie in between these two.

Considering the specific attenuation due to the different rain types, we can see that the three models are in reasonably good agreement as shown in Fig. 5.3(a) for the drizzle rain type. The drizzle rain type is characteristically dominated by small rain drops and rain rate of at most 5 mm/hr. This is in keeping with the notion that small rain drops are almost spherical in shape. The effective raindrop radius, a_e , of the P-P and M-C models, reduces to nearly that of the spherical model, giving almost the same attenuation levels as those due to the Mie model. However, as the raindrop size increases, the difference in the results from the three models becomes more noticeable. A summary of the percentage differences in specific attenuation between the P-P and M-C models on the one hand, with the Mie model on the other, is shown in Table 5.3. The comparison is made at the frequency of 100 GHz. More importantly, this comparison gives insight into the validity of the widely accepted Mie model.

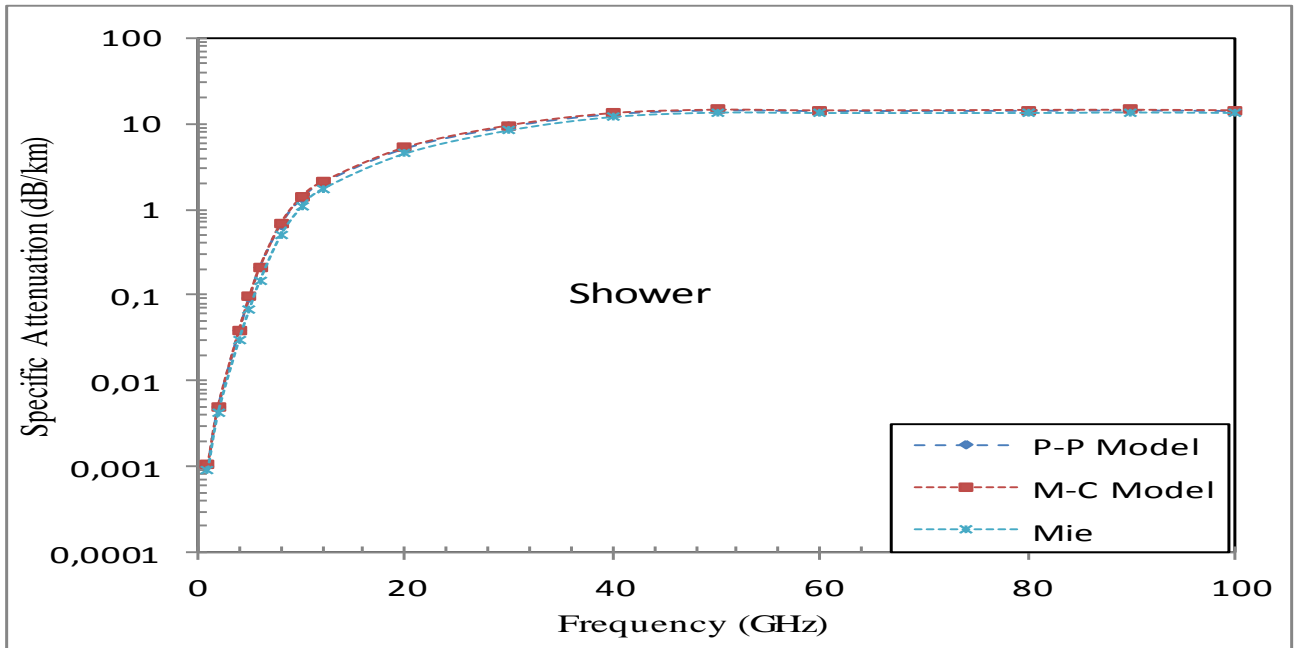
The positive values in the table indicate that the values obtained using the Mie model are less than those of its counterparts. Table 5.3 clearly indicates that the difference between the values obtained using the Mie model and its counterparts increase with increasing rain rate.



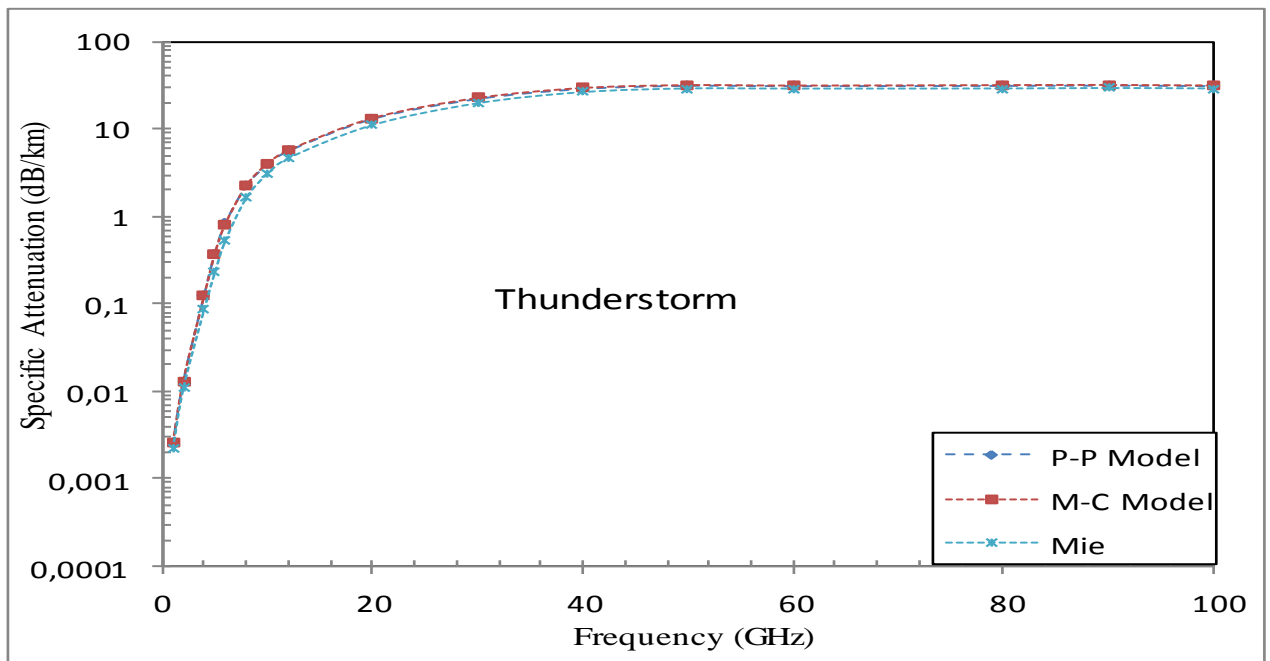
(a) Drizzle



(b) Widespread



(c) Shower



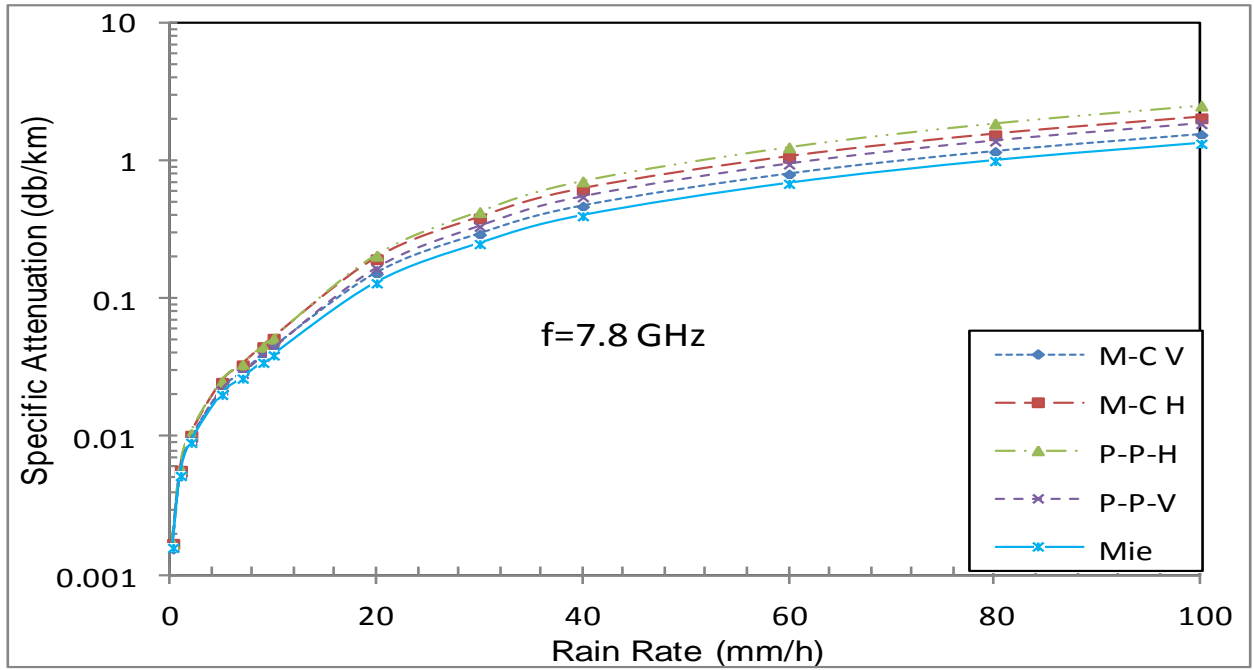
(d) Thunderstorm

Figure 5.3: Specific attenuation due to rain versus frequency for different rain types: (a) Drizzle; (b) Widespread; (c) Shower; and (d) Thunderstorm

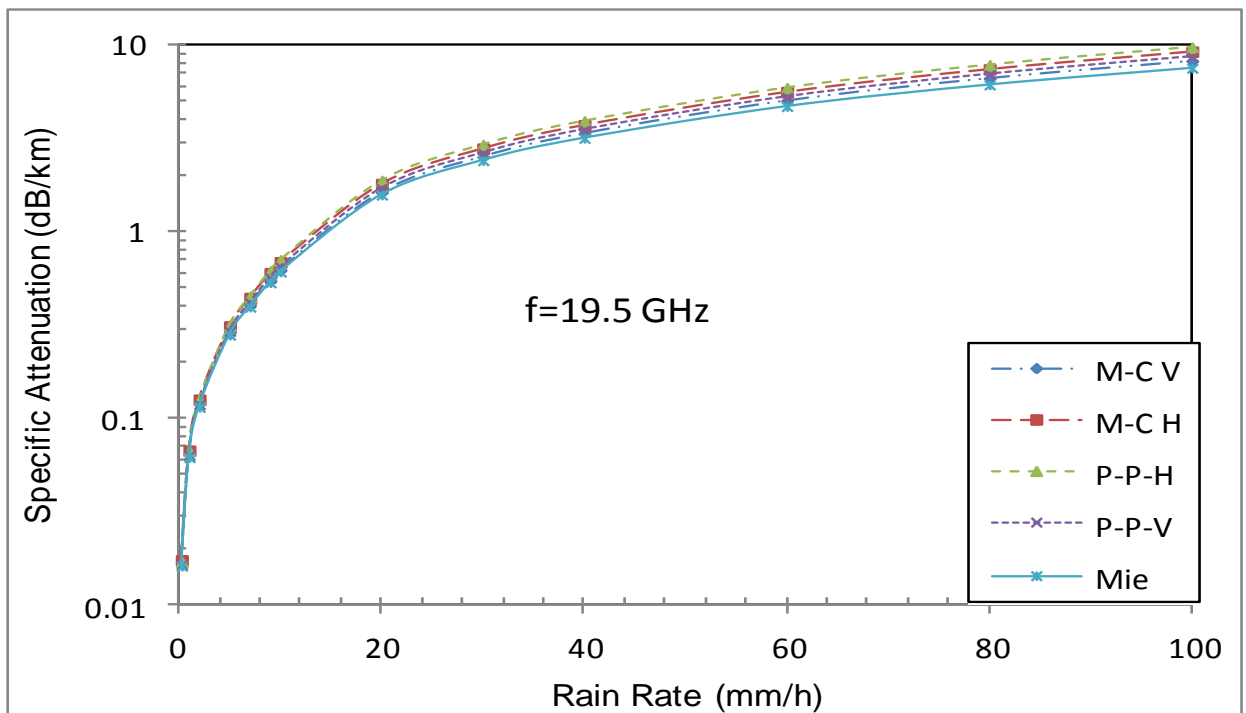
The specific attenuation due to rain varies considerably with operating frequency. Figures 5.4(a) to 5.4(d) show how the specific rain attenuation varies with rain rate for the three models. For both the M-C and the P-P models, the plotted graphs are presented for both vertical and horizontal polarizations. The effect of raindrop distortion is investigated once more and compared with the spherical model of Mie. The results presented in Table 5.4 represent the average percentage differences in specific attenuation between the Mie model and its two counterparts for several frequencies in the range $1 \leq f \leq 245.5$ GHz. It is seen from Table 5.4 that the percentage difference of specific attenuation decreases with increasing frequency. The highest percentage difference of 35.90% is obtained between the Mie model and the P-P model, while a difference of 28.85% is obtained between the Mie model and the M-C model at 7.8 GHz. On the other hand, the lowest percentage difference is observed at a frequency of 140 GHz, with values of 0.81% and 1.04 % for the M-C model (vertical polarization) and the P-P model (vertical polarization), respectively. All the values in Table 5.4 are determined for an extreme rain rate of 100 mm/hr. This result is more evident in Figure 5.3, where small gaps between the graphs are noticeable at lower frequencies. At high frequencies, the graphs seem to attain close values. This implies that the three models are in reasonably good agreement at high frequencies. The Mie model thus gives a good representation of the drop shape even at high frequencies, while a considerable difference is observed at lower frequencies.

Table 5.4: Comparison of the P-P and M-C models to the Mie model at different frequencies

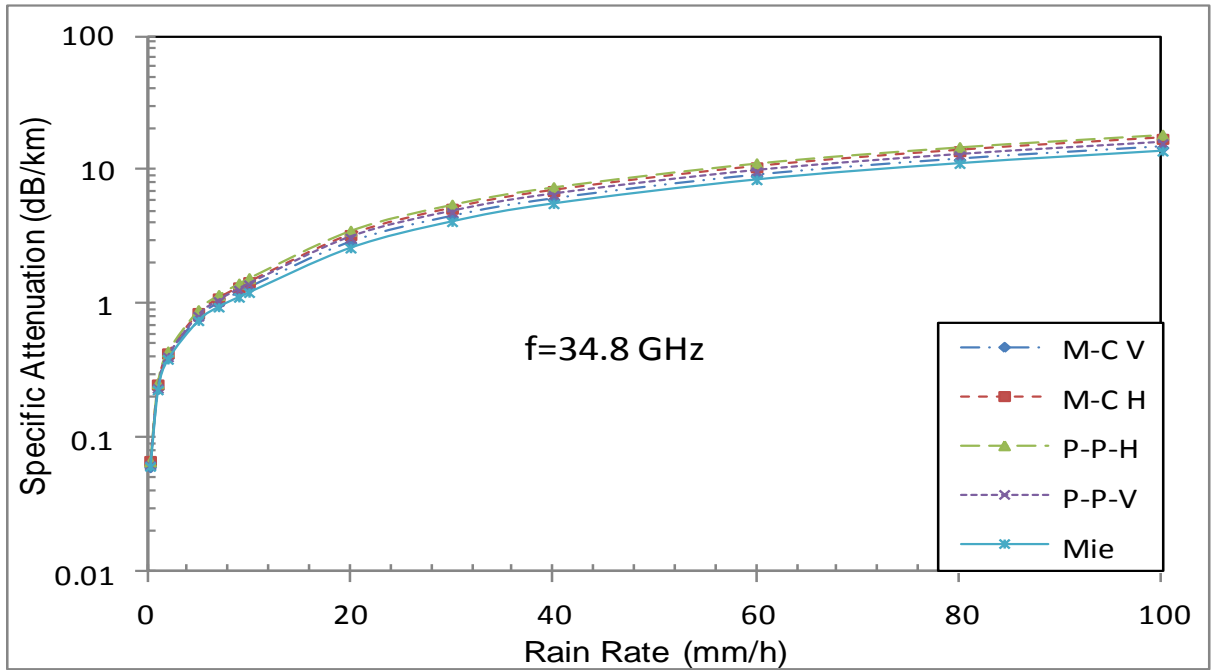
Frequency (GHz)	Average Attenuation Percentage difference (%)			
	P-P V Model	P-P H Model	M-C V Model	M-C H Model
7.8	17.36	35.90	10.20	28.85
13.6	9.19	18.00	10.25	19.04
19.5	7.26	15.80	4.79	13.32
34.8	10.99	22.59	5.67	17.25
140	1.04	10.47	0.81	8.46
245.5	2.47	13.55	1.71	9.18



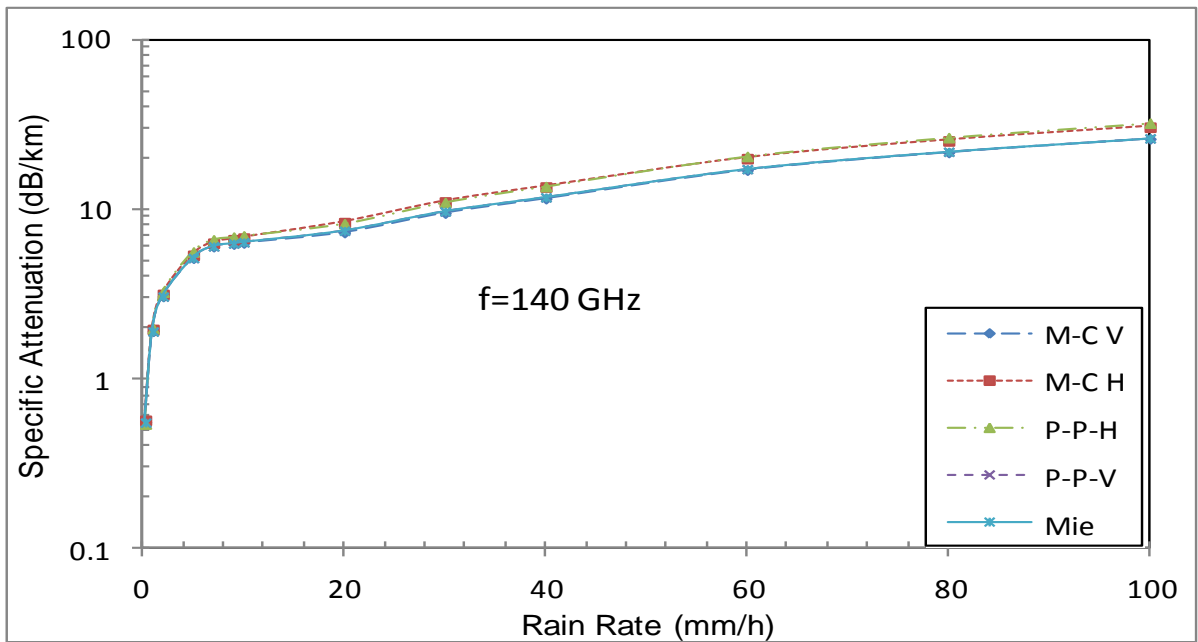
(a) 7.8 GHz



(b) 19.5



(c) 34.8 GHz



(d) 140 GHz

Figure 5.4: Specific rain attenuation against rain-rate for (a) 7.8 GHz (b) 19.5 GHz (c) 34.8 GHz and (d) 140 GHz

5.9 The Olsen Model for Specific Rain Attenuation

The ITU-R recommends the use of the power law relationship to determine the specific attenuation due to rain, provided the local rain rate is known. In this chapter, the results of specific rain attenuation obtained using the Lognormal DSD are modelled using the power law relationship. As mentioned earlier on, the coefficients k and α vary with both frequency and location-dependent rain drop size distribution. These coefficients are determined and presented in Table 5.5 for Durban, which lies on the east coast of South Africa. In this section circular polarization is assumed. Once again, three raindrop size models are considered, one being the popular spherical drop shape of Mie, while the other two take into account distortion during the drop fall. The power law model parameters are presented in Table 5.5 with subscripts m , p , and s representing Mie, P-P, and M-C models respectively.

Figure 5.6 shows the parameter α modelled for the frequency range $0 < f \leq 100$ GHz. The results in Tables 5.6 and 5.7 can be used to determine the power law coefficients at any desired frequency in the range $1 \leq f \leq 100$ GHz. The specific rain attenuation can thus be determined at all frequencies in this range of desired rain rates.

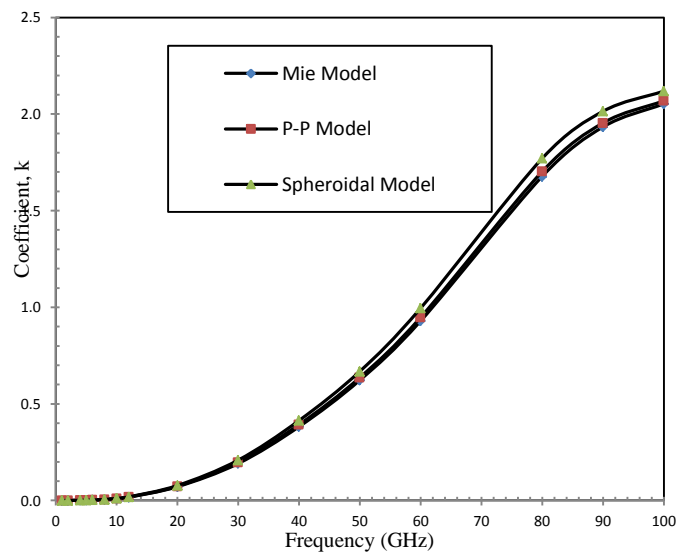


Figure 5.5: Coefficient k against frequency (Note: the Spheroidal model is the M-C model)

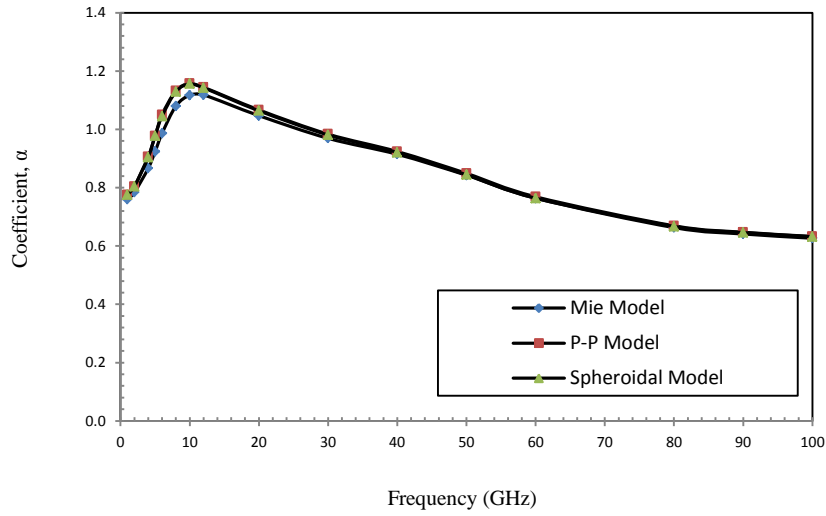


Figure 5.6: Coefficient α against frequency (Note: the Spheroidal model is the M-C model)

The following general model is realized:

$$k = A_1 f^4 + B_1 f^3 + C_1 f^2 + D_1 f + E_1 \quad (5.16)$$

$$\alpha = A_2 f^4 + B_2 f^3 + C_2 f^2 + D_2 f + E_2 \quad (5.17)$$

where A_1 and A_2 represent the fourth coefficient of the polynomial, B_1 and B_2 represent the third coefficient, C_1 and C_2 represent the second coefficient, D_1 and D_2 represent the first coefficient, and E_1 and E_2 represent the constant of the polynomial. Substituting the coefficients shown in Table 5.6 and 5.7 into Equations (5.16) and (5.17) enables the determination of k and α for different frequencies.

Table 5.5: Power law model parameters for the three drop-size models

Frequency (GHz)	Mie Model		P-P Model		M-C Model	
	k_m	α_m	k_p	α_p	k_s	α_s
1	0.00006	0.7595	0.00006	0.7759	0.00006	0.7758
2	0.0002	0.7836	0.0002	0.8043	0.0002	0.8040
4	0.001	0.8663	0.001	0.9064	0.001	0.9039
5	0.0016	0.9239	0.0016	0.9776	0.0017	0.9779
6	0.0025	0.9859	0.0025	1.0500	0.0026	1.0448
8	0.0052	1.0797	0.0053	1.1319	0.0056	1.1291
10	0.0099	1.1168	0.0103	1.1574	0.0109	1.1562
12	0.0172	1.1180	0.0179	1.1442	0.019	1.1424
20	0.0714	1.0471	0.0736	1.0667	0.0776	1.0636
30	0.1914	0.9692	0.1975	0.9835	0.2088	0.9807
40	0.382	0.9145	0.3928	0.9239	0.4137	0.9208
50	0.6226	0.8427	0.6364	0.8489	0.6682	0.8441
60	0.929	0.7638	0.9477	0.7687	0.9951	0.7637
80	1.6774	0.6631	1.7026	0.6692	1.7705	0.6672
90	1.9331	0.6412	1.954	0.6471	2.014	0.6459
100	2.053	0.6266	2.0686	0.6325	2.1186	0.6319

Table 5.6: Modelled coefficient k

Fit Model		Mie	P-P	M-C
Fourth Order Polynomial $1 \leq f \leq 100$	4 th	-7E-8	-7E-8	-7E8
	3 rd	1E-5	1E-5	1E-5
	2 nd	-1E-4	-1E-4	-1E-4
	1 st	3.3E-3	3.3E-3	3.2E-3
	constant	-0.0114	-0.0115	-0.0113

Table 5.7: Modelled coefficient α

Polynomial Fit		Mie	P-P	M-C
4 th Order Polynomial $1 \leq f \leq 10$ GHz	4th	-	8E-5	8E-5
	3rd	-9E-4	-2.8E-3	-2.7E-3
	2nd	1.43E-2	2.81E-2	2.76E-2
	1st	-1.65E-2	-4.4E-2	-4.28E-2
	constant	0.7638	0.7964	0.7954
3 rd Order Polynomial $10 < f \leq 100$ GHz	3rd	5E-7	4E-7	4E-7
	2nd	-4E-5	-3E-5	-2E-5
	1st	-6.3E-3	-7.6E-3	-7.7E-3
	constant	1.1923	1.232	1.232

5.10 Chapter Summary and Conclusion

This chapter presents realistic raindrops based on their extinction total cross section and the specific attenuation due to rain using three models, namely, the M-C (or spheroidal) model, the P-P model, and the Mie (or spherical) model. The chapter further investigates the validity of the Mie spherical raindrops model that is used by many researchers. It is observed that while the extinction cross-section varies considerably with raindrop size, the three models show a close agreement for small raindrop diameters but differ as the drop size increases.

The Mie model thus remains accurate for fade margin determination for small raindrop diameters; this model therefore gives reliable specific rain attenuation predictions in regions dominated by drizzle rainfall, but will considerably underestimate the attenuation in regions dominated by shower and thunderstorm rain types.

The results also show that the raindrop extinction cross section for the three models agree at the lower frequencies while as the frequency increases, a noticeable difference is observed. The effect of polarization is noticed in the M-C model and the P-P model, with the horizontal polarization returning the higher percentage difference compared to the Mie model.

The specific attenuation due to rain for different total cross-sections (P-P, M-C and Mie models) with circular polarization for different rain types shows a progressive increase in the average percentage differences (with respect to the Mie model) from drizzle through widespread to thunderstorm. The average specific attenuation percentage difference for the P-P model is low compared to the M-C model. The results further show that the power law model parameters, k and α , can be modelled using the fourth order polynomial as shown by Equations (5.16) and (5.17). The specific rain attenuation can thus be determined using the power law model for frequencies up to 100 GHz and rain rate up to 100 mm/h. In regions where there is a high presence of large raindrops (as is the case in tropical and sub-tropical regions like South Africa), it will be inadequate to employ the Mie model in the determination of local rain fade margins. However, this model is acceptable for regions dominated by the drizzle rain type due to the large number of small drops.

Chapter 6

Specific Attenuation and Phase Shift due to Rain

6.0 Introduction

As the communication services increase in Southern Africa, the congestion at lower frequency bands has forced service providers to employ higher frequencies such as the millimeter wave band. In view of this, a finer model is required to estimate the militating factors that cause impairments in the transmitted signals at this frequency band. This chapter focuses on the calculation of specific attenuation and phase shift due to depolarization effects of rain at frequencies between 1 and 100 GHz using oblate spheroidal raindrop model for the region. The scattering characteristics at four different rain types are integrated to compute the specific attenuation and specific phase shift due to rain. The applicability of the results derived from this study is confirmed through comparison with results of specific attenuation and phase shift obtained by using the ITU-R standard and other well-known models for tropical and sub-tropical regions.

The demands due to emerging technologies has forced communications service providers and researchers to explore the higher frequency bands where some of the advantages are frequency reuse, device miniaturization, and huge bandwidth. At the frequency bands above 7 GHz for tropical regions and above 10 GHz for temperate regions rain attenuation is a dominant contributor to the signal impairments. However, as the transmitted signal wavelength approaches the size of the raindrops, then the interaction between the transmitted signals and raindrops results in the degradation of the communication link through signal absorption and scattering due to displacement currents in the rain drops and the raindrops' high dielectric constants at high frequencies [1]. To determine the magnitude of signal degradation, i.e., signal attenuation, rain-induced signal depolarization, etc, the detailed scattering process and microphysical properties of raindrops must be known.

Raindrop scattering properties and its attenuation of radio waves have attracted many scholars' contributions, especially in temperate and tropical regions of the globe [121]. In temperate regions, just to name but a few, the contribution by Crane [122], Olsen [123], Oguchi [124 –126] and Medhurst [127] gave an in-depth knowledge in the field of radio propagation in a rainy medium and further comparative studies in the tropical regions. In the tropical regions, the contribution of few authors such as Ajayi and Ofoche [14], and Ajewole et al. [128] in West-Africa and also the contribution by Kunhikrishnan et al., [129] in India have detailed comparative studies of rain attenuation distributions for different regions in the globe. In Southern Africa too, studies have been initiated in this important area of radio propagation, see for example [130-132].

6.1 The physics of the rain structure

The refractivity of raindrops largely depends on their temperature and the frequency of the radio signal propagating through it. In calculating the scattering properties of raindrops, it is imperative to know the complex refractive index, given by [133]:

$$N = N_r + jN_i \quad (6.1)$$

where $j = \sqrt{-1}$. The complex permittivity is related to the complex refractive index by $N = \sqrt{\varepsilon(r)}$. where the complex permittivity of water is given by [133]:

$$\varepsilon(r) = \varepsilon'(r) + j\varepsilon''(r) \quad (6.2)$$

The complex permittivity, also referred to as the dielectric constant, of water is also a function of temperature. A model for calculating the temperature-dependent complex permittivity of water across the frequency range 1 GHz to 1000 GHz that uses a double-Debye relaxation approximation is given in [133]. This model is based on non-linear, multi-parameter, least-squares fitting of experimental data to the dielectric properties of water. The real and the imaginary parts of the complex permittivity in (6.2) are given by [133]:

$$\varepsilon' = \varepsilon_2 + \frac{\varepsilon_0 - \varepsilon_1}{1 + (f/f_D)^2} + \frac{\varepsilon_1 - \varepsilon_2}{1 + (f/f_s)^2} \quad (6.3)$$

$$\varepsilon'' = \frac{f(\varepsilon_0 - \varepsilon_1)}{f_D[1 + (f/f_D)^2]} + \frac{f(\varepsilon_1 - \varepsilon_2)}{f_s[1 + (f/f_s)^2]} \quad (6.4)$$

where: f is the frequency in GHz, ε' = real part of the complex permittivity, ε'' = imaginary part of the complex permittivity, and

$$\varepsilon_0 = 77.6 + 103.3(\theta - 1) \quad (6.5a)$$

$$\varepsilon_1 = 5.48 ; \varepsilon_2 = 3.51 \quad (6.5b)$$

$$f_D = 20.09 - 142(\theta - 1) + 294(\theta - 1)^2 \text{ GHz} \quad (6.5c)$$

$$f_s = 590 - 1500(\theta - 1) \text{ GHz} \quad (6.5d)$$

$$\theta = 300/T ; T = \text{temperature, K} \quad (6.5e)$$

(6.3) and (6.4) are valid for frequencies up to 1000 GHz and temperatures between 10°C and 30°C. The real part is responsible for the change of phase of the radiowave passing through it and the imaginary part is responsible for the signal absorption.

As shown in Figure 6.1, the real part of the complex refractive index of water decreases with increasing frequency whilst the imaginary part attains its maxima in the frequency range between 15 GHz and 30 GHz for the different temperatures, that is, at 0 °C the peak is at 15 GHz, at 10 °C the peak is at 20 GHz, and at 20 °C the peak occurs at 30 GHz.

The dielectric properties of water for millimetric radio wave signals are governed by resonance absorption in water that occurs at particular frequencies. The frequency at which this absorption occurs primarily varies with temperature as the effect of impurities that may be present in rain water becomes negligible for microwave and millimetric radio signals.

Apart from the refractivity, the shape of raindrops, which is a function of surface tension and aerodynamic forces as the drops fall onto the ground, also contributes to signal attenuation due to rain. It has been shown [130] that the shape of falling raindrops depends on the rain drop size, with small rain drops having spherical shapes while larger rain drops are spheroidal in shape. It should be noted that in this work the model of oblate spheroidally shaped raindrops at 20 °C temperature is adopted.

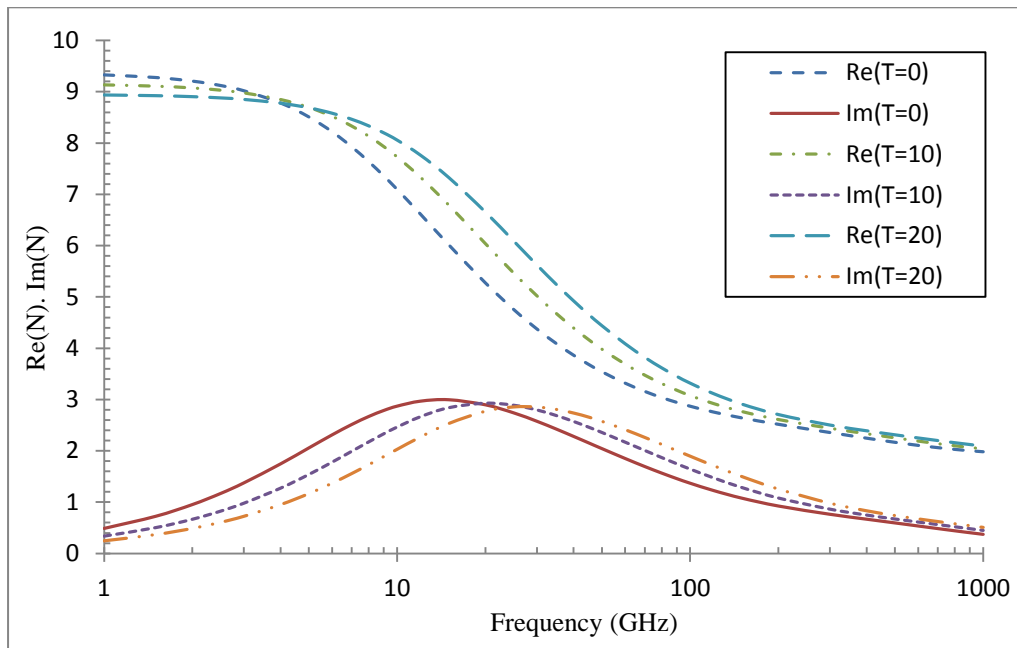


Figure 6.1: Characteristics for the complex refractive index of water at 3 different temperatures

6.2 Method of moments and the three-parameter Lognormal Distribution

In estimating the specific rain attenuation and phase shift, a reliable model of raindrop size is required. In this section, the method of moments is suggested to estimate the three parameters of the lognormal raindrop size distribution. The reader is referred to Sections 4.5, 5.2, 5.6, and 5.8 for the procedure employed in data collection, modelling of the DSD for oblate spheroidal rain drops, the mathematics of the said rain drops, the MoM technique and the Lognormal distribution, and specific rain attenuation and the Pruppacher-Pitter Theory on Oblate Spheroidal is used in this chapter.

Figure 6.2 shows drop size distribution patterns for various rain types. At the drop diameter less than 1 mm, the patterns are similar at different rain rates whereas above 1 mm, the divergence of distribution is well noticed and further as the rain rate increases.

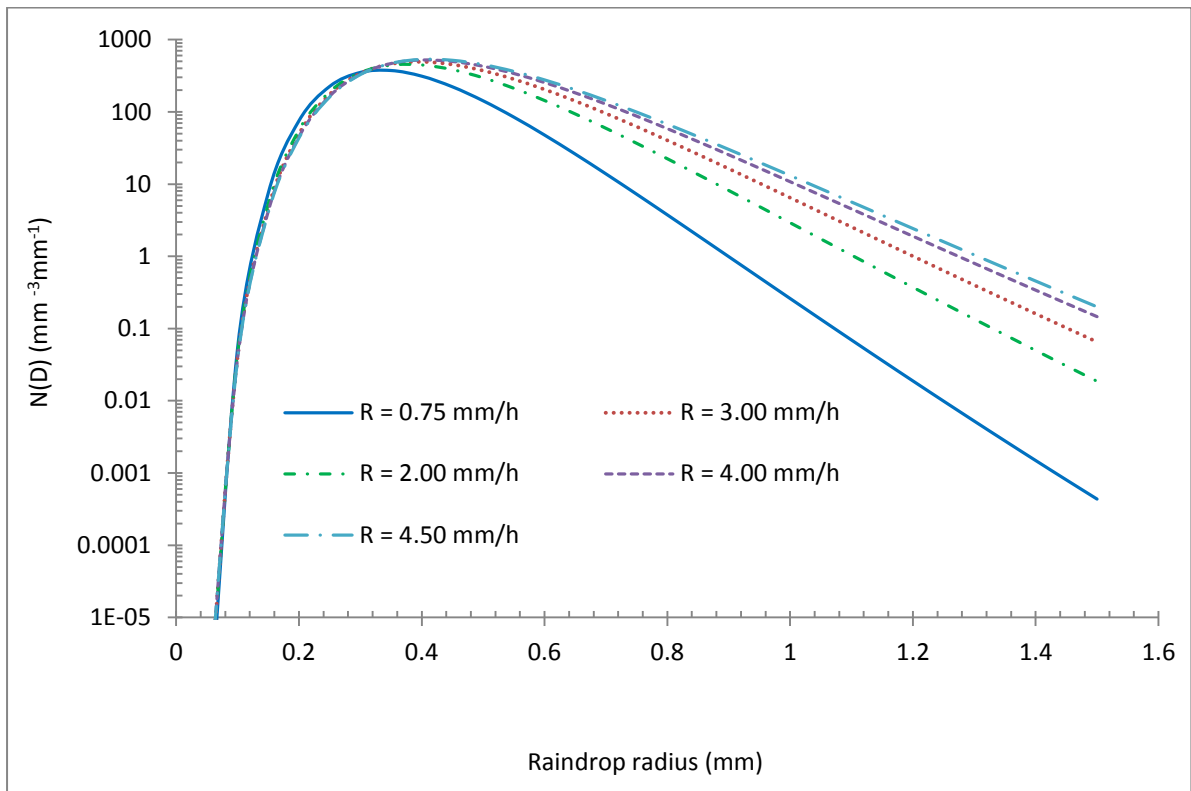
6.3 Specific Rain Attenuation and Phase Shift: Pruppacher-Pitter Theory

The specific phase shift at a given frequency is represented with the imaginary part of the complex forward scattering amplitude $S(0)$ and expressed as [112]:

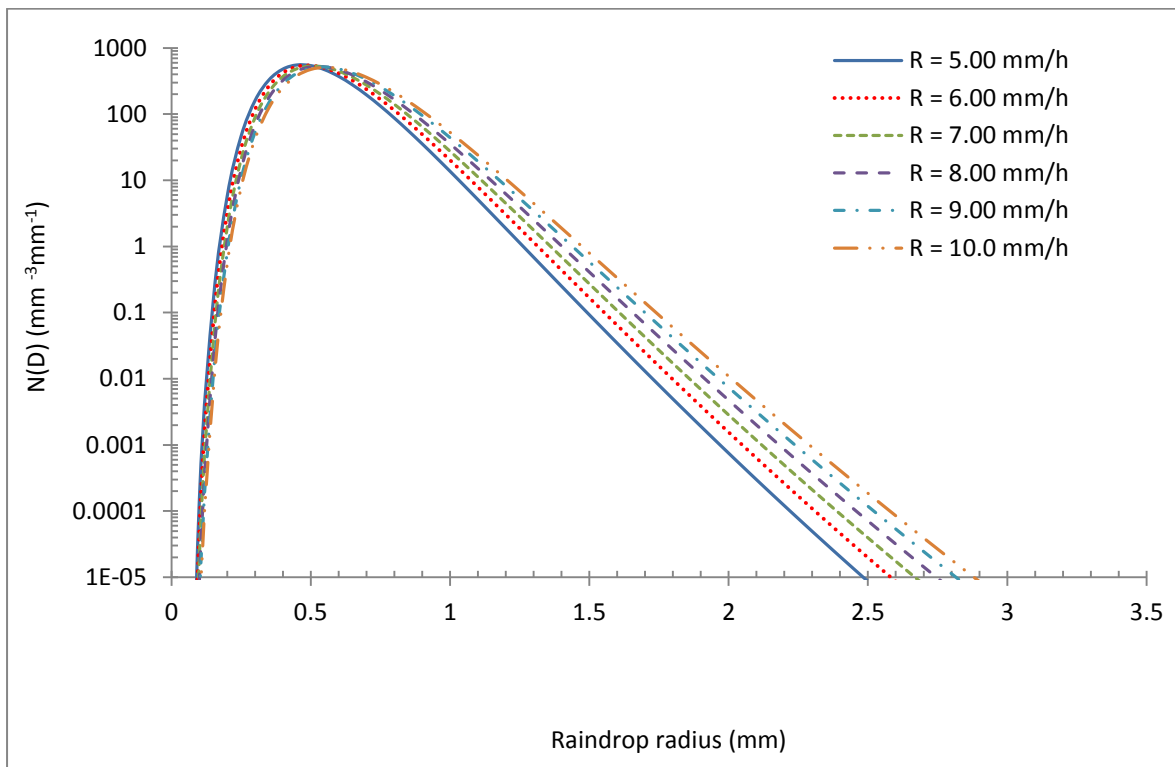
$$\Phi = 9.0 \times 10^4 \frac{\lambda^2}{\pi^2} \text{Im} \sum_{n=1}^{\infty} (2n+1)(a_n + b_n) N(D) dD \quad (dB/km) \quad (6.6)$$

where a_n and b_n are the raindrops' minor and major semi-axes, respectively, and $N(D)$ is the mean raindrop size distribution.

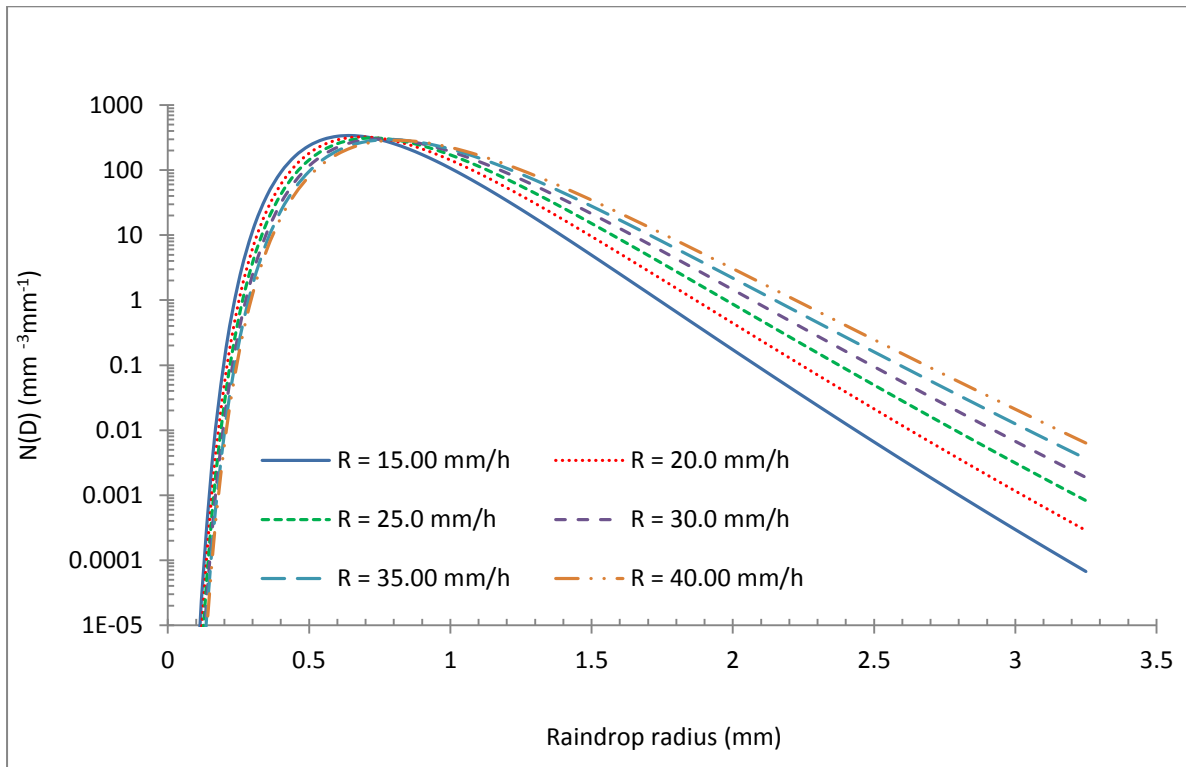
The specific rain attenuation due to different rain classes in South Africa has been evaluated in the frequency range 1 – 100 GHz, for a path length of 1 km, drops' temperature of 20 °C and the oblate spheroidal raindrop shape considered. Figure 6.3 shows values of specific rain attenuation at recommended specifications for different rain types: drizzle, widespread, shower and thunderstorm. In general, specific rain attenuation increases with increase in frequency and also rain rate for all types of rain. At 100 GHz it decreases in rate and tending to attain a bit of stability as the frequency further increases irrespective of rain type, this might be due to the saturation state of the total cross section and scattering cross section of scattering parameters or properties employed at the higher frequencies. The same trend of distribution pattern is recorded for a specific phase shift as presented in Figure 6.4.



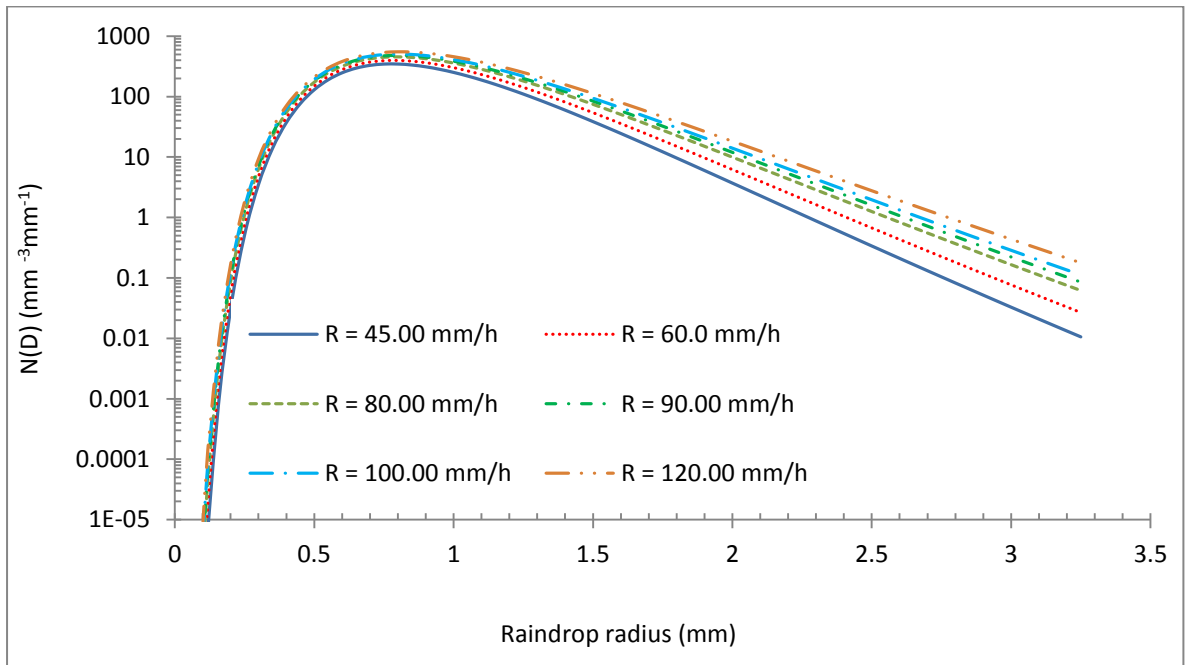
(a)



(b)

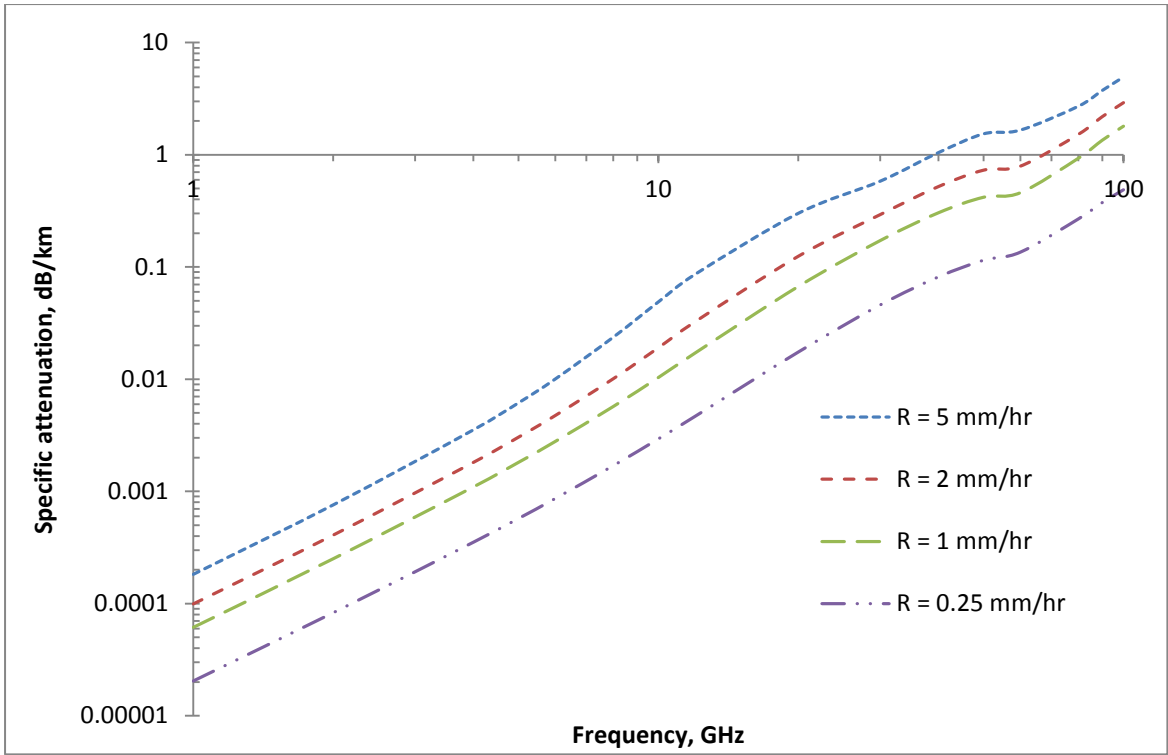


(c)

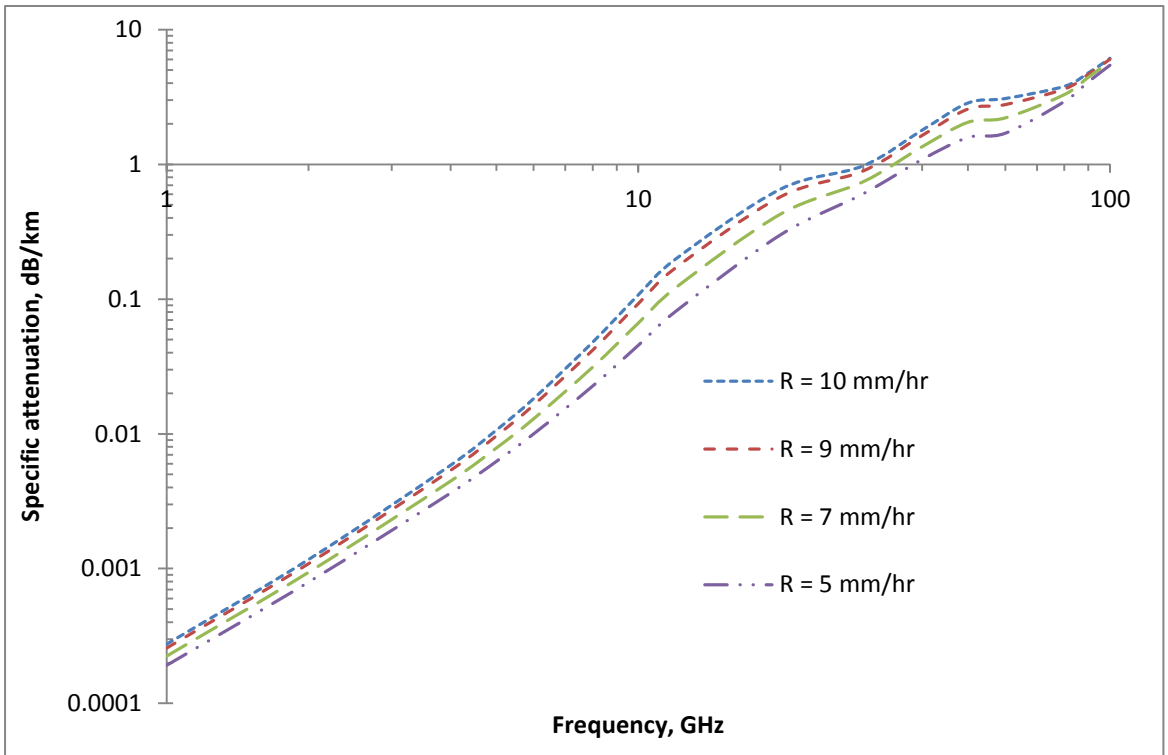


(d)

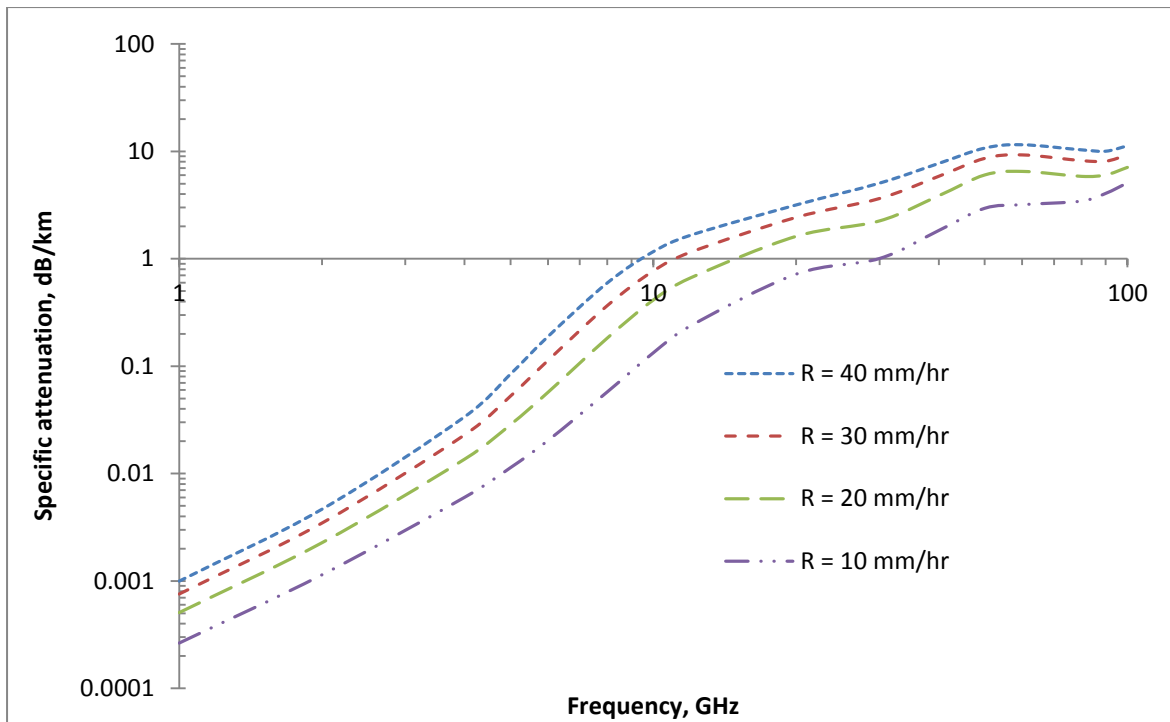
Figure 6.2: Lognormal DSD for: (a) Drizzle (b) Widespread (c) Shower, and (d) Thunderstorm



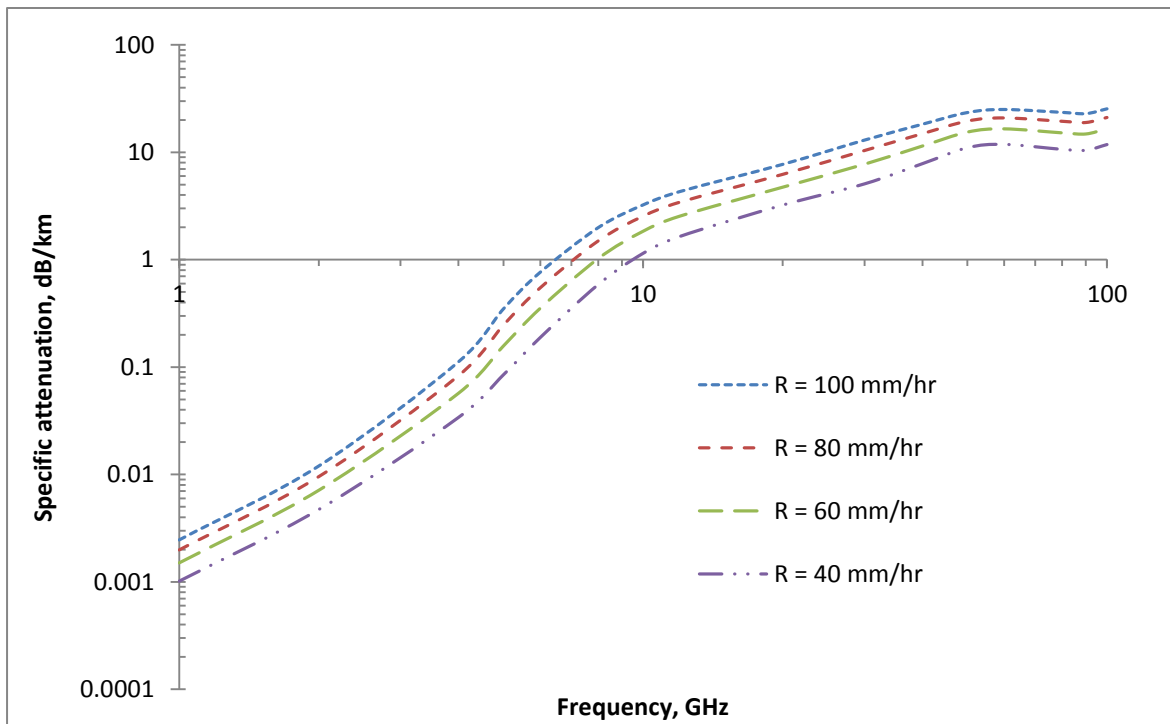
(a)



(b)

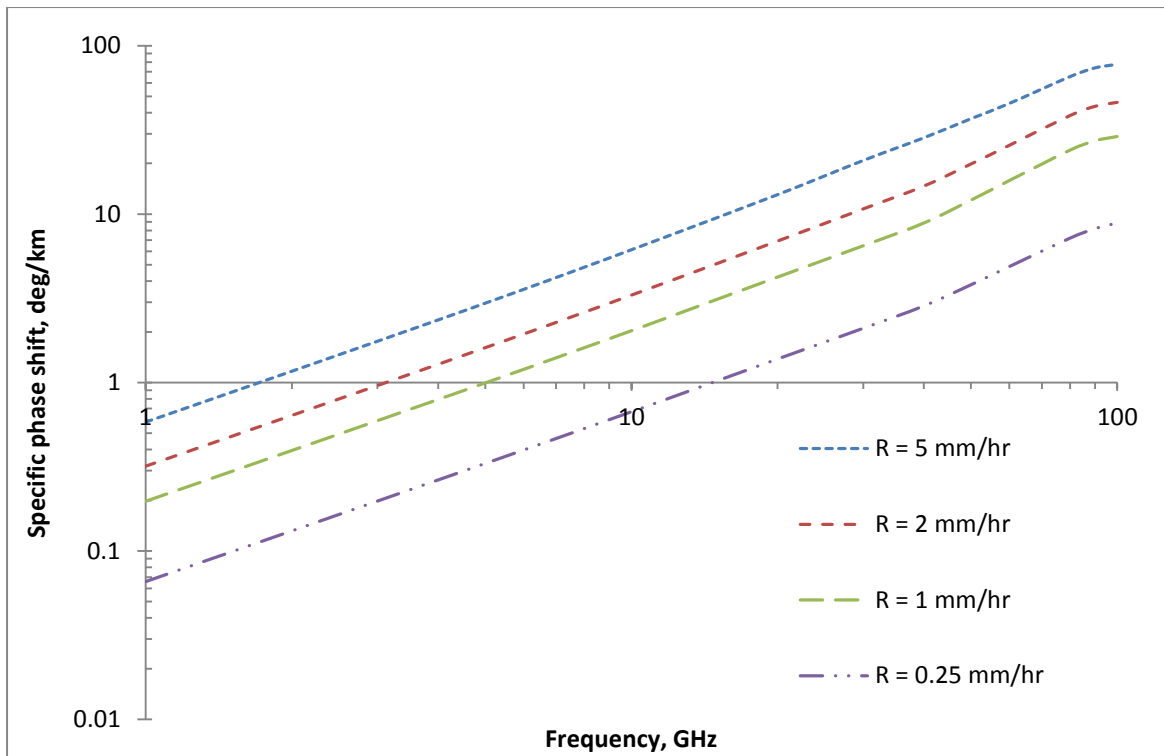


(c)

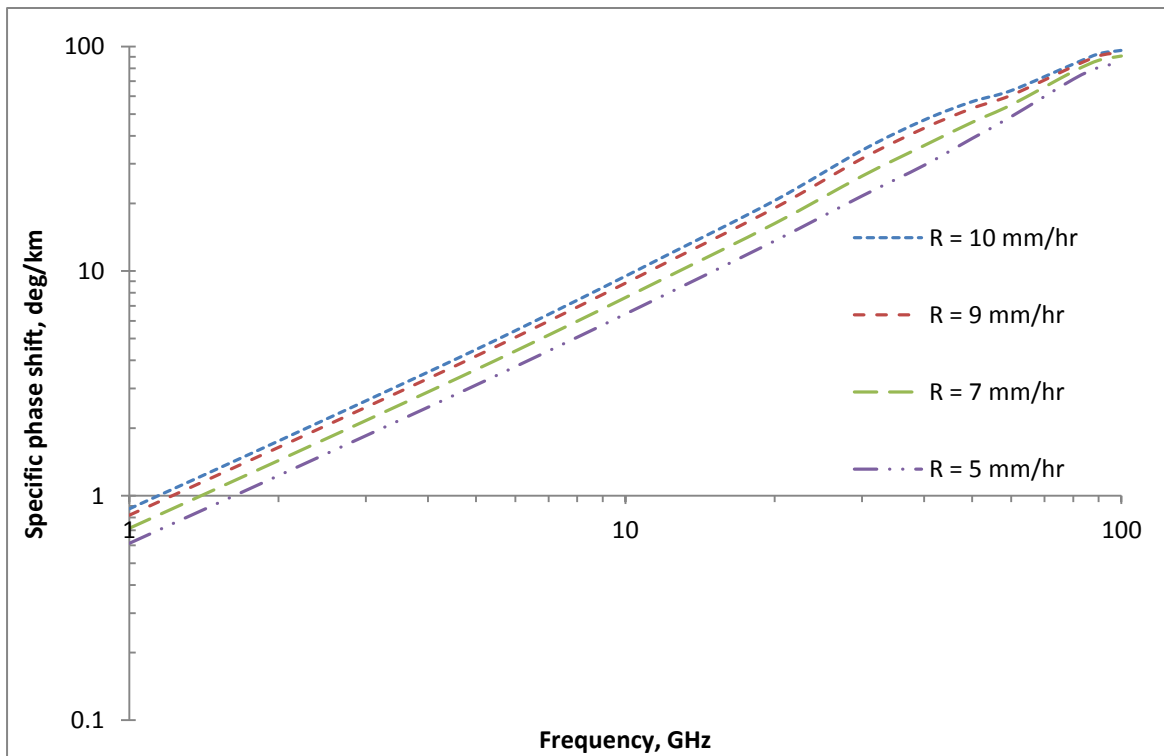


(d)

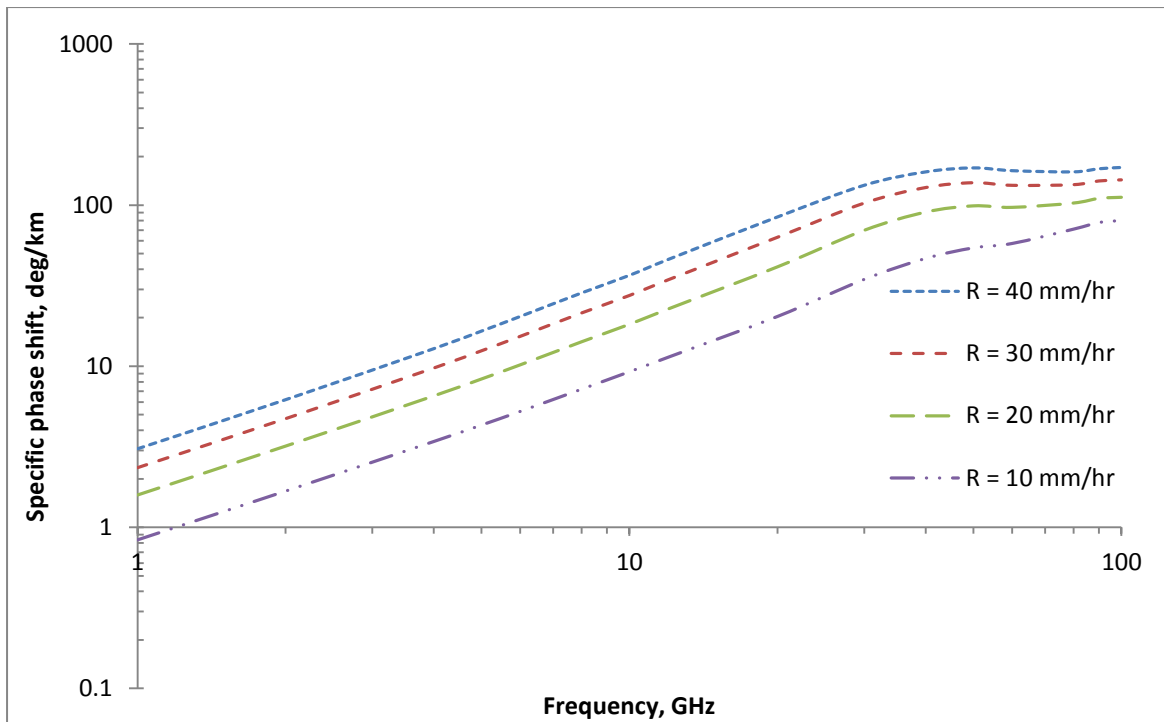
Figure 6.3: Specific Attenuation for: a) Drizzle (b) Widespread (c) Shower (d) Thunderstorm



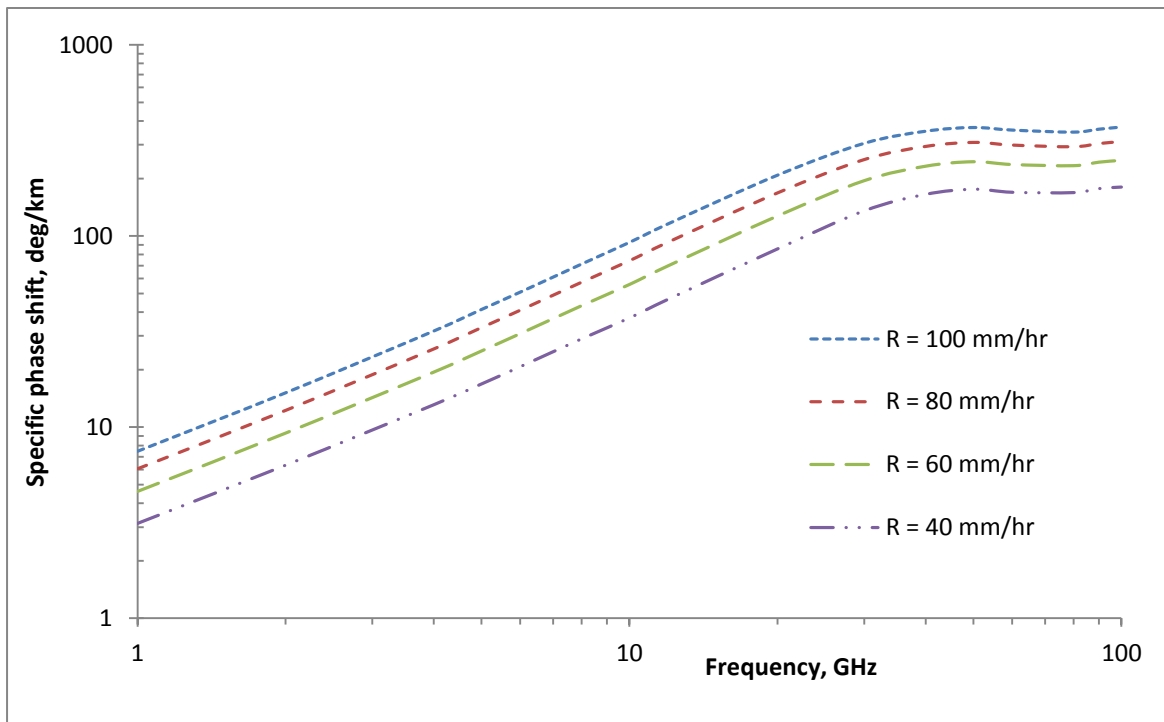
(a)



(b)



(c)



(d)

Figure 6.4: Specific Phase Shift: (a) Drizzle (b) Widespread (c) Shower (d) Thunderstorm

The specific phase shifts due to various sub-tropical rain types of Southern Africa are presented in Figure 6.4 for the frequency range 1 – 100 GHz, for a 1 km path length at a water temperature of 20°C. and oblate spheroidal raindrop shape. The magnitude of the specific phase shift increases rapidly with frequency for drizzle and widespread rain types beyond 100 GHz; for shower and thunderstorm rain types, the phase shift increases with frequency until it reaches a peak approximately around 40 GHz where it stabilizes. As the rain type changes progressively from drizzle to thunderstorm, the specific phase shift decreases and also the more intense the rain rate, the smaller the critical frequency. Simply put, in the thunderstorm rain type, the critical frequency is smallest whereas in the case of drizzle it is the highest.

6.4 Comparative studies of specific attenuation and phase shift with existing models

The models for specific attenuation and specific phase shift derived for the Southern African region, together with the existing models for the Western African region, specifically Nigeria [128], are relatively compared with the ITU-R model for temperate regions which employed the Laws and Parsons DSD [3]. The comparative studies are carried out at rain rates of 0.25 mm/hr, 25 mm/hr, 50 mm/hr and 100 mm/hr which are typical rain type classifications of drizzle, widespread, shower and thunderstorm. In the study, the Southern African and Nigerian models are based on oblate spheroidal raindrop shape while the Laws and Parsons model assumed spherical rain drop shapes. The average percentage difference is used to present the characteristic status (under-estimation or over-estimation) of the proposed models as compared with the accepted ITU-R model.

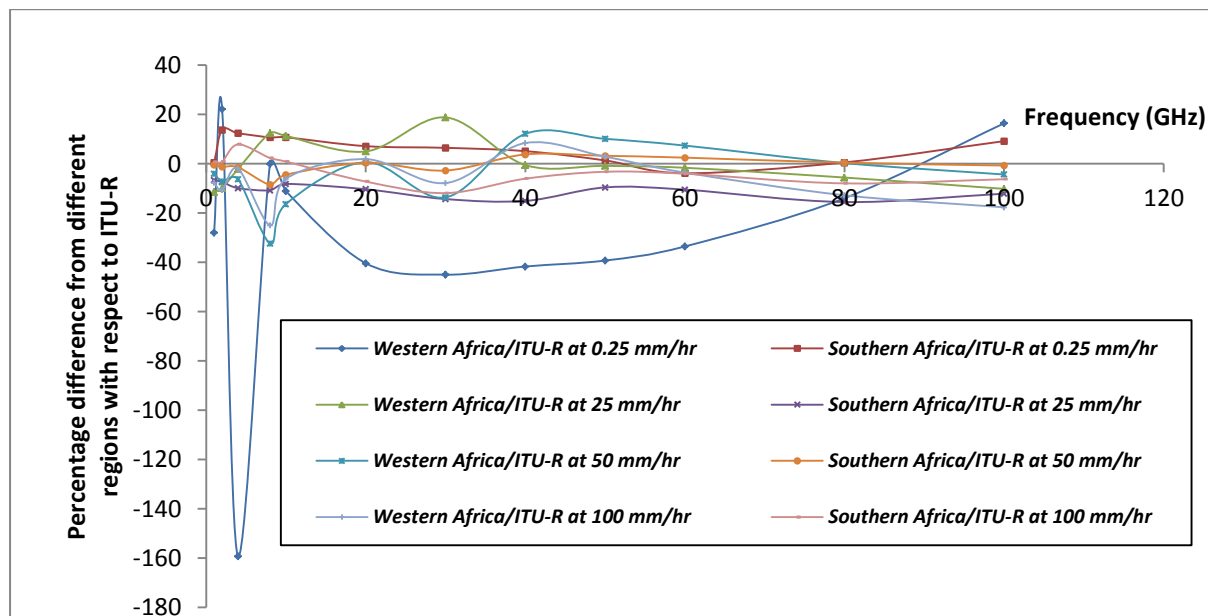


Figure 6.5: Percentage difference in specific attenuation due to rain for different rain rates in different regions with respect to the ITU-R model (Note: The West African Model refers to the Nigerian Model)

Considering Figures 6.5 and 6.6, the parts of the curves below the zero baseline indicate the under-estimation characteristic while those above the baseline indicate the over-estimation of the ITU-R model with respect to the chosen models. In the case of specific attenuation at a rain rate of 0.25 mm/hr (drizzle rain type) Figure 5 indicates that the ITU-R model under-estimates in the West Africa region with an average percentage difference of 31.3% while in the case of Southern Africa there is a 6.19% over-estimation. The minimum percentage of difference recorded for West Africa is -159.3% and its maximum is +16.4%. The minimum percentage of difference for Southern Africa is +0.51% and its maximum is +13.8%.

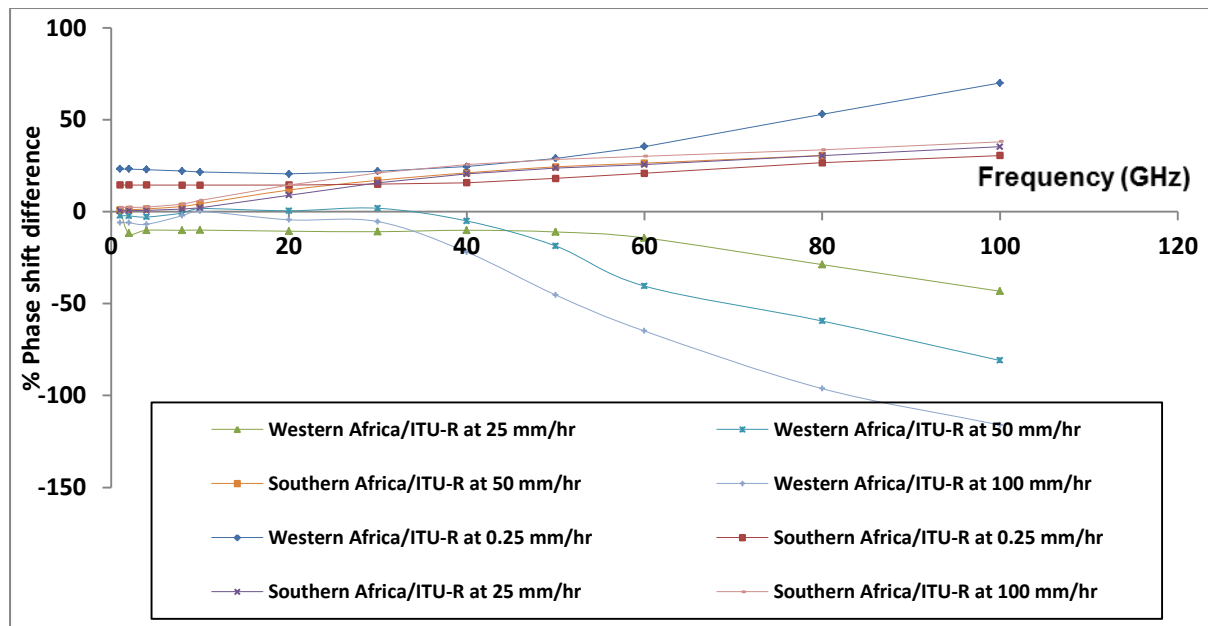


Figure 6.6: Percentage difference in phase shift for different rain rates in different regions with respect to the ITU-R model

In the case of widespread rain type (rain rate of 25 mm/hr), the observed results showed that the average percentage differences in West-Africa and Southern Africa are +0.45% and -10.85%, respectively. This implies that the ITU-R model overestimated specific attenuation in West Africa by 0.45% and underestimated the same phenomenon by 10.85% in Southern Africa.

For the shower rain type (rain rate of 50 mm/hr), the maximum and minimum percentage differences for West Africa are 10.13% and -32.3%, respectively. In the case of Southern Africa, the maximum and minimum percentage difference values are 3.79% and -8.44% respectively. The average percentage difference of specific attenuation due to rain for West Africa and Southern Africa are -4.44% and -0.74%. The average percentage difference shows that both studied regions are underestimated by the ITU-R model.

Lastly on the comparative studies of specific rain attenuation, using the percentage differences for the thunderstorm rain type also confirmed that the ITU-R model underestimated specific attenuation due to rain by -6.66% in West Africa and by -2.83% in the Southern Africa.

Figure 6.6 presents a characteristic percentage differences in the specific phase shift between the West African model and the ITU-R model, and the Southern African model and the ITU-R model. For the drizzle rain type, the average percentage difference for West Africa and Southern Africa are 30.64% and 17.85% respectively. This implies that the ITU-R model used to determine specific phase shift overestimates for the small rain drops for these two regions. In the case of widespread rain (rain rate of 25 mm/hr) the average percentage difference between the West African model and the ITU-R model shows an under-estimation of 14.14% and for the Southern African region there is an over-estimation of 13.84%. The trend of under-estimation by the ITU-R model in the West African region cuts across the shower and thunderstorm rain types by 17.35% and -31.22% respectively, while in the case of Southern Africa, an overestimation trend by 14.83% and 17.40% respectively was observed for the shower and thunderstorm rain types.

6.5 Power Law regression for specific attenuation and phase shift

The results obtained from the computations of specific attenuation and specific phase shift due to rain are modeled using a power law regression scaling at different frequencies and rain types in the region of Southern Africa. Table 6.1 shows the coefficients of power law expressions in Equations (2.17) and (6.7) for specific attenuation and phase shift due to rain for the region respectively.

$$\Phi = \alpha R^\beta \quad (6.7)$$

where α and β are coefficients of the phase shift and R in mm/hr is the rain rate for a defined rain type for the region. With reference to Equation (2.17), Table 6.1 shows that the values of a are less sensitive to the type of rain chosen and the same also applies, to some extent, in the case of parameter b for the frequency range 1 – 7 GHz.

As presented by various authors [45, 134], the analytical expressions of a , b , α and β can be used conveniently by radio planners and system designers to estimate both specific attenuation and phase shift due to rain. Based on Equations (2.17) and (6.7) for Southern Africa and for the different rain types, general equations are summarized in Equations (6.8) to

(6.15) for specific attenuation and Equations (6.16) to (6.23) denote expressions for the specific

Table 6.1: The values of a and b given for the frequency range 1-100 GHz for the Southern African Region

Freq(GHz)	Drizzle			Widespread			Showers			Thunderstorm		
	a	b	R ²									
1	2x10 ⁻⁵	0.9309	0.9738	3x10 ⁻⁵	0.719	0.999	2x10 ⁻⁵	0.8291	0.999	2x10 ⁻⁵	0.8714	1
2	0.0001	0.936	0.9749	0.0001	0.7465	0.9988	8x10 ⁻⁵	0.8671	0.999	7x10 ⁻⁵	0.9161	1
3	0.0002	0.9441	0.9767	0.0003	0.7887	0.9986	0.0002	0.9234	0.9999	0.0001	0.981	1
4	0.0005	0.9549	0.9789	0.0005	0.8421	0.9984	0.0003	0.9938	0.9999	0.0002	1.0643	0.9999
5	0.0008	0.9679	0.9813	0.0007	0.9051	0.9981	0.0004	1.0816	0.9998	0.0003	1.18	0.9999
6	0.0012	0.983	0.9839	0.001	0.9766	0.9979	0.0006	1.1785	0.9998	0.0004	1.2871	0.9999
7	0.0018	1	0.9864	0.0014	1.0503	0.9979	0.0008	1.2556	0.9999	0.0006	1.3351	1
8	0.0025	1.0184	0.9888	0.0019	1.1174	0.9981	0.0011	1.302	0.9999	0.001	1.3392	1
9	0.0035	1.0372	0.9909	0.0025	1.1662	0.9986	0.0017	1.3087	1	0.0017	1.3077	1
10	0.0047	1.0554	0.9925	0.0034	1.1997	0.9991	0.0026	1.2983	1	0.0029	1.2661	1
12	0.0079	1.0835	0.9945	0.006	1.2113	0.9997	0.0055	1.246	1	0.0067	1.1918	0.999
15	0.0152	1.1032	0.9956	0.0127	1.1771	1	0.0143	1.1396	1	0.0177	1.0833	0.999
20	0.0333	1.072	0.9935	0.0287	1.1129	0.9999	0.0302	1.0989	1	0.0377	1.0392	0.9999
25	0.0591	1.0303	0.9897	0.0523	1.0376	0.997	0.0482	1.069	1	0.0568	1.0252	0.9999
30	0.0937	1.0125	0.9876	0.086	0.9894	0.9996	0.0772	1.0296	1	0.0906	0.9871	0.999
35	0.1368	1.004	0.9865	0.1302	0.955	0.9997	0.1196	0.9871	1	0.143	0.9394	0.999
40	0.1872	0.9934	0.9849	0.1849	0.9173	0.9997	0.1709	0.9473	1	0.2053	0.8984	0.9999
45	0.2445	0.9776	0.9825	0.2523	0.8674	0.9996	0.2266	0.907	1	0.2645	0.8659	0.9999
50	0.3094	0.9591	0.9792	0.3373	0.8065	0.9995	0.2889	0.8621	1	0.3176	0.8371	0.9999
60	0.4665	0.9271	0.9723	0.5784	0.6811	0.9994	0.4621	0.7592	1	0.4363	0.7752	1
70	0.6538	0.9086	0.9675	0.9017	0.5896	0.9996	0.7272	0.6632	0.9999	0.6185	0.7072	1
80	0.8273	0.9003	0.9652	1.2113	0.5413	0.9999	1.0107	0.6028	0.9998	0.8267	0.6571	0.9999
90	0.932	0.8967	0.9641	1.4023	0.5202	0.9999	1.196	0.5735	0.9998	0.9659	0.6312	0.9999
100	0.9586	0.8954	0.9638	1.457	0.5122	1	1.2534	0.5625	0.9998	1.0071	0.6215	0.9999

$$a_{Drizzle} = 0.0002f^2 - 0.0017f + 0.0048 \dots\dots\dots 1 \leq f \leq 100GHz \quad (6.8)$$

$$b_{Drizzle} = -1 \times 10^{-4} f^2 + 0.0053f + 0.9651 \dots\dots\dots 1 \leq f \leq 100GHz \quad (6.9)$$

$$a_{Widespread} = 0.0002f^2 - 0.0006f - 0.0124 \dots\dots\dots 1 \leq f \leq 100GHz \quad (6.10)$$

$$\begin{aligned} b_{Widespread} &= 0.0582f + 0.631 \dots\dots\dots 1 \leq f \leq 10GHz \\ b_{Widespread} &= 1.7183f^{-0.2} \dots\dots\dots 11 \leq f \leq 100GHz \end{aligned} \quad (6.11)$$

$$a_{Shower} = 0.0001f^2 - 0.0008f - 0.0072 \dots\dots\dots 1 \leq f \leq 100GHz \quad (6.12)$$

$$b_{Shower} = 0.7616e^{0.0694f} \dots\dots\dots 1 \leq f \leq 8GHz \quad (6.13)$$

$$b_{Widespread} = 1.7795f^{-0.189} \dots\dots\dots 9 \leq f \leq 100GHz$$

$$a_{Thunderstorm} = 2.2889f^{-0.14} \dots\dots\dots 1 \leq f \leq 100GHz \quad (6.14)$$

$$b_{Thunderstorm} = 0.7934e^{0.0766f} \dots\dots\dots 1 \leq f \leq 7GHz \quad (6.15)$$

$$b_{Thunderstorm} = 1.8095f^{-0.193} \dots\dots\dots 8 \leq f \leq 100GHz$$

The expressions in equations (6.8) - (6.15) are fitted by the regression equations optimized by the minimum correlation coefficients R^2 with the values closer to 1. The weak value of R^2 are observed with the expression for b especially in widespread and shower rain types with a value that is less than 0.8.

The same regression technique employed in estimating the coefficients of a and b in the case of specific attenuation is used in determining the coefficients of α and β for the specific phase shift as presented in Table 6.2 for four rain types in the Southern African region.

The results tabulated in Table 6.1 and 6.2 add value in link design in that engineers will be able to determine both specific attenuation and specific phase shift due to rain for the frequency range 1 – 100 GHz. On the other hand, Equations (6.8) – (6.23) are easy-to-use analytical expressions that can present any error that might arise in the case of interpolation of a given frequency to determine unspecified frequencies and their coefficients.

In some cases the analytical expressions are split into two different expressions based on the optimum peaks in order to improve the regression results and correlation coefficients.

$$\alpha_{Drizzle} = 0.0753f^{1.0402} \dots\dots\dots 1 \leq f \leq 70GHz \quad (6.16)$$

$$\alpha_{Drizzle} = 90.624f^{-0.623} \dots\dots\dots 80 \leq f \leq 100GHz$$

$$\beta_{Drizzle} = -4 \times 10^{-6} f^2 + 0.0006f + 0.9278 \dots\dots\dots 1 \leq f \leq 30GHz \quad (6.17)$$

$$\beta_{Drizzle} = 7 \times 10^{-6} f^2 - 0.0016f + 0.9756 \dots\dots\dots 35 \leq f \leq 100GHz$$

$$\alpha_{Widespread} = 0.0823f^{1.0805} \dots\dots\dots 1 \leq f \leq 70GHz \quad (6.18)$$

$$\alpha_{Widespread} = 154f^{-0.641} \dots\dots\dots 80 \leq f \leq 100GHz$$

$$\beta_{Widespread} = -8 \times 10^{-5} f^2 + 0.0041f + 0.7024 \dots\dots\dots 1 \leq f \leq 30GHz \quad (6.19)$$

$$\beta_{Widespread} = 4 \times 10^{-5} f^2 - 0.0083f + 0.9408 \dots\dots\dots 35 \leq f \leq 100GHz$$

$$\alpha_{Shower} = 0.0563 f^{1.1234} \dots\dots\dots 1 \leq f \leq 70GHz \quad (6.20)$$

$$\alpha_{Shower} = 153.06 f^{-0.662} \dots\dots\dots 80 \leq f \leq 100GHz$$

$$\beta_{Shower} = -0.0002 f^2 + 0.0064 f + 0.805 \dots\dots\dots 1 \leq f \leq 30GHz \quad (6.21)$$

$$\beta_{Shower} = 4 \times 10^{-5} f^2 - 0.0095 f + 1.0513 \dots\dots\dots 35 \leq f \leq 100GHz$$

$$\alpha_{Thunderstorm} = 0.0475 f^{1.1414} \dots\dots\dots 1 \leq f \leq 70GHz \quad (6.22)$$

$$\alpha_{Thunderstorm} = 131.56 f^{-0.672} \dots\dots\dots 80 \leq f \leq 100GHz$$

$$\beta_{Thunderstorm} = -0.0003 f^2 + 0.0075 f + 0.8437 \dots\dots\dots 1 \leq f \leq 30GHz \quad (6.23)$$

$$\beta_{Thunderstorm} = 3 \times 10^{-5} f^2 - 0.0075 f + 1.001 \dots\dots\dots 35 \leq f \leq 100GHz$$

Table 6.2: The values of α and β give for frequencies range 1-1000GHz for Southern Africa Region

Frequency(GHz)	Drizzle			Widespread			Showers			Thunderstorm		
	α	β	R^2	α	β	R^2	α	β	R^2	α	β	R^2
1	0.078	0.929	0.973	0.093	0.709	0.999	0.069	0.816	0.999	0.059	0.855	1
2	0.157	0.929	0.973	0.187	0.71	0.999	0.137	0.817	0.999	0.119	0.857	1
3	0.237	0.929	0.973	0.281	0.712	0.999	0.206	0.82	0.999	0.177	0.861	1
4	0.317	0.93	0.973	0.374	0.715	0.999	0.273	0.824	0.999	0.234	0.866	1
5	0.397	0.93	0.973	0.467	0.719	0.999	0.34	0.83	0.999	0.289	0.873	1
6	0.479	0.931	0.974	0.56	0.723	0.998	0.405	0.836	0.999	0.344	0.88	1
7	0.561	0.932	0.974	0.653	0.728	0.998	0.47	0.842	0.999	0.4	0.886	1
8	0.645	0.933	0.974	0.746	0.733	0.998	0.538	0.846	0.999	0.462	0.887	1
9	0.729	0.934	0.974	0.839	0.737	0.998	0.605	0.85	0.999	0.521	0.891	1
10	0.815	0.935	0.974	0.936	0.739	0.998	0.677	0.852	0.999	0.583	0.892	1
12	0.988	0.936	0.975	1.133	0.742	0.999	0.829	0.851	0.999	0.723	0.888	1
15	1.251	0.935	0.974	1.427	0.743	0.998	1.015	0.862	0.999	0.875	0.902	1
20	1.702	0.937	0.975	1.935	0.749	0.998	1.418	0.857	0.999	1.281	0.885	1
25	2.16	0.943	0.976	2.433	0.764	0.999	1.9	0.85	1	1.865	0.856	1
30	2.599	0.943	0.976	2.966	0.756	0.999	2.406	0.829	1	2.451	0.825	1
35	3.008	0.938	0.975	3.529	0.732	0.999	2.904	0.801	1	2.96	0.796	1
40	3.458	0.928	0.973	4.247	0.69	0.999	3.468	0.761	1	3.394	0.767	1
45	4	0.916	0.97	5.225	0.635	0.999	4.225	0.708	0.999	3.863	0.733	1
50	4.547	0.907	0.967	6.296	0.585	0.999	5.12	0.656	0.999	4.395	0.698	1
60	5.538	0.896	0.964	8.295	0.522	0.999	7.05	0.577	0.999	5.718	0.634	0.999
70	6.116	0.892	0.963	9.44	0.5	1	8.325	0.541	0.999	6.801	0.596	0.999
80	6.063	0.892	0.963	9.404	0.496	1	8.385	0.534	0.999	6.906	0.586	0.999
90	5.539	0.892	0.963	8.57	0.498	1	7.667	0.535	0.999	6.387	0.584	0.999
100	4.943	0.892	0.963	7.587	0.504	1	6.704	0.545	0.999	5.552	0.596	0.999

6.6 Chapter Summary and Conclusion

In this chapter, the determination of signal attenuation and signal phase shift due to the interaction of the signal with a passing rain envelope was done. Signal depolarization is itself due to rain attenuation either as a result of scattering or absorption, resulting in a phase change on exit from the rain medium. The advantages inherent at these bands, such as high bandwidth, miniaturization of radio equipment and antenna, easy deployment and large coverage area, are offset by propagation impairments due to rain at these bands. The focus of this chapter is to study and model the rain microstructure and classify it into its various rain types based on regional data such as drizzle, widespread, shower and thunderstorm. Oblate spheroidal rain shape is assumed with the P-P model used to compute scattering amplitude, scattering cross section and total cross section, thus specific attenuation and specific phase shift due to rain at 20 °C and a frequency range of 1 – 100 GHz are determined. The specific attenuation and specific phase shift due to rain are calculated using scattering amplitude and integrated over all the lognormal raindrop size distribution models using different rain types.

In order to evaluate the characteristics of estimated specific attenuation and phase shift for Southern Africa, percentage difference is employed to compare the obtained results with the ITU-R model. A further comparison is made with results obtained using the model derived for West Africa with results obtained using the ITU-R model to see the effect of different regions on the ITU-R results. From these results, we conclude that the ITU-R model under-estimates in some cases and overestimates in other cases, which might be due to the raindrop shape assumed in the computation. The power relation expressions obtained, together with their respective coefficients will add value in link design in the region.

Chapter 7

Conclusions and Recommendations for Future Work

7.0 Conclusions

In the first part of this study, the rain attenuation estimation is presented using both the ITU-R model and measured regional rain rate data collected over 10 years in South Africa. The results obtained in the second part of this study are based on the Intelsat 17 (IS-17) satellite characteristics which operate at C- and Ku-band and projections are made into higher frequency bands.

Across all the frequency bands from C-band up to V-band, rainfall attenuation, elevation angle, and effective path length have been determined for satellite link applications in South Africa. A consideration has been made for link availabilities from 99.99% up to 99.999% of the time. It is noted that the severity of the degradation of the propagating signal increases with increasing availability. However, for a given percentage availability, the signal degradation increases with an increase in operating frequency of the satellite link.

In the third part of this study we proposed a simple and regionally based model for the calculation of the specific rain attenuation at different rain rates and frequencies up to 100 GHz. The key parameters are “regional rain drop size distribution model” and “rain rate”. The results presented show the suitability and adaptability of the model for the Southern African region. This makes it possible to calculate specific rain attenuation and thus total attenuation at a defined distance of less than 60 km. The statistical tests confirmed the suitability of other models such as the modified Gamma model. For the optimum calculation of the attenuation, a rain attenuation model for non-spherical raindrops is proposed. This result will serve as a good tool for radio planning engineers and technicians especially in the Southern African region where no comprehensive work has been carried out in the field of radio propagation through rain.

The fourth part of this study presented realistic raindrops based on their extinction total cross section and the specific attenuation due to rain using three models, namely, the Morrison and Cross (or spheroidal) model, the Pruppacher-Pitter model, and the Mie (or spherical) model. A further investigation of the validity of the Mie spherical raindrops model that is used by many authors was carried out. It is observed that while the extinction cross-section varies considerably with raindrop size, the three models show a close agreement for small raindrop diameters but differ as the drop size increases. The Mie model thus remains accurate for fade margin determination for small raindrop diameters; this model therefore gives reliable specific rain attenuation predictions in regions

dominated by drizzle rainfall, but will considerably underestimate the attenuation in regions dominated by shower and thunderstorm rain types.

The results also show that the raindrop extinction cross section for the three models agree at the lower frequencies while a noticeable difference is observed as the frequency increases. The effect of polarization is noticed in the M-C model and the P-P model, with the horizontal polarization returning the higher percentage difference compared to the Mie model.

The specific attenuation due to rain for different total cross-sections (P-P, M-C and Mie models) with circular polarization for different rain types shows a progressive increase in the average percentage differences (with respect to the Mie model) from drizzle through widespread to thunderstorm rain types. The average specific attenuation percentage difference for the P-P model is low compared to the M-C model. The results further show that the power law model parameters, k and α , can be modelled using a fourth order polynomial. The specific rain attenuation can thus be determined using the power law model for frequencies up to 100 GHz and rain rate up to 100 mm/hr. In regions where there is a high presence of large raindrops (as is the case in tropical and sub-tropical regions like South Africa), it is inadequate to employ the Mie model in the determination of local rain fade margins. However, this model is acceptable for regions dominated by the drizzle rain type due to a high presence of small drops.

In the fifth and last part of this study the focus was to study and model the rain microstructure and classify it into its various rain types based on regional data such as drizzle, widespread, shower and thunderstorm. Oblate spheroidal rain shape is assumed with the P-P model used to compute scattering amplitude, scattering cross section and total cross section, thus specific attenuation and specific phase shift due to rain at 20 °C and a frequency range of 1 – 100 GHz are determined.

The raindrop size models for each rain type are presented by their respective expressions. The results determined here will improve the accuracy of specific attenuation and specific phase shift due to rain in the sense that each unnoticed peak that might be peculiar with the general expression is being identified. The specific attenuation and specific phase shift due to rain are calculated using scattering amplitude and integrated over all the lognormal raindrop size distribution models using different rain types.

In order to evaluate the characteristics of estimated specific attenuation and phase shift for Southern Africa, percentage difference is employed to compare the obtained results with the accepted ITU-R model. A further comparison is made with results obtained using the model derived for West Africa with results obtained using the ITU-R model to see the effect of different regions on the ITU-R results. It is observed that the ITU-R model either under-estimated in some cases or overestimated the rain attenuation in the South African region, which might be due to the raindrop shape assumed in the

computation (spherically-shaped raindrop). The phase shift and specific attenuation power relation expressions obtained will be useful in improved link design in the South African region.

7.1 Recommendations for Future Work

Rain attenuation in both terrestrial and satellite links remains under-researched in Southern Africa. The dynamic nature of the seasonal as well as annual rain patterns still presents a new frontier for research, with regard to their impact on link performance. As such, much of the work involving attenuation computation in South Africa using rainfall data as well as confirmation measurements have only been extensively carried out in Durban. The same needs to be extended to cover more areas.

The limitation of the JWD with regard to the smallest raindrop size it can measure has meant that raindrops that are smaller than 0.3 mm have not been included in the development of rain DSDs. To mitigate this limitation, it will be necessary to develop parameterizations that will correct the JWD measurements through factoring in raindrops of small diameters for the Southern African region. This could be done through a transformation that will focus on correcting the DSDs measured. Also, different types of measurement equipment need to be used concurrently so as to draw comparisons with the results obtained using the Joss-Waldvogel RD-80 distrometer used in the current study.

References

- [1] G.O. Ajayi, S. Feng, S.M. Radicella, B.M. Reddy (Eds.): *Handbook on radio propagation related to satellite communications in tropical and subtropical countries*, (ICTP, 1996).
- [2] T.J.O. Afullo, “Raindrop Size Distribution Modelling for Radio Link Design along the Eastern Coast of South Africa,” *PIER B*, Vol.34, pp. 345-366, 2011.
- [3] J.O. Laws and D.A Parsons, “The relation of raindrop-size to intensity,” *Trans. Amer. Geophys. Union*, Vol.24, pp.452-460, 1943.
- [4] F. Moupfouma, & J. Tiffon, “Raindrop size distribution from microwave scattering measurements in equatorial and tropical climates,” *Electronic Letters*, Vol. 18, pp. 1012 – 1014, 1982.
- [5] H.R. Pruppacher, and R.L. Pitter, “A semi-empirical determination of shape of cloud and rain drops,” *J. Atmos. Science*, Vol. 28, pp. 86-94, 1971.
- [6] Mie, “Contributions to the optics of turbid media particularly of colloidal metal solutions,” *Annalen Dr Physiq*, Vol 25 (3), pp. 377-445, 1908.
- [7] M.O. Odedina, *A Semi-Empirical Formulation for Determination of Rain Attenuation on Terrestrial Radio Links*, Ph.D. Thesis, School of Electrical, Electronics and Computer Engineering, University of KwaZulu Natal, Durban, South Africa, 2010.
- [8] O. Massambani,, and C. A. M. Rodriquez, “Specific attenuation as inferred from drop size distribution measurements in the tropics,” in *Proceedings of URSI Commission F symposium*, pp. 25 – 28, Rio de Janeiro, Brazil, 3-7 December, 1990.
- [9] L. R. Maciel, and M. S. Assis, “Tropical rainfall drop-size distribution,” *Int. J. Sat. Commun.*, 8, 181 – 186, 1990.
- [10] Zainal, A. R., I. A. Glover, and P. A. Watson, “Rain rate and drop size distribution measurements in Malaysia,” in *Proceedings of IEEE International Geoscience and Remote Sensing Symposium* pp. 309 – 311, 1993.
- [11] R. MD Islam, Y. A Abdulrahman and T. A Rahman, “An improved ITU-R rain attenuation prediction model over terrestrial microwave links in tropical region,” *EURASIP Journal on Wireless Communications and Networking*, 2012:189, pp. 1-9, 2012.

- [12] T. S. Yeo, P. S. Kooi, and M. S. Leong, and S. S. Ng , “Microwave attenuation due to rainfall at 21.255 GHz in the Singapore Environment,” *Electron. Lett.*, 26(14), 1021 – 1022, 1990.
- [13] Z. X. Zhou, L. W. Li, T. S. Yeo, and M. S. Leong , “Cumulative distributions of rainfall rate and microwave attenuation in Singapore’s tropical region,” *Radio Science*, 35(3), 751 – 756, 2000.
- [14] G. O. Ajayi, and E. B. C. Ofoche, “Some tropical rainfall rate characteristics at Ile-Ife for microwave and millimeter Wave Application,” *J. Climate and Appl. Meteor.*, 23(4), 562 – 567, 1983.
- [15] G. O. Ajayi, and R. L. Olsen, “Modeling of a tropical raindrop size distribution for microwave and millimeter wave applications,” *Radio Sci. J.*, 20(20), 193 –202, 1985.
- [16] G. O. Ajayi, and S. U. B. Ezekpo, “Development of climatic maps of rainfall rate and attenuation for microwave application in Nigeria,” *The Nigerian Engineer* 23(4), 13 – 30, 1988.
- [17] G. Giambene, *Resource Management in Satellite Networks: Optimization and Cross-layer design*. Springer, ISBN 978-0-387-36897-9, 2007.
- [18] W. Dissanayake, “Ka-Band propagation Modeling for Fixed Satellite Application,” *Online Journal of Space Communication* Issue No.2, Fall 2002.
- [19] P.A. Owolawi, *Characteristics of Rain at Microwave and Millimetric Bands for Terrestrial and Satellite Links Attenuation in South Africa and Surrounding Islands*, Ph.D. Thesis, School of Electrical, Electronics and Computer Engineering, University of KwaZulu Natal, Durban, South Africa, 2010.
- [20] M.O. Odedina, and T.J.O. Afullo, “Determination of Rain Attenuation from Electromagnetic Scattering by Spherical Raindrops: Theory and Experiment,” *Radio Science* 45: RS1003, 2010.
- [21] A. Dissanayake, J. Allnutt, and F. Haidara, “A Prediction Model that Combines Rain Attenuation and Other Propagation Impairments along Earth-Satellite Paths,” *IEEE Trans. Antennas and Propagation*, vol. 45, No. 10, 1997, pp. 1546 – 1557.
- [22] L. Castanet *et al.*, “Comparison of Various Methods for Combining Propagation Effects and Predicting Loss in Low Availability Systems in the 20-50 GHz Frequency Range,” *Int’l. J. Satell. Commun.*, vol. 19, 2001, pp. 317–34.
- [23] L. J. Ippolito, *Satellite Communications System Engineering, 1st Ed.*, John Wiley and Sons, 2008, Chapter 8.

- [24] D. B. Hodge, "An Improved Model for Diversity Gain on Earth-Space Propagation Paths," *Radio Sci.*, vol. 17, no. 6, 1982, pp. 1393–99.
- [25] A. D. Panagopoulos, P.-D. M. Arapoglou, and P. G. Cottis, "Satellite communications at Ku, Ka and V bands: Propagation impairments and mitigation techniques," *IEEE Commun. Surv. Tutor.*, Oct. 2004, 3rd Quart.
- [26] M. Filip and E. Vilar, "Adaptive Modulation as a Fade Countermeasure, An OLYMPUS Experiment," *Int'l. J. Satell. Commun.*, vol. 8, 1990, pp. 31–41.
- [27] C. Chu and K.S. Chen, "Effects of Rain Fading on the Efficiency of the Ka-band LMD system in the Taiwan Area," *IEEE Trans. On Vehicular Technology*, Vol.54, No.1, 2005.
- [28] ITU-R Recommendation P.618.10, *Propagation data and prediction methods required for the design of Earth-space telecommunication systems*, 10/2009, Geneva, Switzerland.
- [29] ITU-R Recommendation P.840-4, *Attenuation due to clouds and fog*, 10/2009 Geneva, Switzerland.
- [30] ITU-R Recommendation P.676-10, *Attenuation by atmospheric gases*, Geneva, Switzerland.
- [31] ITU-R Recommendation P.838-3, *Specific attenuation model for rain for use in prediction methods*, 09/2005, Geneva, Switzerland.
- [32] ITU-R Recommendation P.839-3, *Rain height model for prediction methods*, 02/2001, Geneva, Switzerland.
- [33] ITU-R Recommendation P.530-12, *Propagation data and prediction methods required for the design of terrestrial Line-of-Sight Systems*, 2012, Geneva, Switzerland.
- [34] R. L. Freeman, *Radio system design for telecommunications*, Third Edition, WILEY-INTERSCIENCE: John Wiley & Sons Inc., New York, 2007.
- [35] S.M. Babin, "A case study of subrefractive conditions at Wallops Island, Virginia," *Journal of Applied Meteorology*, vol. 34, pp. 1028-1038, 1995.

- [36] COST Project 255, *Radiowave Propagation Modeling for Satcom Services at Ku band and Above*, Final Report, ESA Publication Division, 2002.
- [37] N.K. Chaudhary, D.K. Trivedi and R. Gupta, "The impact of k-factor on the wireless link in Indian semi-desert terrain," *International Journal Advanced Networking and Applications*, vol. 2, Issue 04, pp. 776-779, 2011.
- [38] B.G Ayantunji, P.N Okeke, J.O Urama and Y. Najib, "A semi-empirical model for extrapolation of surface refractivity over Nigeria," *African Review of Physics*, vol. 6, No. 14, pp. 121-128, 2011.
- [39] P.K. Odedina and T.J.O Afullo, "Multipath propagation modeling and measurement in clear-air environment for LOS link design application," *Southern Africa Telecommunication Networks and Applications Conference Proceedings*, 2009.
- [40] N.B.A. Rahim, Dao, H., Islam, M.R., and Ibrahim, A.F.I., "Prediction of the tropospheric scintillation for earth to satellite link in tropical climate," *4th International Conference on Mechatronics (ICOM)*, 17-19 May 2011, Kuala Lumpur, Malaysia.
- [41] Karasawa, Y., M. Yamada and J. E. Allnutt, "A New Prediction Method for Tropospheric Scintillation on Earth-Space Paths," *IEEE Trans. Antennas Propagat.*, pp. 1608-1614, 1988.
- [42] Ippolito L.J., *Radiowave Propagation in Satellite Communications*, van Nostrand Reinhold Company, 1986.
- [43] K. Harb, A. Srinivasan, H. Changcheng, and B. Cheng, "Prediction Method to Maintain QoS in Weather-impacted Wireless and Satellite Networks," *Proceedings of the 2007 ISIC IEEE International Conference on Systems, Man and Cybernetics*.
- [44] R.K. Crane, "Prediction of the Effects of Rain on Satellite Communication Systems," *Proceedings of the IEEE*, vol. 65, No. 3, pp. 456 – 474, March 1977.
- [45] R. Olsen, D. Rogers, and D. Hodge, "The aR^b relation in the calculation of rain attenuation," *IEEE Trans. Antennas Propag.*, Vol. 26, no. 2, pp. 318–329, 1978.

- [46] Y. T. Karasawa and T. Matsudo, "Characteristics of fading on low-elevation angle Earth-space paths with concurrent rain attenuation and scintillation," *IEEE Transactions on Antennas and Propagation*, vol. 39, No. 5, pp. 657 – 661, 1991.
- [47] M. P. H. Hall, L. W. Barclay, and M.T. Hewitt (1996), *Propagation of Radiowaves*, IEE Press, London.
- [48] H. J. Liebe, T. Manabe, and G. A. Hufford, "Millimetre Wave Attenuation and Delay Rates Due to Fog/Cloud Conditions," *IEEE Transactions on Antennas and Propagation*, December 1989, vol. 37, No. 12, pp. 1617 – 1623.
- [49] S.I.S. Hassan, *Satellite link impairment due to rain and other climatic factors*, Department of Electrical and Electronic Engineering, Universiti Sains Malaysia, Available on http://www.aprsaf.org/data/aprsaf12_data/day2/csa/6_Dyed_csawg.pdf, last accessed on 16th October 2013.
- [50] E.A. Altshuler and R.A. Marr, "Cloud attenuation of millimetre wavelengths," *IEEE Transactions on Antennas and Propagation*, 1989, vol. 37, pp. 1473 – 1479.
- [51] A. W. Dissanayake, J. Allnut, and F. Haidara, "Cloud attenuation modelling for SHF and EHF applications," *International Journal of Satellite Communications*, 2001, Vol. 19, pp. 335 – 345.
- [52] E. Salonen, "Prediction models of atmospheric gases and clouds for slant path attenuation," *Olympus Utilization Conference*, Sevilla, 1993, pp. 615 – 622.
- [53] B.T Maharaj, "Application of fade countermeasures to alleviate rain fade attenuation on earth-space links," *Satnac* 1998.
- [54] F.Moupfouma, "Improvement of a rain attenuation prediction method for terrestrial microwave links," *IEEE Transactions on Ant .and prop.*, Vol. AP-32, No.12, pp.1368-1372, 1984.
- [55] P.A. Owolawi, "Rainfall rate probability density evaluation and mapping for the estimation of rain attenuation in South Africa and surrounding islands," *PIERS Online*, Vol.112, pp.155-181, 2011.

- [56] P.A. Owolawi, S.J. Malinga and T.J.O. Afullo, "Estimation of Terrestrial Rain Attenuation at Microwave and Millimeter Wave Signals in South Africa Using the ITU-R Model," *PIERS Proceedings*, Kuala Lumpur, Malaysia, March 27-30, 2012, pp. 952-962.
- [57] S.J. Malinga, P.A. Owolawi, and T.J.O. Afullo, "Estimation of Rain Attenuation at C, Ka, Ku, and V Bands for Satellite Links in South Africa," *PIERS Proceedings*, Taipei, Taiwan, March 25-28, 2013, pp. 948-958.
- [58] ITU-R Recommendation P.618-8, *Propagation data and prediction methods required for the design of Earth-space telecommunication systems*, ITU, Geneva, Switzerland, 2003.
- [59] N.C. Mondal, S.K. Sarkar, "Rain height in relation to 0-1°C isotherm height for satellite communication over the Indian Subcontinent," *Theoretical and Applied Climatology*, Vol. 76, 89–104, 2003.
- [60] J.T. Ong, K.I. Timothy, F.B.L. Choo, W.L. Carron, "Effective rain height statistics for slant path attenuation prediction in Singapore," *Electronic Letters* 36 (7), pp. 661–663, 2000.
- [61] S. Parshoatam, I.S. Hudiara, M.L. Singh, "Estimation of effective rain height at 29 GHz at Amritsar (tropical region)," *IEEE Transaction on Antennas and Propagation* 55 (5), 1463–1465, 2007.
- [62] G. O. Ajayi, and F. Barbaliscia, "Prediction of attenuation due to rain: Characteristics of the 0°C isotherm in temperate and tropical climates," *International Journal of Satellite Communication*, Vol. 8, pp. 187-196, 1990.
- [63] J. S. Seybold, *Introduction to RF Propagation*, John Wiley & Sons, Hoboken, NJ, 2005, pp. 255-270.
- [64] R.K Crane, *Electromagnetic wave propagation through rain*, John Wiley, 1996.
- [65] S.Das, A. Maitra, A.K. Shukla, "Rain attenuation modelling in the 10 – 100 GHz frequency using drop size distributions for different climate zones in tropical India," *PIER B*, 25, pp. 211-224, 2010.

- [66] K.S. Chen, C.Y. Chu, Y.C. Tseng, "A semi-empirical model of rain attenuation at Ka-band in Northern Taiwan," *PIER M*, 16, pp. 213-223, 2011.
- [67] J.S. Mandeep, J.E. Allnut, "Rain attenuation prediction at Ku-band in South East Asian countries," *PIER*, Vol. 76, pp. 65-74, 2007.
- [68] A. Berne, and R. Uijlenhoet, "A stochastic model of range profiles of raindrop size distributions: Application to radar attenuation correction," *Geophys. Res. Lett.*, 32, L10803, doi: 10.1029/2004GL021899, 2005a.
- [69] A.R. Jameson and A.B. Kostinski, "What is a Raindrop Size Distribution?," *Bulletin of the American Meteorological Society*, Vol.82, pp.1169-1177, 2001.
- [70] R. Uijlenhoet, J.A. Smith, and M. Steiner "Microphysical Structure of Extreme precipitation as inferred from Ground-based Raindrop spectra," *Journal of the Atmospheric Sciences*, Vol. 60, pp. 1220-1238, 2003.
- [71] J.S. Marshall. and W.M. Palmer, "The distribution of raindrops with size," *Journal of Meteorology*, Vol.5, pp. 165-166, 1948.
- [72] R.G. Quimpo and A.B Brohi, "On the frequency distribution of raindrop sizes," *Journal of Irrigation and Drainage Engineering*, Vol.112, No.2, pp. 119-127, May 1986.
- [73] P.A Owolawi, "Raindrop Size Distribution Model for the Prediction of Rain Attenuation in Durban," *PIERS Online*, Vol.7, No.6, pp. 516-523, 2011.
- [74] L.R. Maaciél and M.S. Assis, "Tropical rainfall drop size distribution," *International Journal of Satellite Communications*, Vol.8, pp. 181-186, 1990.
- [75] L.S. Kumar, Y.H. Lee, and J.T Ong, "Truncated Gamma Drop Size Distribution Models for Rain Attenuation in Singapore," *IEEE Transactions of Antennas and Propagation*, Vol.58, No.4, April 2010.
- [76] L.S. Kumar, Y.H. Lee, and J.T. Ong, "Two-Parameter Gamma Drop Size Distribution Models for Singapore," *IEEE Transactions on Geoscience and Remote Sensing*, Vol.549, No.4, September 2011.

- [77] B.S. Jassal A. K. Verma and Lal Singh, "Raindrop size distribution and attenuation for Indian climate," *Indian Journal of Radio and Space Physics*, Vol.23, Iss.3, pp. 193-196, June 1994.
- [78] A.R. Tharek and J. Din, "Rainfall drop size distribution measurements in Malaysia," *Proc. URSI Comm. F. 1992 Symposium on Wave Propagation and Remote Sensing*, Ravenscar, North Yorkshire, UK, 8-12 June, 1992, pp 1.2.1-1.2.5.
- [79] G.O. Ajayi and A. Adimula, "Variations in raindrop size distribution and specific attenuation in a tropical environment," *URSI Comm. F Symposium*, La Londe-les Maures, France, pp. 811-814, September 1989.
- [80] B. Sevruk, , and W. R. Hamon, *International comparison of national precipitation gauges with a reference pit gauge. WMO Instrument and Observing Methods Rep. 17*, 1984. [Available from World Meteor. Org., Case Postale 2300, CH-1211, Geneva, Switzerland].
- [81] B. Sevruk, "Wind induced measurement error for high-intensity rains. Proc. International Workshop on Precipitation Measurement," *WMO Tech. Document 328*, 199–204, 1989. [Available online at <http://www.wmo.ch>].
- [82] P. Y. Groisman, and D. R. Legates, "The accuracy of United States precipitation data," *Bull. Amer. Meteor. Soc.*, Vol. 75, 215-227, 1994.
- [83] V. Nešpor, , and B. Sevruk, "Estimation of wind-induced error of rainfall gauge measurements using a numerical simulation," *J. Atmos. Oceanic Technol.*, Vol. 16, 450–464, 1999.
- [84] B. Sevruk, , M. Ondras and B. Chvila, "The WMO precipitation measurement intercomparisons," *Atmos. Res.*, Vol. 92, 376-380, 2009.
- [85] O. Fiser, M . Schoenhuber, and P. Pesice, "First results of DSD measurement by video distrometer in the Czech Republic in 1998–1999," *Studia Geophysica et Geodetica*, 46, 3, 485–505, 2002.
- [86] I.A Adimula and G.O. Ajayi, "Variation in raindrop size distribution and specific attenuation due to rain in Nigeria," *Ann. Telecom*, Vol.51, No. 1-2, pp. 87–93, 1996.

- [87] K.I. Timothy, J.T. Ong and E.B.L. Choo, "Raindrop size distribution using method of moments for terrestrial and satellite communication applications in Singapore," *IEEE Trans. Antennas Propagat.*, vol. 50, pp. 1420–1424, October 2002.
- [88] J.S. Mandeep and K. Tanaka; "Effect of atmospheric parameters on satellite links," *Int. Journal Millimeter wave*, 2007, 28(10), pp. 789-795.
- [89] L.S. Kumar, Y.H. Lee, J.X. Yeo and J.T. Ong., "Tropical rain classification and estimation of rain from Z-R (Reflectivity-rain rate) relationships," *PIER B*, Vol.32,107-127, 2011.
- [90] R. Gunn and G.D. Kinzer, "The terminal velocity of fall for water droplets in stagnant air," *Journal Atmos. Sci.*, Vol.6, No.4, pp. 243-248, 1949.
- [91] J. Vivekanandan, G. Zhang, and E. Brandes, "Polarimetric radar rain estimators based on constrained gamma drop size distribution model," *J. Appl. Meteorology.*, Vol.43, No.2, pp. 217-230, 2004.
- [92] T. Kozu, and K. Nakamura., "Rainfall parameter estimation from dual-radar measurements combining reflectivity profile and path-integrated attenuation," *J.Atmos. Oceanic Tech.*, 1991, Vol. 8(2), pp. 259-270.
- [93] C.W. Ulbrich, "Natural variation in the analytical form of the raindrop size distribution," *J. Climate Appl. Meteor.*, Vol. 22, pp. 1764-1775, 1983.
- [94] K.I. Timothy, S. Sharma, M. Devi and A.K. Barbara, "Tropical raindrop size distribution (RDS): Prediction and modeling its effects on microwave propagation," *Proceedings of 9th International Conference on Antennas and Propagation*, Eindhoven, The Netherlands, 4-7 April 1995, pp. 244-248.
- [95] H. Jiang, M. Sano and M. Sekine, "Weibull Raindrop-size distribution and its application to rain attenuation," *IEE Proc., Microwave, Antenna Propagation.*, Vol.144, No.3, pp.197-200, June 1997.
- [96] S. J. Malinga and P. A. Owolawi, "Obtaining raindrop size model using the method of moments and its applications for South African radio systems," *PIER B Journal*, Vol. 46, pp. 119-138, 2013.

- [97] W. Pan, Leung, P., Huang, W and Wei Liu, W. "On interval estimation of the coefficient of variation for three-parameter Weibull, lognormal and gamma distribution: A simulation-based approach," *European Journal of Operational Research*, 164, pp. 367-377, 2005.
- [98] C.J. Willmott and K. Matsuura., "Advantages of the mean absolute error (MAE) over the root mean square error (RMSE) in assessing average model performance", *Climate Research* , Vol.30, pp. 79-82, December ,2005.
- [99] J. T. Ong and Y. Y. Shan, "Raindrop size distribution models for Singapore: comparison with results from different regions," *Proc. 10th Intl. Conf. on Ant. & Prop.*, Vol. 436, 2.281-2.285, 1997.
- [100] J. T. Ong *et al.*, "Studies on tropical rainfall structure with RAL S-band radar, TRMM PR and radiosonde-inter comparison," *Proc. European Geophysical Society, XXVI General Assembly*, France, Mar. 2001.
- [101] T.S. Yeo, P.S. Kooi, M.S. Leong, and L.W. Li, "Tropical raindrop size distribution for the prediction of rain attenuation of microwaves in the 10-40 GHz band," *IEEE Transactions on Antennas and Propagation*, Vol.49, No.1, 80-82, January 2001.
- [102] L. da Silva Mello and M.S. Pontes., "Unified method for the prediction of rain attenuation in satellite and terrestrial links," *Journal of Microwaves, Optoelectronics and Electromagnetic Applications*, Vol.11, No.1, June 2012.
- [103] F. Moupfouma, "A new theoretical formulation for calculation of the specific attenuation due to precipitation particles on terrestrial and satellite radio links," *International Journal of Satellite Communications*, Vol. 15, pp. 89-99, 1997.
- [104] I. Seishiro, "Rain attenuation at millimeter wavelength of 1.33 mm," *International Journal of Infrared and Millimeter waves*, Vol. 25, No.10, pp. 1495-1501, October 2004.
- [105] M. Sekine, C. Chen, and T. Musha, "Rain attenuation from log-normal and Weibull raindrop-size distributions," *IEEE Trans. Antenna and propagation*, Vol. AP-35, No.3, pp. 358-359, March 1987.
- [106] D.A. De Wolf, "On the Law-Parsons distribution of raindrop sizes," *Radio Science*, Vol. 36, No.4, pp. 639-642, June/August 2001.

- [107] T. Kozu, *Estimation of raindrop size distribution from space borne radar measurements*, Ph.D. dissertation, Univeristy of Kyoto, Japan, 1991.
- [108] P.W. Mielke Jr., "Simple iterative procedures for two parameter gamma distribution maximum likelihood estimates," *Journal. Appl. Meteor.* Vol. 15, pp. 181-183, 1976.
- [109] S. Moumouni, M. Gosset, and E. Houngninou, "Main features of rain drop size distributions observed in Benin, West Africa, with optical distrometers," *Geophysical Research Letters*, Vol. 35, No. 23, L23807, doi: 10.1029/2008GL035755, December 2008.
- [110] J.A Morrison and M.J. Cross, "Scattering of a plane electromagnetic wave by axisymmetric raindrops," *Bell Syst. Tech. J.*, Vol. 53, pp. 955-1019, July-August, 1974.
- [111] L.W. Li, P.S. Kooi, M.S. Leong, T.S. Yeo, and M.Z. Gao, "Microwave attenuation by realistically distorted raindrops: Part I-Theory," *IEEE Trans. Antenna Propagation*, Vol. 43, No.8, pp. 811-821, 1995.
- [112] L.W. Li, P.S. Kooi, M.S. Leong, and T.S. Yeo, "Integral Equation Approximation to Microwave Specific Attenuation by Distorted Raindrops: The Pruppacher-and-Pitter Model," *Proceedings of IEEE Singapore International Conference*, 3-7 Jul 1995, pp. 600-604, ISBN: 0-7803-2579-6.
- [113] L.W. Li, P.S. Kooi, M.S. Leong, and T.S. Yeo, "Integral Equation Approximation to Microwave Specific Attenuation by Distorted Raindrops: The Spheroidal Model," *Proceedings of IEEE Singapore International Conference*, 3-7 Jul 1995, pp. 658-662, ISBN: 0-7803-2579-6.
- [114] T. Oguchi, "Attenuation of electromagnetic wave due to rain with distorted raindrops," *J. Radio Res. Labs.*, Vol. 7, pp. 467-485, 1960.
- [115] Distromet Ltd., *Distrometer RD-80 instructional manual*, Basel, Switzerland, June 20, 2002.
- [116] T.J. Schuur *et al.*, "Drop Size Distribution Measured by a 2D Video Disdrometer: Comparison with Dual-Polarization Radar Data," *Journal of Applied Meteorology*, Vol. 40, pp. 1019 – 1034, June, 2001.

- [117] H. R. Pruppacher and K. V. Beard, "A wind tunnel investigation of the internal circulation and shape of water drops falling at terminal velocity in air," *Quart. J. R. Met. Soc.*, Vol. 96, pp. 247-256, April 1970.
- [118] T. Oguchi, "Electromagnetic wave propagation and scattering in rain and other hydrometeors," *Proc. IEEE*, Vol. 71, Issue 9, pp. 1029-1078, Sept. 1983.
- [119] L. W. Li *et al.*, "On the simplified expression of realistic raindrop shapes," *Microwave & Optical Technol. Letters*, Vol. 7, Issue 4, pp. 201-205, March 1994.
- [120] S.J. Malinga, P.A. Owolawi and T.J.O. Afullo, "Determination of specific rain attenuation using different total cross-section models for Southern Africa," *SAIEE Africa Research Journal*, Vol. 105, No. 1, pp. 20-30, 2014.
- [121] M. Marzuki, T. Kozu, and T. Shimomai, "Diurnal Variation of Rain Attenuation Obtained from Measurement of Raindrop Size Distribution in Equatorial Indonesia," *IEEE Transactions on Antennas and Propagation*, Vol. 57, 1191-1196, 2009.
- [122] R.K. Crane, "Propagation phenomena affecting satellite communication systems operating in centimeter and millimeter wavelength bands," *IEEE Transactions on Antennas and Propagation*, AP-26, No.2, 318-329, 1978.
- [123] D.V. Rogers and R.L. Olsen, "Calculation of radiowave attenuation due to rain at frequencies up to 1000 GHz," *Communications Res. Centre, Dept. of Communications, Ottawa, ON, Canada, CRC Rep. 1299*, 1976.
- [124] T. Oguchi, "Attenuation of Electromagnetic wave due to rain with distorted raindrops (Part II)," *Journal of Radio Labs (Japan)*, 11, 19-44, 1964.
- [125] T. Oguchi, "Scattering and absorption of a millimeter wave due to rain and melting hailstones," *Journal of Radio Labs (Japan)*, 13, 141-172, 1966.
- [126] T. Oguchi, "Effect of incoherent scattering on microwave and millimeter wave communication through rain," *Electronics Letter*, 27, 759-760, 1991.

- [127] R.G. Medhurst, "Rainfall attenuation of centimeter waves: Comparison of theory and measurement," *IEEE Transactions on Antennas and Propagation*, AP-13, 550-564, 1965.
- [128] M.O. Ajewole, L.B. Kolawole and G.O. Ajayi, "Theoretical study of effect of different types of tropical rainfall on microwave and millimeter-wave propagation," *Radio Science*, 34, 1103–1124, 1999.
- [129] P.K. Kunhikrishnan, R. Sivaraman, and D.P. Alappattu, "A case study of rain drop size distribution over a tropical Indian station," *36th COSPAR Scientific Assembly*, 16-23 July, Beijing China, 2006.
- [130] P.A. Owolawi: *Rain at SHF and EHF for Radio Link in South Africa: Characteristics of Rain at SHF and EHF for Terrestrial and Satellite Links in South Africa*, LAP LAMBERT ACADEMIC Publishing, ISBN: 9783846596548, 2011.
- [131] K. Naicker and S.H. Mneney, "Propagation Measurement and modelling for terrestrial line-of-sight links at 19.5 GHz," *IEEE Africon 2004*, Gaborone, Botswana, pp. 95-100, 2004.
- [132] M.O. Fashuyi and T.J.Afullo, "Rain attenuation prediction and modelling for LOS links on terrestrial paths in South Africa," *Radio Science*, Vol.42, RS003618, 2007.
- [133] H.J. Liebe, "MPM – An atmospheric millimeter wave propagation model," *International Journal of Infrared and Millimetre Waves*, Vol. 10, No. 6, pp. 631 – 650, 1989.
- [134] J. Goldhirsh, "Two-dimension visualization of rain cell structure," *Radio Science*, Vol. 35, pp. 713-729, 2000.